PROJECT REPORT: MAXIMUM POWER POINT TRACKING OF PV ARRAYS IN KUWAIT

Mohamed Ahmed Hassan El-Sayed
Professor
Kuwait University

College of Engineering and Petroleum
Electrical Engineering Department

Tel : +965 2498-3347
elsmah@hotmail.com

Steven B. Leeb
Professor of Electrical Engineering
and Computer Science, joint
appointment in Mechanical
Engineering.

MIT Laboratory for Electromagnetic
and Electronics Systems.
Tel: 6172539360
sbleeb@mit.edu

ABSTRACT

One technology to generate electricity from renewable resources is to use solar cells to convert solar irradiance into electricity. Currently, photovoltaic (PV) energy generation has a great commercial and academic interest. Recent studies indicate that in the medium to longer term PV generation may become technically and commercially worldwide feasible to be implemented for electricity generation. The main purpose of this report is to study the performance of PV arrays under varying weather conditions in Kuwait. For this study a data base of hourly solar radiation and temperature were collected for a period of six years. The grid connected PV system converts sunlight directly into ac electricity to supply local loads and inject the excess energy to the public grid. The main purpose of the system is to reduce the electrical energy imported from the electric network. The dc output of the PV array is converted into ac and injected into the grid through an interfacing inverter. The controller of this system implements all the main regulation and protection functions such as:- Maximum Power Point Tracking (MPPT), protection relay and detection of islanding operation.

New opportunities exist for deploying switched power electronic circuits with fresh thinking about the role and use of energy storage components. During the course of this research, we have explored the application of new power electronic approaches for cell level processing, and for array configuration and MPPT tracking. This report presents some of the results from this work.

Publications associated with this work:

1. Chang, Arthur, John J. Cooley, Steven B. Leeb, "Design Considerations in Distributed MPPT Switched-Capacitor DC-DC Converters for PV Energy Extraction and Cost Effectiveness," IEEE *Applied Power Electronics Conference,* Florida, February 2012

2. Chang, Arthur, S.B. Leeb, "Improved Transient Response Control Strategy and Design Considerations for Switched-Capacitor (SC) Energy Buffer Architectures," IEEE *Applied Power Electronics Conference,* California, March 2013

3. El-Sayed, M. and S. Leeb, ðEvaluation of Maximum Power Point Tracking Algorithms for Photovoltaic Electricity Generation in Kuwait,ö International Conference on Renewable Enegies and Power Quality, Cordoba, Spain, April 2014.

4. Gillman, M., J. Donnal, J. Paris, C. Schantz, U. Orji, S.B. Leeb, M. El-Sayed, K. Wertz, S.Schertz, ðEnergy Accountability Using Non-Intrusive Load Monitoring,ö *IEEE Sensors Journal,* Vol. 14, No. 6, June 2014, pp.1923-1931.

Table of Contents

Chapter 1

Potential Utilization of Photovoltaic Electricity Generation in Kuwait

This chapter presents electric energy resources in Kuwait and discusses the development of Kuwait's electricity supplies. It also describes the electrical system in Kuwait including generation, transmission and distribution subsystems. Moreover, the available renewable energy such as solar energy and the associated radiation are analyzed to justify the potential utilization of such clean resources.

1.1 Historical Background

State of Kuwait is located in the northwestern part of the Arabian Gulf, bordered by Iraq from the north and Saudi Arabia from the south. It occupies 17,820 square kilometers with a current population of a little more than 3 million. The population is concentrated in and around Kuwait city along the gulf coast, in a radius of about 30 miles. The rest of the country is virtually unoccupied desert and oil fields [1.1].

The discovery of oil in the 1930's and then the first export of oil in 1946 have transformed Kuwait into a modern country. Kuwait has an estimated oil reserve of 96 billion barrel, which accounts to 9% of the world's oil reserves. With the massive oil revenues, the country was able to begin the civilization advancement in its governmental utilities (electricity generation and water supply), education, health care…etc. One of these utilities that will be considered in this report in details is the electric utility. A Company called "The private electric company" first introduced electricity in Kuwait in 1934; the company had a generating capacity of only 30 KW at 200 Volts D.C. In 1949, the first 3 phase, 50 Hz AC power plant with 380/220 voltage

two generators, each with a capacity of 200 KW, was installed to replace the D.C. system. In 1951, the Department of Electricity was established to be responsible for electricity production. Later, the Department of Electricity was expanded as the demand for electricity was increasing. That urged the establishment of what is now known as the Ministry of Electricity and Water (MEW), which is a government agency [1.2].

MEW had six dual purpose power plants before the Iraqi invasion in 1990. These plants had two functions to produce electricity and drinking water by desalination process. The oldest dual power plant (Al-Shuwaikh plant) was commissioned in 1954 with 4x7.5 MW capacity. The second oldest dual plant (Al-Shuaiba plant) was commissioned between 1965 and 1969 with a total installed capacity of 400 MW. These two plants were destroyed during the seven month Iraqi occupation and not repaired due to unjustified repairing cost and their passed life time. The other four power plants were repaired because they were relatively new and had higher generation capacities than the previous older units. These four are Al-Shuaiba South, Doha West, Doha East, and Al-Zour plants. These plants are fuel fired steam plants using different types of fuel such as natural gas, heavy fuel oil, crude oil, and gas oil. During peak load hours and emergency situations Gas turbines are also used, in Al-Zour and Doha East plants.

It is worth to mention that the electric demand is increasing in an exponential rate and new Dual Purpose Plants (DPP) should be installed to meet future needs. As a matter of fact, the DPP at Al-Sabiya is currently in operation with an installed capacity of 2400 MW. The actual generation cost per kWh reaches a value of 10 cent However, considering the high demand growth, it will be necessary to build new power stations to meet the expected load. This requires massive investment in electricity sector. In fact Kuwait's oil export represents more than 90% of its total revenues. On the other side,

building new fuel-fired power plants considering the last time falling oil prices has a great impact on the country's economy. This has prompted the government to utilize non-conventional renewable energy for electricity generation and to encourage the measures of energy conservation as well as rearranging the subsidiary policy of energy consumptions.

1.2 Electrical Power System in Kuwait

1.2.1 Power Generation

The Electrical utility mainly employs Thermal Steam Turbines for the generation of power needed to satisfy demand. However, Power Plants also include some Thermal Gas Turbines that make up around 14.4% of total installed capacity. Otherwise, they are kept as standby with a high degree of availability owing to gas turbines high operational costs and low thermal efficiency. The Power Generation utility has over the last five decades developed in quantity and quality. After the erection of the first (3X0.75 MW) Steam Power Station in 1952, Power Plants capacities have increased until they reached 2400 MW (8x300 MW) with the commissioning of Doha West Power Station in 1983/84 , Az-Zour South Power Station and Sabiya Power Station which is already completed and in operation. The development of the peak load and the installed capacity are displayed in Table 1.1.

Table 1.1 Development of Peak demand and Installed Capacity in Kuwait

Year	Peak Demand (MW)	Installed Capacity (MW)
1978	1595	2128
1988	3920	7398
1998	5800	7389
2008	9710	11642
2010	10890	12145

1.2.1.1 Steam Turbine Units

These units comprise the large capacity units. Their capacities vary from 134 MW to 300 MW in all Power Stations. For example in year 2008, the total installed capacity of these units is 8970 MW. The above units are operated according to the system power demand. In general, the available and operational capacity will be maximum in summer seasons as the electrical load demand increases with temperature rise and minimum in the winter seasons, hence, routine annual maintenance of the above units takes place during the winter season [1.2].

1.2.1.2 Gas Turbine Units

These are smaller capacity units ranging from 18 MW as in Doha East Power Station , 42 MW in Shuwaikh Station, 28.2 MW in Doha West and 27.75 - 165 MW in Az-Zour South Power Station and 41.7 MW as in Sabiya station. The total installed capacity is 2670.8 MW at high temperature operation. The above units are designed for normal peak load operations with blackout start capability within 10 minutes, where it takes more than five hours normally in case of steam turbine units. Table 1.2 (a) displays the turbines capacities in the different power plants of Kuwait. The development of Power Station's Installed Capacity and the generated energy in the period from 1990-now is displayed in Table 1.2 (b).

Table 1.2 (a) Turbine Capacity in the Power Plants

Power Plant	Steam turbines capacities (MW)	Gas turbines capacities (MW)
Shuwaikh		6x42 MW= 252
Shuaiba South	6x 134 MW = 804	
Doha East	7x 150 MW = 1050	6x18 MW = 108
Doha West	8x 300 MW = 2400	3x 28.2 MW = 84.6
Az-Zour South	8x 300 MW = 2400	4x27.5+8x130+5x165=1976
Subiya	8x 300 MW = 2400	6x41.7MW= 250.2

Table 1.2 (b) Development of Installed Capacity and Generated Energy in Kuwait

Year	Power (MW)	Energy (MKWh)	Year	Power (MW)	Energy (MKWh)
1987	6696	18092	2000	9189	32323
1988	7398	19599	2001	9189	34299
1989	7411	21085	2002	9189	36362
1990	7283	18477	2003	9189	38577
1991	6898	10780	2004	9689	41257
1992	6898	16885	2005	10189	43734
1993	6898	20178	2006	10189	47605
1994	6898	22802	2007	10481	48754
1995	6898	23724	2008	11641	51749
1996	6898	25475	2010	12145	55810
1997	6898	26724			
1998	7389	29984			
1999	8289	31576			
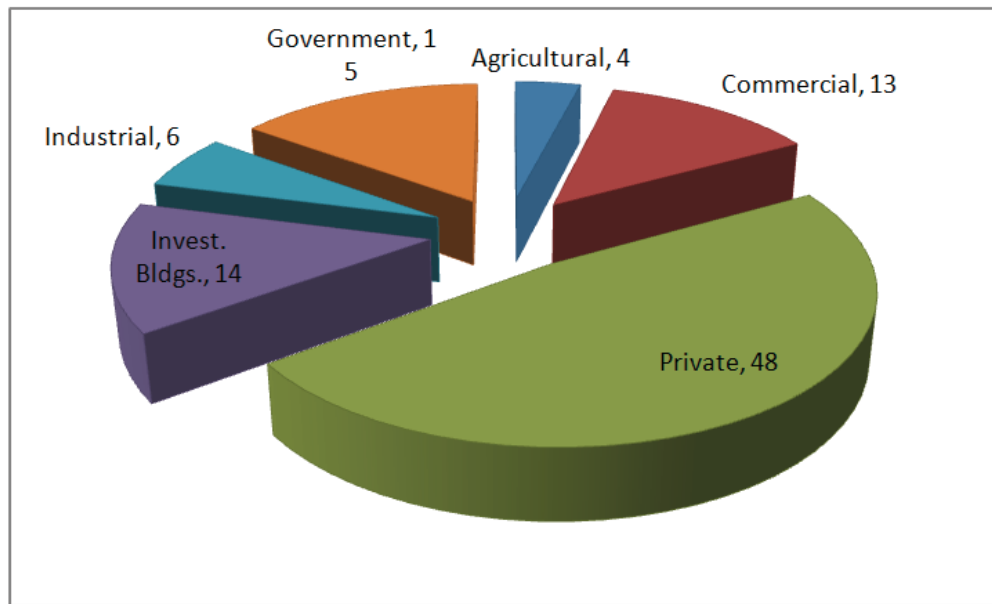
Fig. 1.1 The energy consumed in different sectors in Kuwait

As indicated in Fig. 1.1 the domestic sector in private and investment building represents 62% of the total energy consumption. Table 1.3 shows the maximum and minimum daily consumption in kWh for each month of year 2008. The relative humidity and maximum temperature as well as the percentage annual peak load increase are given in Table 1.4. The following figures show the total load, temperature and humidity at daily peak load for the summer months. The peak load reached 9710 MW on Saturday, 27th of July 2008 at 14:30, with a temperature of 50° C and relative humidity of 5 % with an annual increase of 7.06 %. In addition, the variation of load factor from year 1985-2000 is drawn in Fig. 1.2. It should be noted that the maximum load on 15 July 2012 has a value of 11610 MW while the installed capacity reaches about 13000 MW. The corresponding daily load curve at peak value is displayed in Fig. 1.3. Moreover, the relative humidity and maximum temperature for the days of peak load are displayed in Table 1.4 for the period from 1992-2008.

Table 1.3 Maximum and Minimum Daily Consumption in kWh

Month	Max. Consumption	Date	Min. Consumption	Date
January	94027	16 Jan.	71684	04 Jan.
February	84712	04 Feb.	68660	29 Feb.
March	114211	04 Mar.	71047	07 Mar.
April	142315	29 Apr.	92530	04 Apr.
May	165995	29 May.	121973	02 May.
June	187150	29 Jun.	143253	13 Jun.
July	189070	27 Jul.	159034	11 Jul.
August	187856	03 Aug.	165679	19 Aug.
September	191182	08 Sep.	137652	30 Sep.
October	144193	12 Oct.	92933	11 Oct.
November	93296	01 Nov.	77736	07 Nay.
December	87591	2I Dec.	72169	09-0ec.

Table 1.4 Relative Humidity and Maximum Temperature at Peak Load

Max. Rel. Humidity % at Peak Load	Max. Temp. at Peak Load (°C)	Date	Percentage of Annual Increase	Max. Load (MW)	Year
32	48	16.08.1992		3460	1992
28	48	17.08.1992			
6	49	10.08.1993	19.1	4120	1993
8	45	01.06.1994	5.6	4350	1994
5	48	21.06.1995	8.7	4730	1995
28	43	02.09.1996	9.9	5200	1996
18	48	28.06.1997	3.1	5360	1997
10	49	19.08.1997	8.2	5800	1998
8	48	04.09.1999	6.2	6160	1999
5	50	28.08.2000	4.7	6450	2000
38	43	13.08.2001	4.7	6750	2001
7	50	22.07.2002	7.4	7250	2002
2	49	06.07.2003	3.2	7480	2003
16	50	26.07.2004	3.6	7750	2004
7	48	03.08.2004			
7	51	17.07.2005	8.4	8400	2005
6	49	26.07.2006	6.0	8900	2006
6	47	03.09.2007	1.9	9070	2007
5	50	27.07.2008	9.1	9710	2008
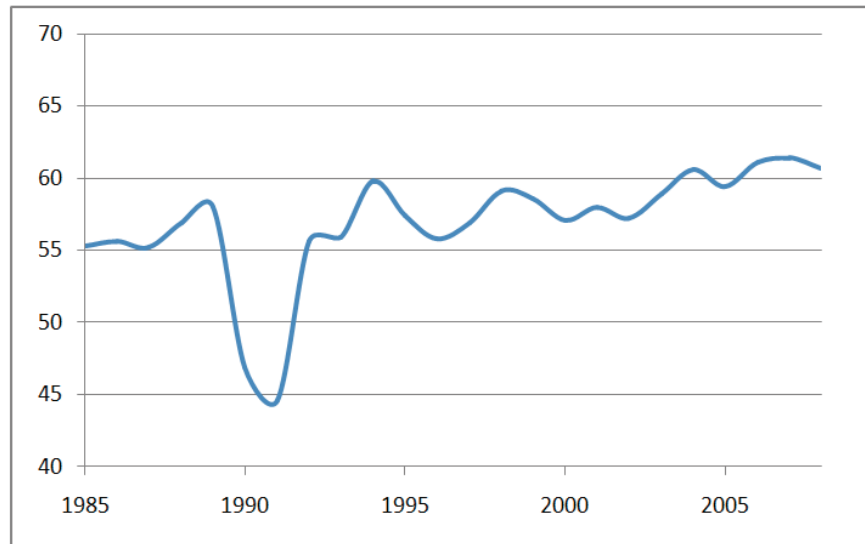
Fig. 1.2 Load factor variation for the period from 1985-2008
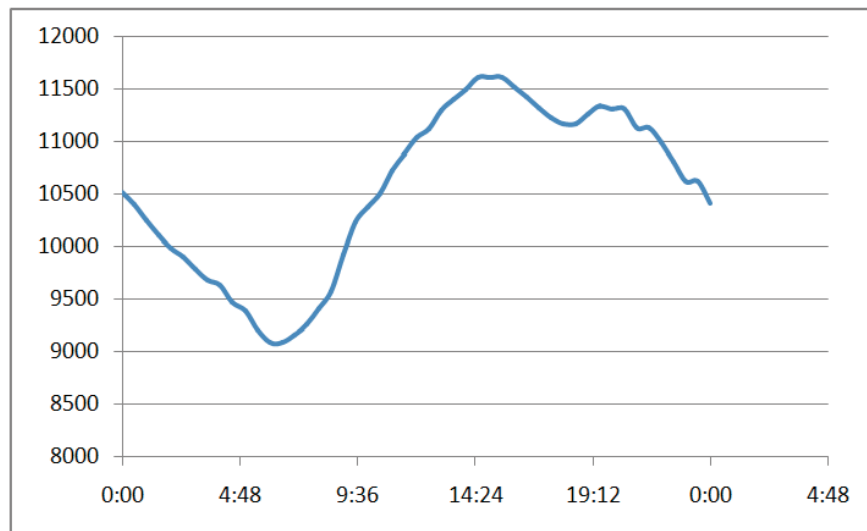
Fig. 1.3 Peak load curve in 2012

1.3 Environmental considerations

It is very important that an Environmental Impact Assessment is carried-out by any energy project planning. This includes site preparation, construction, operation, maintenance and decommissioning phases. The general significant issues that needed to be addressed include the following:

- Air pollution.

- Noise.

- Non-thermal water pollution.

- Thermal water pollution.

- Electromagnetic fields.

- Fuel storage areas and loading terminals.

- Waste management.

- Health and safety within and out-side the plant boundary.

- Ecosystem and its biotic and abiotic components.

Kuwait electrical load is characterized by high load in summer and low load in winter according to the increase and decrease in the values of temperatures and relative humidity.

1.4 Electrical Network

Currently Kuwait is covered by electric power networks system consisting of overhead lines, underground cables and power transformer substations which ensure supply to every consumer with electric energy including residential, industrial, commercial or agricultural loads. The expansion of these networks has been carried out in parallel to the rapid growth of the required electric demand. Furthermore, work is continuously

under way to strengthen and reinforce the different electrical networks to meet the additional loads resulting from the change in consumption patterns.

A brief summary of the electrical networks expansion could be expressed as follows:

In 1934, electrical network started using + 200 V (Direct Current) O/H lines with copper conductors on wooden poles. In 1949, the network voltage was changed to 380/220 V 50 Hz (A.C) after the expansion of the National Electricity Company Services. Upon the transfer of this company to Government ownership in 1951 and the erection of Shuwaikh power plant, the network voltage was raised from 380 V to 11 KV to extend the ranges of the network to satisfy the growing electrical load. Also 11 KV/415 V substations were constructed with the 11 KV underground cables and overhead lines. As 11 KV network was unable to transmit the increasing power to remote areas, a 33 KV transmission network was added in year 1958 comprising 33 KV O/H lines, underground cables and 33/11 KV substations in town and Salmiya. Upon the erection of additional power plant in 1961-62, the 33 KV transmission network was expanded with additional 33/11 KV sub-stations erected in Town, Hawally and Al-Jahra. After the erection of Shuaiba North power plant there was a need to raise the voltage to 132 KV. Consequently, the Ministry constructed the first 132 KV transmission line from Kuwait City to Shuaiba and consequently, the 5th Ring Road 132/33 KV substation was constructed to transmit power to Shuaiba and Fahaheel. Expansion and reinforcement of 132 KV network were continued in order to connect Shuaiba South and then Doha East power plant. The 132 KV network served to transmit power in bulk to the major 132/33 KV and 132/11 KV substations constructed in the main load centers in the country [1.1].

With the continued growth of electrical demand and the corresponding increase in the generating capacity, the 132 KV transmission network reached its economic and technical limit. So it was decided to introduce a new 275 kV transmission network to link the Power Stations with the 300/132 KV substations which will constitute major supply centers in various areas. Fig. 1.4 shows the existing 275 kV network in year 2012.

1. E.H.V. Network:

A - Length of Underground 275 kV Cables - 216 KM.

B - Overhead 275 kV Lines - 712 KM.

C - Number of 275 kV Sub- Stations - 19.

2. H.V. Network:

A - Number of 132 KV Sub-Stations - 277.

B - Number of 33 KV Substations - 292.

C - Length of Underground 132 KV Cables - 2566 KM.

D - Length of Underground 33 KV Cables - 1531 KM.

E - Length of Overhead 132 KV Lines – 2162 KM.

F - Length of Overhead 33 KV Lines - 1827 KM.

3. M & L.V. Network 11 KV 415 V:

A - Number of Ring Main Substations - 7043.

B - Number of Spur Substations - 5800.

C - Length of 11 KV Cables - 8784 KM.

D - Length of Low Tension Cables (415 V) – 22886 KM.

E - Length of Overhead 11 KV415 V and Low Tension Lines - 4415 KM.
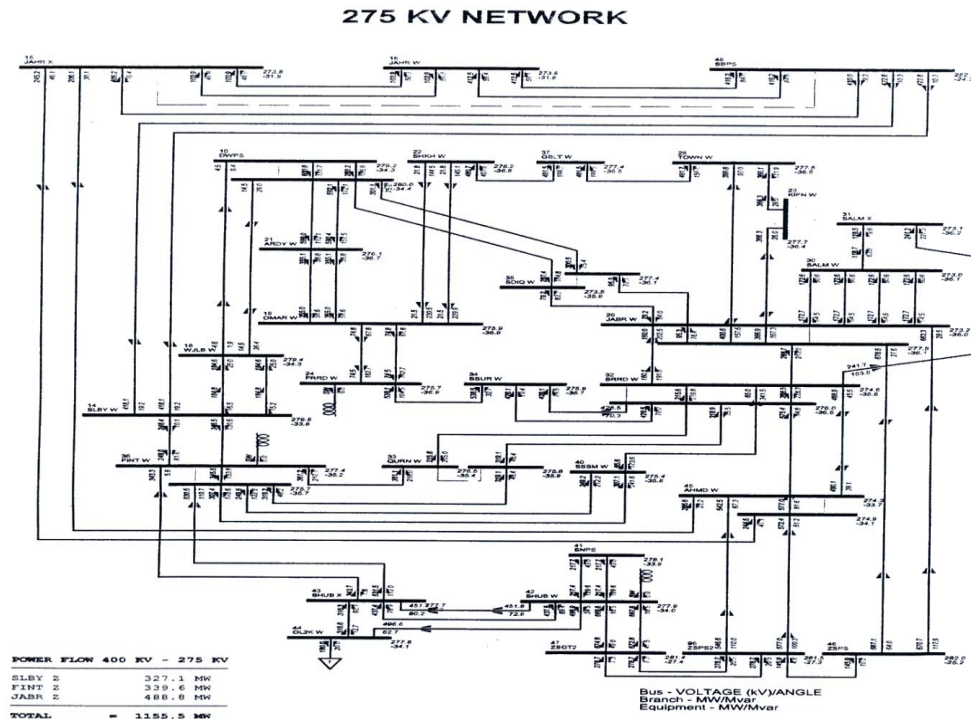
Fig. 1.4 Layout of 275 kV network in Kuwait

4. Street Lighting:

A - Length of Streets with 30 M Masts - 168 KM.

B - Length of Streets with 22 M Masts – 263.7 KM.

C - Length of Streets with 12 M Masts and 16 M Masts – 1728.5 KM.

D - Streets with HPMV Lamps on 10 M Masts - 1833.2 KM.

E - Side Roads, Different Type of Lamps on 8 M Poles – 1887.1 KM.

F - Sub-Main Roads, Different Type of Lamps on 4M – 6M Poles – 1846.2 KM.

Most of the electrical consumption takes place at the L.V. level (415/240 volts) with the exception of some industries where consumption takes place at medium voltage (11 KV) or (3.3 KV). However, electric power generation takes place at the medium voltage (from 11 KV to 21 KV) and this voltage is not adequate to transmit large amounts of

power over long distances to the center of consumption. Hence, it is necessary to step up the voltage at the Power Station to 132 or 275 kV in order to transmit the large amounts of power to the main centers of consumption where the voltage is stepped - down to lower levels in suitable substations and the power distributed in smaller amounts and in successive stage until the levels of power and voltage are suitable to supply the consumers. Therefore, the electrical networks comprise the following types of sub-stations:

- Step-up Substations at the Power Stations to raise the voltage from (11 - 21 KV) to 132 KV or 275 kV.

- Step-down Substations to lower the voltage from 275 kV to 132 KV.

- Step-down Substations to lower the voltage from 132 KV to 33 KV.

- Step-down Substations to lower the voltage from 132 KV to 11 KV.

- Step-down Substations to lower the voltage from 33 KV to 11 KV.

- Step-down Substations to lower the voltage from 11 KV to 415/240 Volts.

- These types of sub-stations are interconnected amongst themselves as well as with the Power Stations on one side and with the consumers on the other side by various networks of different voltages levels. The following resume outlines the main characteristics and functions of these networks:

- The primary transmission EHV network (275 kV) which consists mainly of double circuit overhead lines having quadruple bundle conductors supported on steel towers. In built-up areas, this network comprises 275 kV underground cables of special design. This network has two functions - firstly to transmit bulk Power Station to major center of consumption (the 300/132 KV Substations) and

secondly, to interconnect the Power stations in perfect synchronism whereby all generators maintain on identical speed.

- The secondary transmission HV Networks (132 KV and 33 KV) which consists in open areas, of double circuit overhead lines having single of double-bundle conductors supported on steel towers and in built-up areas of underground cables of special design. The main function of this network is to transmit medium amounts of power from the 300/132 KV and 132/33 KV substations to the distribution network (11 KV and 415/240 Volts) and sometimes to large consumers.

- Street-lighting network which consists of L.T. Cables emanating from 11 KV / 415 - 240 Volts sub-station to supply street lighting lanterns on poles and masts.

1.5 GCC Grid Systems Interconnection

An idea to connect all six Gulf Cooperation Council Countries (GCCC), Kuwait, Saudi Arabia, Qatar, Bahrain, United Arab Emirates and Oman, was put down in the early eighties because Saudi Arabia uses the 60 Hz network, where the other five countries uses the 50 HZ system. However, with the technological advancement of the HVDC system, this idea gained further support in the nineties. Recognizing the benefits of interconnection of their power grids, the six countries have agreed in 1997 to establish HVDC connection as economical and feasible alternative.

AC interconnection of the 50 Hz systems of Kuwait, Bahrain, Qatar, UAE and Oman was built with a back-to-back HVDC interconnection to the 60 Hz Saudi Arabian system. The interconnection was justified based on reserve sharing between the systems and the opportunity for trading electricity between the member countries. After

Fig. 1.5 Route and layout of the GCC interconnection

investigating different options for financing the Project, it was decided to finance the Project with funds from the member countries. The electrical grid system interconnection between the GCC states is shown diagrammatically in Fig. 1.5.

The Interconnection Project consists of the following high voltage lines and the associated substation:

- A double-circuit 400 kV, 50 Hz line from Al Zour (Kuwait) to Ghunan (Saudi Arabia) with an intermediate connection at Fadhili (Saudi Arabia).

- A back-to-back HVDC interconnection to the Saudi Arabia 380 kV, 60 Hz, system at Fadhili.

- A double circuit 400 kV comprising overhead lines and submarine link from Ghunan to Al Jasra (Bahrain).

- A double circuit 400 kV line from Ghunan to Salwa (Saudi Arabia) and associated substations.

- A double circuit 400 kV line from Salwa to Doha South (Qatar) and associated substations.

- A Control Centre located at Ghunan.

- A double circuit 400 kV line from Salwa to Ghuwaifat (UAE).

- A double and a single circuit 220 kV line from Al Ouhah (UAE) to Al Wasset (Oman).

A Control Center for the GCC Interconnection, which is also capable of communication with the national centers of the Member Countries, will also be installed and, when eventually completed, the interconnected substations will be suitable for operation in a coordinated and stable manner through this Control Center. The Center will provide the control and monitoring of the exchanged power between the countries.

1.6 Control Centers

The fast development of the Electrical Networks in Kuwait and to co-ordinate the activities of Power Generation, Transmission and Distribution and to secure the continuity of the supply to the consumers in reliable and economic way, the Ministry decided to construct National Supervisory Control Center and distribute Regional Control Centers according to the geographical area and define their responsibilities as described by:

1. National Control Center Jabriya:

This Center was constructed by Siemens in 1980 and upgraded by the same company in 1994. This Center is responsible for the supervision and control of 275 kV, 132 kV Electrical Network and supervises all Generating Stations in the country.

2. Jabriya District Control Center:

This Center started operating from 1972 and has been upgraded by Siemens on 1994. This Center is responsible for the supervision and control of 132, 33 and 11 kV Network which lies in the area surrounded by Fourth Ring Road in north and Gulf Street on the east and Sixth Ring Road with Sabah Al Salem Area to the South and Al-Ghazali Street with Riqaee and South Ardiya areas to the west.

3. Town District Control Center:

This Center started operating in 1988 and has been upgraded by Mitsubishi on 20/10/99. This Center is responsible for the supervision and control of 132, 33, 11 kV Electrical Network which lies in the area surrounded by Fourth Ring Road in the south and Al-Ghazali Street to the west including Shuwaikh Industrial area and Hospitals area and Gulf Street on the north and east.

4. Shuaiba District Control Center:

This Center was constructed by Siemens in 1988 and upgraded by the same company on 30/10/99. This Center is responsible for the supervision and control of 132, 33, 11 kV Electrical Network which lies in the area surrounded by Sixth Ring Road in the north (excluding Sabah Al Salem Area) and the Kuwait Saudi border in the south and Gulf Street on the east and Faisal Bin Abdul Aziz Motorway on the west.

5. Jahra District Control Center:

This Center constructed by Cogelex in 1994 and upgraded by the same company on 24/7/2002. This Center is responsible for the supervision and control of 132, 33, 11 kV

Electrical Network which covers all the area on western side starting from Sulaibikhat and includes Ardiya, Andalus, and Sulaibiya.

1.7 Basic Requirements of the Supervisory Control Centers

The Control Centers require some very sensitive, accurate, reliable and advanced systems which can be divided into the following categories:

- Information Collection Systems.

- Telephony Systems and Peripherals.

- Communication System and Peripherals.

- Auxiliary Power Supply System and Peripherals.

- Computer System & Peripherals.

Next, a description of each category is given.

1. Information Collection System:

This system consists of a microprocessor with special programmes to collect and send all required information and measurements from the Power Generating Stations and Substations to the Control Centers and to receive the instructions issued from the Control Centers and to ensure their correctness and follow up their execution. The sending and receiving is to be very fast using different communication equipment.

2. Telephony System and Peripherals:

The MEW utilizes redundant communication facilities in different Power Generating Stations and Substations to support the operating engineers for coordinating the operation of the power system and taking the corrective measures in case of any forced

outage. Telephony network for each Center and are interconnected to each other to increase the efficiency of these networks.

The Telephonic System of each Center consists of a main PABX installed in the Control Center while the PAX' s are usually installed in some of the major sub-stations connected to the same Center. All PABX's available in the control Centers are connected to the Ministry of Communication Telephony network to have access to direct outside communication in addition to the internal communication. It is to be noted that the capacities of these PABX's differ according to the operational requirements of each Center. With regards to the Peripherals to the main PABX's consists of Multi-channel Duplicated Voice Recording Equipment connected to the telephonic lines and is used to record all the conversation exchanged between the Control Room Operation Engineer and others round the clock. By this way the operation engineer can analyze the instructions and to issue the required remedial actions.

3. Communication System and Peripherals:

It has been considered in the designing of the Communication System that all major substations data is transmitted via duplicate channels and the equipment differs according to the routes used and the wired or wireless transmission media. Separate Pilot Cables or communication cables are used with underground cables for power transmission which are laid alongside on the same route for the transmission data in the frequency range of 4 KHz and in case of Overhead Lines, these lines are used for data transmission using Power Lines Carrier equipment which operate in the frequency range of 35 – 500 KHz. With regards to wireless media, the equipment installed is Microwave which operate in the frequency range of 7.5 GHz. Some major substations collects the data of their satellites and transmits and receives the information in the same way as

described earlier. Digital Microwave Equipment which operates in the frequency range 18, 19 Hz has been installed between one substation and Shuaiba DCC. In case of substations located in far areas and for which the previously described medias are not economical to be used then the equipment using the Ultra High Frequency (UHF) wireless operating in the frequency range of 367.925 – 399.5 MHz is installed for the provision of telephonic services with the Control Centers.

Ministry started in 1997 to use fiber optic technology for transmission of data and telephony with a link between NCC and MEW Head office due to its superior features such as the speed, capacity for data transmission and diversity of information transfer (analog and digital) in addition to efficiency, integrity and availability of communication channels.

Conventional ground wires, on eight 33 KV OHL links majoring 56 km have been replaced with optical ground wires (OPGW). The replacement of conventional ground wire for many existing 300 & 132 KV overhead lines with optical ground wires (OPGW) is underway.

4. Auxiliary Power Supply System:

In view of the important role played by the supervisory control equipment and the continuous operation even in case of loss of electrical supply to the station an auxiliary power supply system should be provided in the Control Center and each station. Auxiliary system in the substations consists of battery charger which converts the electrical energy from the alternating current to the direct current and stores them in battery. These batteries provide the required energy in case of loss of supply to the charger for a period between 10 to 12 hours. The Auxiliary Power Supply System as provided for the Control Centers consists of the following:

Uninterruptible Power Supply System which feeds the required power to the computers and their peripherals.

Auxiliary Power Supply System for the Communication and Telephony Equipment and their Peripherals which is identical to what is provided in the substations with the only difference that their capacities are larger matching to the equipment requirements present in the Control Centers.

5. Computer Systems and peripheral:

The duty of the Control centers depends mainly on the computer systems, which communicate with the remote terminal units and power stations. These systems were designed as Duplex System for work continuity. The National Control Center works through special programs to display and analyze the data (SCADA Functions) in addition to special programs for the Energy Management System. However the duty of the district centers is restricted on data display and analysis (SCADA Functions) besides the transmission of some data to the National Control Center in order to use it for the Energy Management System.

6. Internet Service Provider:

The National Control Center is acting as the Internet Service Provider. A complete domain has been registered for the use of the Ministry of Electricity & Water to serve the e-mail services. An official web site has been developed under the name www. mew.gov.kw. The site includes many general information such as Ministry of Electricity & Water telephone directory, steps and procedure getting energy services, water and electricity saving advises. Billing information, training programs and load gauge.

7. Energy Saving Campaign:

National Control Center participated in the Energy Saving Campaign by exporting information regarding energy consumption related to areas of Kuwait from the National and District Control Centers SCADA system to Kuwait National Campaign Control Room. This step contributed among others in reducing the consumptions of the load.

8. Upgrade of Internet Infrastructure:

Currently, MEW is undertaking a project to upgrade the Infrastructure at the Ministry and implementation of United Communication Systems in addition to enhance the overall network security. The solution will combine upgrading the network infrastructure at MEW head office by providing fully redundant, highly available and secure network with 10 Gigabit Ethernet Fiber backbone. The solution will also include installation of a pilot Unified Communication system with different types of needed components and IP Phone. The complete system will be highly secure, voice and video ready. IP Telephony and Video conferencing will be implanted as part of Unified Communication.

1.8 MEW Future Projects

Government authorities are also planning to bring additional capacity over the next few years, with the private sector expected to play a major role in this expansion.

According to the displayed data in section 2, peak demand for power is expected to increase at a rate of 6-8% per annum over the next few years, reaching 14,256 MW by 2014. Peak demand usually occurs in the summer, when heavy use of cooling systems can strain the power grid. According to some estimates, air conditioners account for around 70% of Kuwait's peak power demand. By the beginning of June all power

station will be committed according to cover the load. Table 1.5 depicts the future power stations under study with the associated capacity to cover the future increasing demand. Moreover, Table 1.6 indicates the total number of the required projects and their associated costs.

Table 1.5 Future Expansion Planning in Power Plants

Project	Capacity
Az-Zour Power Plant (4 Stages)	4800 MW+280 MIGD
Al-Julaia Power Planr	1000 MW
New Shuwaikh Power plant	2000 MW
New Shuaiba South Power Plant	1400 MW+50 MIGD
New Doha East Power Plant	2300+100 MIGD
Total to be added	11500 MW + 430 MIGD

Table 1.6 Expansion Planning Projects and the Required Cost

Sector	Total No. of Projects	Total Cost of Projects MKD
Planning & Training	9	85
Power Stations & Desalination plants	13	2800
Water Projects	27	1129
Control Centers & IT	20	158
Electrical Transmission	62	2400
Electrical Distribution	9	550
Operation & Maintenance Power Stations	8	325
Consumer Affairs	7	125
Technical Services & Main Workshops	6	35
Total	134	7500

Indeed, in late June 2012 six gas-powered turbines have been activated, which will be able to generate 1400 MW of electricity, equivalent to roughly 10% of Kuwait's current total capacity. The plant is expected to enter its full combined-cycle commercial operations by the end of 2012, at which point its total capacity will be around 2000 MW. A combined-cycle plant is more efficient because waste heat is recovered and converted into steam, which is then used to drive a steam turbine to produce additional power. Owned by the state, the facility will be operated and maintained by General Electric for a period of seven years from the commencement of full commercial operations.

The consumption of electrical energy per sector in Kuwait indicated that the domestic sector has the highest share of this energy. In addition, there has been an escalating increases in the demand for electrical energy and in the national cost for energy production. Therefore, the government of Kuwait continues to encourage the development of a code of practice for energy conservation in buildings and to utilize renewable energy.

1.9 Renewable Energy in Kuwait

In its broadest sense, renewable energy can be understood as energy generated from ecological resources which are naturally replenished. Renewable energy sources include sunlight, wind, rain, tides and geothermal heat (for electricity generation), organic-based biofuels (for heating and transportation) and traditional biomass (fuel wood and agricultural waste) (for cooking and heating). The focus of this chapter will be on renewable energy in the context of larger-scale electricity generation, which at a GCC level has already achieved some success and has the potential to achieve significantly

more. Although nuclear power generation is often discussed alongside renewable energy, it is technically not a renewable source of energy and accordingly will not be discussed in this report other than to note that certain GCC countries have announced an intention to include nuclear energy in their future energy mix.

Several renewable energy technologies have made significant penetrations in the world energy market. These technologies include solar (solar thermal and photovoltaic), wind, biomass, geothermal, hydro, wave, tidal and ocean thermal resources applications. The increased interest and rapid growth in these applications have been stimulated by a significant drop in cost over the previous decades, and technical improvement in their efficiency, reliability and life time. Other advantages of renewable energy applications are their modularity, large solar potential in developing countries especially in MENA region, favorable land-use features and ease of decommissioning.

The leading technical improvements in this field includes: manufacturing, innovations, improvements in solar system design, conservation, efficiency improvements, aerodynamic advances in wind turbine design and other mechanical and electrical innovations. In this work, the renewable energy applications and its potentials in MENA region is discussed and the needed steps to exploit and apply these sources in Kuwait is studied.

The benefits of developing renewable energy in MENA region or in anywhere else can be categorized in four headings: sustainability, environment, diversification, and economics. The following are some of these benefits:

- Renewable energies are sustainable sources of energy. Renewable technologies are designed to run on a virtually inexhaustible or replenishable supply of natural fuels. The primary long term benefits of renewable technologies is that

once a renewable energy project has been constructed and fully operated, it become a permanent component of the national energy system.

- Renewable sources promote energy diversification. Development of a diverse portfolio of generation assess reduces a country dependence on any one particular form of technology or fuel.

- Renewable energy technologies have a very small impact on environment compared to fossil fuel. The discharge of unwanted or unhealthy substance in air, ground and water commonly associated with other forms of energy use can be reduced significantly by using renewable energies.

- Renewable energies have values beyond they generate. Renewable energy systems are modular, flexible and can be installed anywhere and in any size. Investment in locally available renewable energy generates more jobs, greater earnings and higher output. The renewable energy industry provides a wide range of employment opportunities, from high technology manufacturing of PV components to maintenance jobs at solar thermal or wind systems. Several renewable energy technologies and applications are of relevance to developing countries. However, local and country-specific conditions including the availability of renewable energy resources, cost of conventional energy, capital cost of equipment, as well as other factors, influence the commercial viability of renewable energy technologies. The following sections present brief description of renewable energy technologies that could be utilized in Kuwait and its applications.

1.9.1 Solar Energy

1.9.1.1 Solar Energy Applications

Energy from the sun travels to the earth in the form of electromagnetic radiation similar to radio waves, but in a different frequency range. In a clear day, the amount of solar radiation available at earth surface in the direction of the sun is typically 1,000 W/m2. At any particular time, the available solar energy is primarily dependent upon how high the sun in the sky and the current cloud condition. There are many ways that solar energy can be used effectively. Applications of solar energy can be grouped into three primary categories: thermal applications, electricity production, and chemical processes. The most widely used applications are for water heating. Uptake of electricity producing solar technologies is increasing for the application of photovoltaic (primarily) and concentrating solar thermal-electric technologies. Due to recent advances in solar detoxification technologies for cleaning water and air, these applications hold promise to be competitive with conventional technologies. The economics of solar energy has witnessed drastic improvements in the past few years. This improvement came especially in the form of increased conversion efficiency, and reductions in the cost of production.

1.9.1.2 Solar Energy Potential

There are different ways to reduce the cost of electricity in Kuwait. One of these ways is to set up a Heat Rate improvement Program using the method that suits co-generation plants. Also, Demand Side Management program should be set up to recover some of the costs and to encourage conservation. Incremental Heat Rate must be used to figure out which generating unit is most economical to serve the portion of the load increase.

Also, the proposed electrical tie between the six Gulf States could play a big role in saving these countries some future capital investments. A Power Pool should be formed to determine the most economical way to serve any load in any area. Ways to exploit the tremendous solar energy and other renewable energies like Fuel Cells should be considered and studied for their feasibility in Kuwait. Power plants generate adverse environmental and health impacts on the short, medium and long terms. Such impacts need to be addressed, assessed and monitored compared to clean energy resources.

Climate change, rising energy prices and technology advances in renewable energy utilization are all forces for reshaping the collective mindset of consumers, turning many from "passive ratepayers" to highly informed, environmentally conscious customers who want a role in using power. And now, with the emergence of the technologies that make smart grids possible, companies can provide their customers with the information and control they need to actually change their behavior patterns and reduce usage and costs that show up on the utility bill. Many digital companies are helping utilities by adding a layer of digital intelligence to their smart grids.

These smart grids use sensors, meters, digital controls and analytic tools to automate, monitor and control the two-way flow of energy. A power company can optimize grid performance, prevent outages, restore outages faster and allow consumers to manage energy usage right down to the individual networked appliance. Smart grids can also incorporate new renewable energies such as solar and wind power, and interact locally with distributed power sources, or plug-in electric vehicles.

The potential of solar energy resources is excellent in Gulf countries with an annual global solar radiation varying between 4 to 8 kWh/m2. The region also enjoys high direct normal radiation and low average cloud cover. The solar energy irradiated on the
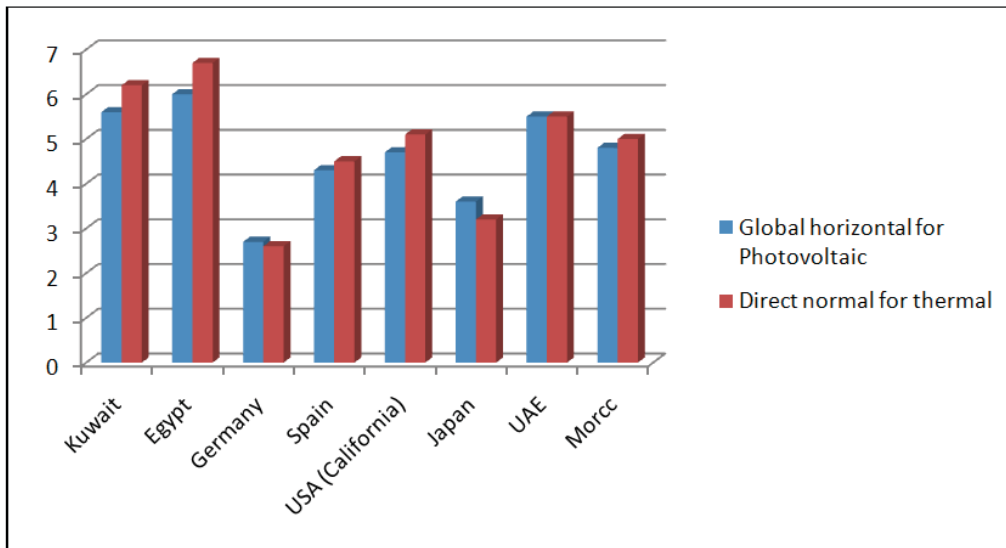
Fig. 1.6 Global horizontal and direct normal solar radiation [1.4]

ground is equal to 1-2 barrels of fuel oil per square meter and year. This magnitude of resource can be used both in solar thermal applications and photovoltaic systems. Thus, both distributed rural and centralized urban demand can be covered by solar energy technologies. Fig. 1.6 shows the global horizontal solar radiation and direct normal radiation in Kuwait compared to other countries. It is clear that Kuwait has a high solar potential which can be utilized for electricity generation.

It is well known that Kuwait has no fresh water resources. However, Kuwait has an abundance of solar energy capability. Solar energy use has been limited till now to experimental, use and research purposes only. Solar energy could be used effectively in different applications like Water Heating, lighting…etc. In other words, the use of renewable energy is virtually very limited and needed to be thought of and considered for supplying domestic loads.

Kuwait has been collaborating with local, regional, and international organizations and companies to meet the new demands of power. Kuwait has gone above and beyond establishing power supplies from various sources. Among these sources, Kuwait is

working on nuclear energy, and wind energy power. Having signed a 5 year deal with Japan, for instance, nuclear power is estimated to make up 15- 20 percent of the total electrical power supply. Another source Kuwait is considering to face power shortage is solar and wind energy. As an example of innovative power resources is Solar Power. Because of high solar irradiation in the regions, State of Kuwait is resorting to buy Solar PV Systems.

With the ministry of electricity and water estimate the demand for power to climb to 20,000MW by 2015 and 26,000MW in 2020, Kuwait plans to invest billions in doubling its installed capacity through a number of projects by 2017, from currently 13000MW to 27,040MW.

As a means to relieve the power shortage in the foreseeable future, the government of Kuwait has accepted a proposal to link up with the grids of other GCC countries. In theory the grid linkup would provide each GCC country with additional spare capacity to handle demand during summer. However, as observers have pointed out, peak demand is the same throughout the GCC and without plans to provide greater spare capacity the scheme seems unlikely to achieve its stated objective. Upon completion of the project, Kuwait and Saudi Arabia will receive 1,200 MW of power capacity each, UAE will receive 900 MW, Qatar 750 MW, Bahrain 600 MW and Oman 400 MW. The discrepancy between the amount of electricity generated and/or imported and the amount consumed and/or exported is accounted for as loss in transmission and distribution.

Owned by the government of Kuwait, the Sabiya facility is the largest power plant in Kuwait and among the largest in the region. When the plant enters combined-cycle operation by end 2012, the total plant output will be more than 2,000 megawatts. A

combined cycle plant dramatically boosts efficiency because waste heat is recovered from the exhaust of the gas turbine, converted to steam and then fed to a steam turbine to provide additional energy output.

The six gas turbines in the plant utilize emission-reducing technology that lowers annual Cos and NOx emissions by significant margins, which support Kuwait's clean air goals. In the hot arid region of the Arabian Peninsula including Kuwait, fresh water is not available in adequate quantity in its natural form. Multi-stage flash (MSF) and reverse osmosis (RO) are two desalination processes currently applied in different countries to produce fresh water. These desalination processes need large amounts of basic thermal and/or electrical energy for fresh water production from seawater or underground brackish water. Primary energy requirement of MSF is thermal energy in the temperature range of 80-120°C. A smaller amount of electrical energy is also needed to operate miscellaneous pumps and controls. The RO system, unlike the MSF system, needs only mechanical or electrical power. Solar energy can be effectively used to produce the required low-grade thermal energy in a solar thermal or (PV) system.

The use of PV as the power source for pumping water is one of the most promising areas in photovoltaic applications in Kuwait. With the increased use of water pumping systems, more attention should be taken to their design and optimum utilization in order to achieve the most reliable and economical operation. Thereby, the water pumping system consists of the PV array, DC motor, centrifugal pump, a storage tank that serves a similar purpose to battery storage and a maximum power point tracker to improve the efficiency of the system. The pumped water is desired to satisfy the domestic needs in remote areas in Kuwait.

1.9.2 Potential of Solar Power Generation in Kuwait

- Compatibility of Power Availability with National Power Demand

    o Power demand in Kuwait is maximum during the summer months and during sunshine hours.

    o Maximum power availability from solar systems is also available during the same period.

- Plenty of Barren Land

    o Kuwait has plenty of desert land that is not being used.

    o An area of 5 km^2 or 0.03% of Kuwait land area is adequate to generate 500 MW solar power.

The increasing level of renewable energy penetration into public grid has recently emphasized the importance of accurate renewable parameters (solar radiation, wind speed..) forecasting to utilities and independent system operators (ISOs). System operators are required to balance generation and load within a very tight band. This means that if load is rising, or wind power is declining, other generation must rise to keep the system balanced. Fig. 1.7 shows typical time frames that affect the operation of the power system. Typically the most important time frames are for unit commitment (days) and scheduling (daily). Large thermal units (e.g., those driven by steam turbines) need long cold start times to synchronize them to the grid and start generating electrical energy. Because of this, utilities and ISOs need to know a day-ahead how much load is anticipated throughout the next day. With large penetrations of renewable power, it also becomes essential to know with acceptable accuracy what the total renewable power production on the system will be during each hour. When renewable power forecasts are lower than what occurs, the system operator may have to turn on additional units that
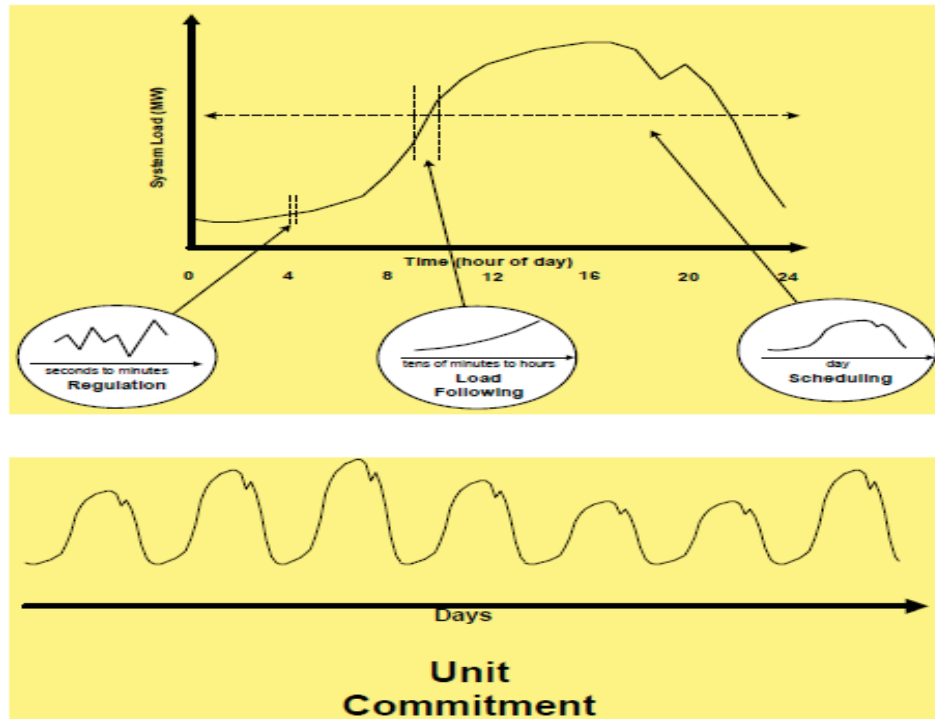
Fig. 1.7 Time frames of generation planning

were not needed, thereby increasing operating costs. When renewable power forecasts are higher than what occurs, the system operator may not have committed enough generation in advance and will either have to run expensive fast-start gas turbines or in some cases shed load. The shorter term forecasts in the "load following" time frame are also very important in balancing load, especially when renewable power may be changing rapidly in magnitude either ramping up or down.

Accurate information on the meteorological data at Kuwait is very essential to the development of renewable energy based projects. This information is used for project design, in component layout, cost analysis and in calculations of the project overall efficiency. In particular, the solar radiation, wind speed, the clearness, in addition to other meteorological information such as humidity and, temperature, are extremely

important to assess the feasibility of utilizing renewable energy for electricity generation.

1.10 Renewable Power Forecasting Techniques

Penn State/NCAR fifth-generation mesoscale model (MM5) 4D-Var system is the most advanced system that was available to weather forecast [1.13], [1.15]. As shown in Figure 1.8, MM5 has been applied to assimilate zenith delay observations from Global Positioning System satellites [1, 16] and to assimilate cloud-cleared brightness temperatures from Geostationary Operational Environmental Satellite (GOES) sounders [1, 17]. The MM5 produces very detailed and accurate simulations of tropical cyclones when high-resolution and advanced physical parameterizations are used [1, 13], [1, 17]. Due to current limitationof computer resources, weather control 4D-Var calculations were restricted to a horizontal grid spacing of 20 km.

The parameterizations of surface fluxes, radiated transfer, and cumulus convection are currently limited in the MM5 4D-Var system. This technique can be applied to both operational data and historical cases to aid in the scientific learning and pattern recognition of forecasters. Renewable generation forecasts cover a wide range of time frames. Typical power forecasts time frames include day-ahead hourly averages and hourly or more frequent same day average forecasts. Power forecasts valid for periods beyond several hours from the forecast origination time are developed by a two-step process. First, Solar radiation and wind speed forecasts at renewable plant sites are derived from numerical weather prediction model output. A wide range of models are used by the various commercial firms as the basis for the speed predictions.

A recent trend in commercial forecasting is to use an ensemble of model output that often includes the Weather Research and Forecasting model and large scale national models such as the Global Forecast System. Ensemble results provide an indication of the uncertainty of the renewable parameters and therefore power production forecasts that are quite important to utility system operators. The forecasted solar radiation and wind speeds must then be converted to forecasted power output in megawatts. This information will then be used in utility operations such as for unit commitment and dispatch of the conventional resources. This is not a straightforward process. The most important problem is developing an accurate power production curve (the production of energy by renewable resources.
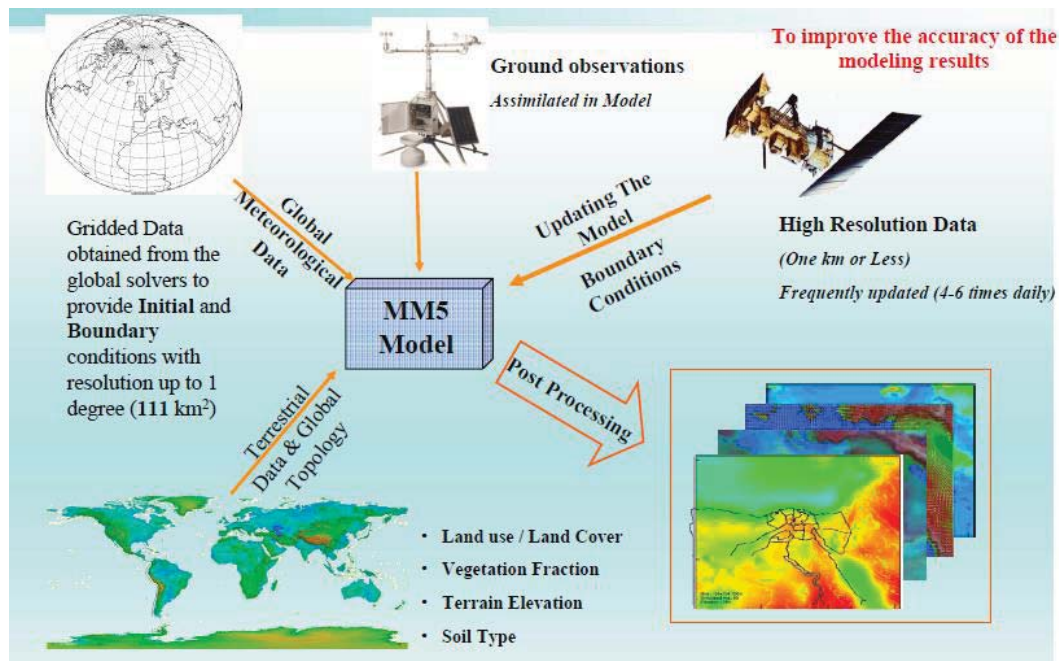
Fig. 1.8 Weather forcast using MM5 model [1.13]

In collaboration with the Army Test and Evaluation Command (ATEC), NCAR has developed a Real-Time Four Dimensional Data Assimilation (RTFDDA) and

forecasting system. The RTFDDA system is built around the Penn State/NCAR Mesoscale Model version 5 (MM5) and the Weather Research and Forecasting (WRF) model. RTFDDA is capable of continuously collecting and ingesting diverse synoptic and asynoptic weather observations from conventional and unconventional platforms, and provides continuous 4-D weather analyses for accurate nowcasts and short-term forecasts for mesoscale regions. Operational RTFDDA systems have been implemented at seven ATEC test ranges and tens of other DoD, public and private applications in the last seven years, providing rapidly updated, multi-scale weather analyses and forecasts with the fine-mesh domain having 0.5 - 3 km grid increments. The observational data ingested by the system includes WMO standard upper-air and surface reports, wind profilers, satellite cloud-drift winds, commercial aircraft reports, all available mesonet data, radar observations, and any special instruments that report temperature, winds and moistures. Furthermore, the system has been expanded to include the following new modeling and data assimilation capabilities that are highly valuable for wind energy applications: a) Ensemble RTFDDA, which is a multi-model, mesoscale data analysis and forecasting system that samples uncertainties in the major components of RTFDDA and predicts the uncertainties in the weather forecasts by performing an ensemble of RTFDDA analyses and forecasts; b) LES (Large Eddy Simulation) modeling, which is nested down from the RTFDDA mesoscale data assimilation and forecasts to LES models with grid sizes of ~100 m for wind farm regions using GIS 30-m resolution terrain; and c) HRLDAS (High-Resolution Land-Surface Data Assimilation System), which assimilates high-resolution satellite vegetation and soil data to generate high-resolution, accurate state of soil moisture and temperature. This modeling system has been applied for supporting wind energy prediction at wind farms operated by Xcel

Energy. The modeling capabilities will be described and demonstrated through case studies at selected wind farms.

1.10.1 The Characteristics of Solar Radiation

The various solar energy applications/technologies are influenced by the character of the resource, such as its directional nature (whether the sunlight is direct of diffuse — by clouds, for example — and it's angle of incidence on the collector surface), its spectral nature (what specific wavelengths of sunlight the collector technology responds to most effectively), and its variability. The variability characteristic can be in the span of a few minutes (how clouds will affect power production), seasonal (how climate patterns will affect the solar resource), inter-annual (how the resource will vary year to year), or even decadal (how climate change could affect the resource).

This solar radiation computation program requires only a latitude value to predict sunrise, sunset and sunshine period to compute the solar radiation equations. A new predicted empirical equation has been added to this script to give a good agreement and it has been tested for three different locations in the middle east which are Kuwait, Riyadh and Jerusalem. The incident solar radiation values, based on monthly average daily amounts can be obtained from the available references or the 22 years average values which are recorded in NASA website [1.6].

Since the earth-sun distance varies each season, the apparent extraterrestrial solar irradiation changes during the year. Therefore, the solar irradiation intensity depends on the number of the day in the year [1.3]. The average daily extraterrestrial solar irradiance is given by:

$$\overline{S}_{ET} = \frac{33048}{\pi}\left[1+0.034\cos\left(\frac{360n}{365}\right)\right]\times\left(\cos L \cos\delta \sin H_{SR} + \frac{\pi}{180}H_{SR}\sin L \sin\delta\right)$$

$$(0.1)$$

In clear sky atmosphere calculations, the clearness index Kt is defined as the ratio of the horizontal insolation S_H at the site to the ET insolation S_{ET} on a horizontal surface above the site and just outside the atmosphere and is given by:

$$K_t = \frac{S_H}{\overline{S}_{ET}} \qquad (0.2)$$

The relationship between the forecasted sky cover parameter SK and the global index, GHI/GHI$_{clear}$. Fig. 1.9 (a) is a plot of forecasted SK against measured global index for all forecasts ranging from 4 to 8 hours [1.14]. Unlike the quasi-linear relationship observed for the satellite-derived cloud cover CI (see Fig. 1.9 (b)). The relationship between global irradiance index GHI index and cloud index CI represented by ground-observed cloud cover is markedly non- linear. Kasten and Czeplak [1.5] had proposed the following expression between the global index and ground-observed cloud cover:

$$GHI\,/\,GHI_{clear} = 1-0.75\left(\frac{N}{8}\right)^{3.4} \qquad (0.3)$$

where N is the ground-observed cloud cover in octas.
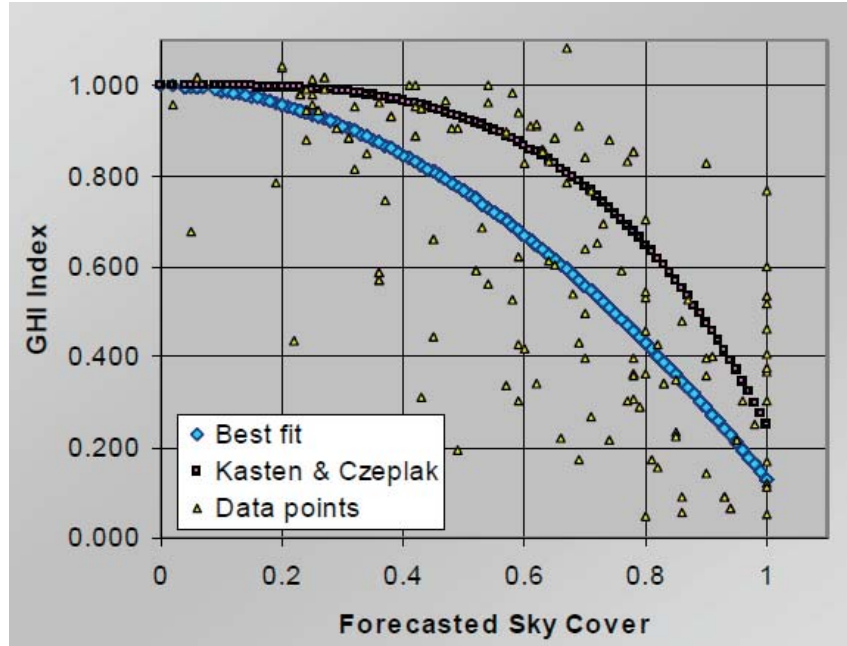
(a)
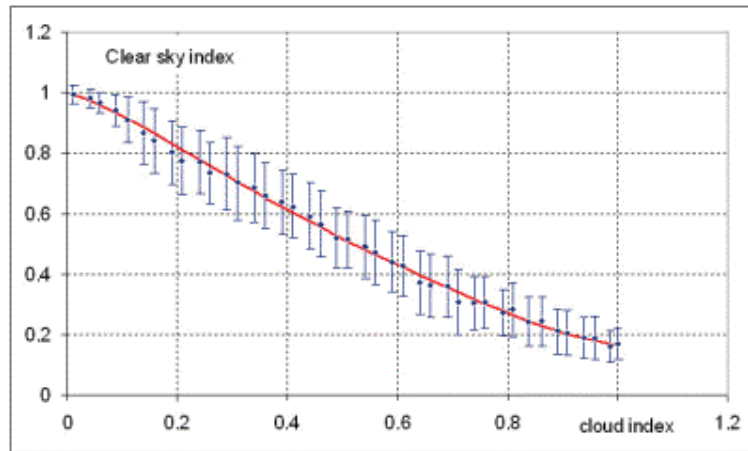
(b)

Fig. 1.9 (a) Relationship between 4-8 hours SK forecasts and observed global irradiance index (b) Relationship between satellite-derived cloud index CI and observed global irradiance index

Another approach using clearance index is applied to represent the effect of cloud on the global radiation. A high clearness index (Kt > 0.5) corresponds to clear skies, where most of the SR will be direct beam, while a low one (Kt < 0.5) indicates overcast

conditions with diffuse SR. A monthly averaged clearness index for the site of Kuwait can be obtained from National Aeronautics and Space Administration (NASA) website for Kuwait area over 22 years (1983 – 2005) [1.6], as given in Table 1.7.

Table 1.7: Monthly averaged clearness index in Kuwait area

Latitude 29.33^o Longitude 47.5^o	22 Year Average K_t
January	0.52
February	0.57
March	0.56
April	0.56
May	0.62
June	0.69
July	0.68
August	0.67
September	0.65
October	0.60
November	0.50
December	0.47
Annual average	0.59

From the best curve fitting for the values of *Kt* in Table 1, the clearness index can be expressed to a good accuracy as a function of day number *n,* as

$$K_t = -3.807 \times 10^{-6} n^2 + 0.001124n + 0.6139 \tag{0.4}$$

The daily global SR on horizontal surfaces, *SH*, in Wh/m2, can be found from (1.2)

The hour by hour SR data is essential if the radiation on the horizontal surfaces is to be estimated. We can follow the same procedure as for the daily radiation except for expressing the hour angle in terms of solar time in hours (local apparent time, LAT) as in:

$$H = 15°(t - 12) \tag{0.5}$$

and letting the solar time t vary between sunrise time and sunset time according to the longitude of site. For the Kuwait area with a longitude of 47.5º, the standard sunrise and sunset times are 6:00 am and 18:00 pm, respectively, and ET S may be obtained from Kuwait Metrological Centre.

The consumption of electrical energy in Kuwait indicates that almost one half of the generated energy in Kuwait is consumed for domestic purposes. At the same time, most of the load in residential, industrial, and commercial areas is due to air conditioning (A/C) systems.

According to the maximum and minimum load distributions shown in Table 1.3 for the year 2010, Kuwait electrical load is characterized by high load in summer and low load in winter depending on the increase and decrease in the values of temperatures and relative humidity.

The meteorological data for Kuwait, latitude angle (L = 29.33º), longitude angle (γ = 47.5o), clearness index Kt (almost cloudless atmosphere for nine months), solar time t (varying from 6:00 to 18:00), and the corresponding hour angle H, has been used in the model and the intensity of daily and hourly global SR on horizontal surfaces SH in Kuwait area has been obtained as a function of both day number n (with a day number increment of one day) and time (with a time increment of one hour). These results can be obtained for any day of the year and for any hour of the day.

1.11 Solar cooling

Today, there are two main solar air-conditioning technology options: solar thermal air-conditioning, where the solar absorption cooling is the first type of this option and it is still practical for remote building in places where there is an excess of heat energy

available. Another option is the solar photovoltaic air-conditioning, by using electricity from renewable sources to power the conventional cooling equipment. ''On the other hand, the market introduction of photovoltaic systems is much more aggressive than that of solar thermal power plants; cost reductions can be expected to be faster for photovoltaic systems. [1.7].

The cooling demand generally follows the outside ambient air temperature. Normally, higher temperature leads to higher cooling load due to a heat transition through the building's envelope from hotter outside to a cooler inside of the building.

Solar air-conditioning systems can be divided into two groups of systems:'' solar autonomous systems and solar-assisted systems. In a solar autonomous system "all" energy used by the air-conditioning system is solar energy. In a solar assisted system the solar energy covers a certain fraction of the energy used by the air-conditioning system and the rest of the energy is provided through an auxiliary or backup system'' [1.7]. Only the solar-assisted systems are considered in this study.

Solar air-conditioning technologies are any air-conditioning system that use solar radiation as source of power to drive the cooling process in order to produce cold air for buildings. This can be achieved through solar thermal conversion or solar photovoltaic (PV) conversion. In PV air-conditioning systems, PV cells arranged in modules convert solar radiation to electric power which then drives a traditional compression chiller. Solar thermal air-conditioning technology converts solar radiation to heat power (through thermal collector) which is fed into a thermal cooling process or into a direct air-conditioning system.

1.11.1 Solar PV Air -Conditioning

PV air-conditioning system consists of three main parts: solar energy collection (includes PV cells) which converts solar radiation into electric power in order to drive the electric machine heat pump. This machine is any electric traditional air-conditioning system which converts the electric power to cooling power. The cooling power is distributed for space cooling either directly in a decentralized system or by a cooling coil and sometimes by a hidronic system [1.8]. The PV air-conditioning system can include a storage system (battery system) or it can be without a battery system.

Thermal air-conditioning systems can be divided in two groups [1.8]: a solar heat driven air-conditioning system which consists of a solar thermal collectors (high temperature or medium temperature hot water) where typically flat plate collectors, evacuated tube collectors or concentrated parabolic collectors are used. This converts the solar radiation to heat power. Then this power is provided to drive another system in order to produce cooling power for buildings.

This system can be either an electrical air-conditioning (such as traditional air-conditioning) or thermal air-conditioning (such as absorption/adsorption chillers) or both. The other type is a desiccant cooling system which uses water as refrigerant in direct contact with air and the desiccant dehumidification is combined with an additional cooling system which may be a conventional cooling coil or evaporative cooling.

The PV air-conditioning without a storage scenario consists of a PV–module, inverter, a compressed chiller and a system distribution. As shown in Fig. 1.10, the system set up of a PV air-conditioning with storage is similar to the first scenario, but it additionally has a storage (battery) system and a charge controller.

The PV module converts solar radiation into electric power as direct current (DC). The solar charge controller regulates the voltage and the current which comes from the PV module into the battery. This prevents from the overcharging of the battery and increases the battery life.

The inverter converts DC into alternating current (AC) which is needed to drive the compressed chiller. The battery stores the excess energy for supplying the compressed chiller when there is no enough solar radiation to cover the cooling demand. The compressed chiller converts the AC power to the cold air. The compressed chiller is supplied as a back-up with an electric AC power from the grid, when there is not enough DC power from the PV-array and the battery bank, especially at night, evening and morning of the day when there is no enough solar radiation to drive the compressed chiller. The first step in designing a solar PV air-conditioning system is to find out the cooling power and energy consumption that need to be supplied by the PV-array.
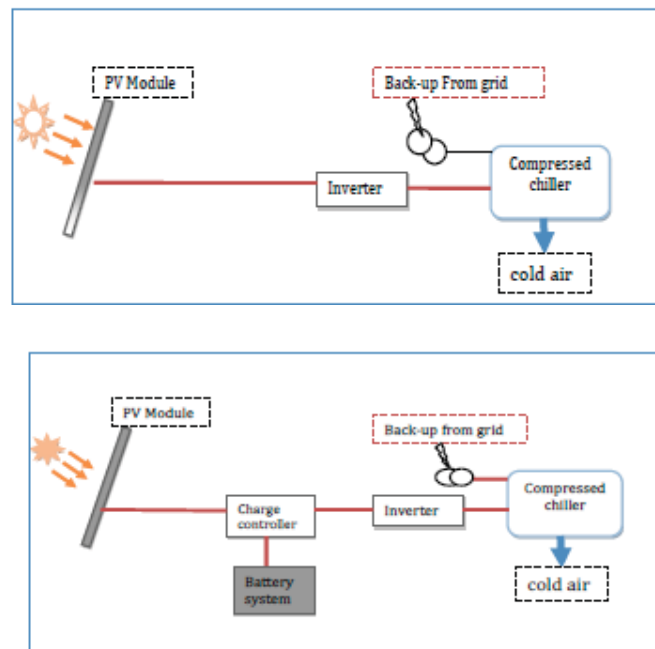
Fig. 1.10 Schematic flow diagram for solar PV air-conditioning with storage.

Energy produced by the PV array is accumulated and stored in batteries for use on demand. The battery system is designed for a PV air-conditioning with storage. In this scenario, when the electric DC power is higher than the electric power needed by the compression chiller. The battery accumulated and stored the excess DC power as electric energy. The solar charge controller regulates the voltage and the current which comes from the PV module into battery [1.9].

When there is no enough electric power coming from the PV-array and the battery system to cover the cooling power demands, the back-up system is designed to deliver the remaining needed AC power. The back-up system is assumed to have a direct connection to the electricity grid and to the compressed chillers. This connection is considered and designed for both PV air-conditioning scenarios without and with storage [1.10].

1.11.2 Solar Thermal Air-conditioning

The thermally driven air-conditioning process is the heart of every solar cooling system. Thermally driven air-conditioning systems are available on the market which commonly utilize sorption processes. For air-conditioning applications, mainly absorption chillers using the sorption pair Lithium bromide-water (LiBr-H2O) are applied [1.11] since they require a comparatively low temperature as heat input. Most of the thermally driven cooling system and solar assisted air-conditioning systems installed today are based on absorption chillers [1.11].

In this solar thermal system, an absorption chiller coupled with a solar heating system and an auxiliary energy supply as back-up electric heater is analyzed. In the assumed case, the collector converts the solar radiation into heat and then the pump delivers it to

the storage tank. The storage tank then supplies the absorption chiller with thermal energy to produce cold water. The coil and the fan system transfer the cooling power from cold water to the inside air of the building. A duct system distributes it in the building. If solar heat is insufficient e.g. at night or during cloudy days, the conventional back-up electric heater is connected directly with the storage tank can provide heat. The system components and design can be described as follows in Fig. 1.11:
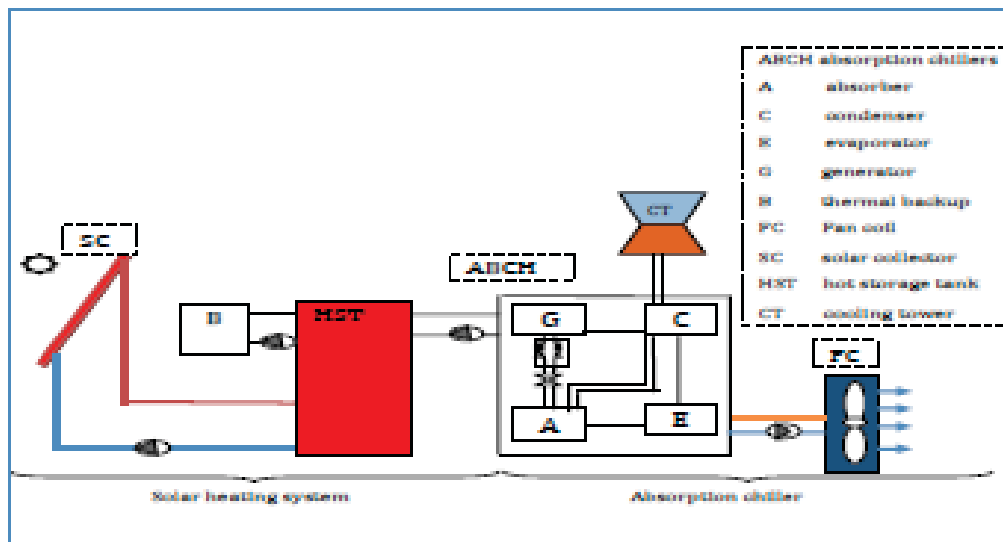
Fig. 1.11 Solar thermal air-conditioning system scenario, coupling of an absorption chiller with a solar heating system.

A solar collector is a special kind of heat exchanger converting the solar radiation into thermal heat which is carried by a working fluid, e.g. water which is flowing through the collector. There are three types of solar collectors which are typically used in a solar thermal air-conditioning systems: flat plate collectors, evacuated tube collectors and concentrated parabolic collector.

In the solar thermal air-conditioning system, the temperature level that should be supplied by the solar thermal collector depends on the cooling technology used. Flat plate collectors can be designed for applications requiring energy delivery at moderate

temperatures, up to perhaps 100 0C above the ambient temperature. The operation of absorption air-conditioning with energy from flat plate collectors and storage systems is the most common approach to solar cooling.

Flat plate collectors are fixed and there is no tracking system. The collectors should be oriented directly towards the equator. The collector's location in the northern hemisphere should be facing the south and vice-versa in order to maximize the amount of daily and seasonal solar energy received by the collector. The optimal tilt angle of the collector is an angle equal to latitude of its location [1.11]. However, in summer the tilt angle should be smaller than the latitude to receive more solar radiation.

The solar photovoltaic air-conditioning system stores the excess DC in batteries. Similarly, It is necessary to use a thermal energy storage tank, either heat or cold storage in thermal air-conditioning system.

These two alternatives are not equivalent in capacity, costs or effect on the overall system design and performance. The required capacity of a cold storage tank is less than that required of a heat storage tank because the heat storage has higher conversion efficiency than the cold storage tank. In addition, heat storage tanks can be used for other applications for example domestic hot water or space heating.

When there is no enough solar radiation (e.g. at evening, night or on cloudy days), it will be a necessary to have a back-up system for the cold production or to allow the solar air-conditioning system to continue.

Two different back-up approaches can be used to achieve this objective, either back-up heating or cooling systems. The back-up heating system usually uses burners (oil, gas or pellet) or electric heater connected directly to the heat storage tank. The back-up cooling system usually uses conventional vapor pressure cooling devices.

One of the main objectives of the solar air-conditioning systems is to save primary energy consumption. Recent studies have indicated that PV air-conditioning scenario with storage behaves and compensates the cooling demand better than the solar thermal air-conditioning with storage scenario and needs less storage to cover the same amount of cooling load demand. However, the storage system in the PV air-conditioning scenario is minor and the direct compensation is major. Therefore, the PV performance has to be analyzed under different weather condition in Kuwait.

1.11.3 District cooling

The extensive use of air conditioning for indoor cooling in offices and large commercial buildings in Kuwait represents a major part of the power and electricity consumption in that country. In Kuwait approximately 45% of the total annual exported electrical energy is consumed solely by air conditioning systems as a result of the very high ambient temperatures occurring between March and October. Furthermore, it was estimated that air conditioning systems represent about 62% of the peak electrical load [1.12].

This was motivated by the extreme climatic conditions in Kuwait and the necessity to reduce both maximum power demand and energy consumption whilst being economically feasible. To assess the potential of cool thermal storage, the air conditioning system for a typical medium size building in Kuwait, was studied with and without a cool thermal storage system. The recent studies demonstrate that internal ice-on-coil and chilled water storage systems are suitable storage technologies that can be implemented in Kuwait.

Air and water-cooled water chillers are commonly used for AC of medium and large sized buildings in Kuwait. Air-cooled chillers are generally favoured for medium size systems and water-cooled for large systems. In these systems, the chillers cool the water, and the cooled water is pumped through the piping system to the various air handling and fan coil units in the building. The fan in the air handling and coil units circulates the air in the ducting system and within the conditioned space. The return air from the room is then cooled and dehumidified by the cooling coils and returns again to the room.

Basically, in this process, the circulated chilled water in the cooling coil picks up the heats that is gained by the room, supply and return ducts, and fan motors, and is returned to the chiller for cooling in the evaporator. The refrigerant in the evaporator absorbs the heat of the return chilled in the chiller as it evaporates at a low temperature and pressure, and gives up this heat to the atmosphere as it condensates at a higher temperature and pressure.

In an air-cooled system, the power demand of the chiller is a strong function of building load and ambient dry bulb temperature. However, the power demand of the AHU and chilled water pumps (if constant speed motors are used in the system) are generally constant during the whole summer period irrespective of the building cooling load and weather conditions. In water-cooled systems the main components in the AC system that consume electricity are similar to those of the air-cooled systems but with the addition of the condenser water pumps and motors of the cooling tower fans.

MEW promotes the implementation of District Cooling in the new five cities coming up in Kuwait. One of them is a commercial city and the rest are residential cities. District Cooling is the concept of centralized production and distribution of cooling energy,

using chilled water delivered via an underground insulated pipeline to office, industrial and residential buildings to cool indoor air within a district. The district cooling is fast becoming a reality in the GCC states, which are suffering from high growing because of the need for comfort cooling, non-ozone depleting coolants, and cutting energy consumption.

By district cooling, the solar energy is gained through the collector and accumulated in the storage tank. Then, the hot water in the storage tank is supplied to the generator to boil off water vapour from a solution of Lithium Bromide and water. The water vapour is cooled down in the condenser and then passed to the evaporator where it again is evaporated at low pressure, thereby providing cooling to the required space. Meanwhile, the strong solution leaving the generator to the absorber passes through a heat exchanger in order to preheat the weak solution entering the generator. In the absorber, the strong solution absorbs the water vapor leaving the evaporator.

Cooling water from the cooling tower removes the heat by condensation. Since the temperature of the absorber has a higher influence on the efficiency of the system than the condensing temperature, the heat rejection (cooling water) fluid, is allowed to flow through the absorber first and then to the condenser. An auxiliary energy source is provided, so that hot water is supplied to the generator when solar energy is not sufficient to heat the water to the required temperature level needed by the generator.

More than 70 percent of the domestic energy consumption is spent on comfort cooling. By 2030, the demand will grow to 32,000 MW. Kuwait uses 350,000 barrels of oil per day to generate electricity, and in the next 15 years, this figure will climb to 1 million bpd. District cooling can cut power consumption by up to 30 percent.

The contribution of this report is to find solutions to the rationing of energy use with the aim to preserve Kuwait's oil wealth and to priorities future needs during the gradual shift towards the use of alternative and renewable energy in power generation, with emphasis on solar energy and PV generation. Solar energy as a renewable energy resource will play a major role in Kuwait's future energy supply. Kuwait has an abundance of solar energy capability [1.12].

1.12 Meteorological Data for Kuwait

To study the utilization potential of solar energy in Kuwait the meteorological data will be further explained in next section. These data sets were used to assess the performance of the PV panel and generate the results presented in this study.

The data file was hourly data included the horizontal solar radiation (beam, diffuse and global), ambient air temperature and relative humidity [1.6]. Figs. 1.12 to 1.20 represent the horizontal global irradiation, ambient air temperature, cloud cover, participation and relative humidity data for Kuwait.

1.12.1 Temperature

The hottest day of 2011 was July 9, with a high temperature of 50°C. The hottest month of 2011 was July with an average daily high temperature of 46°C.
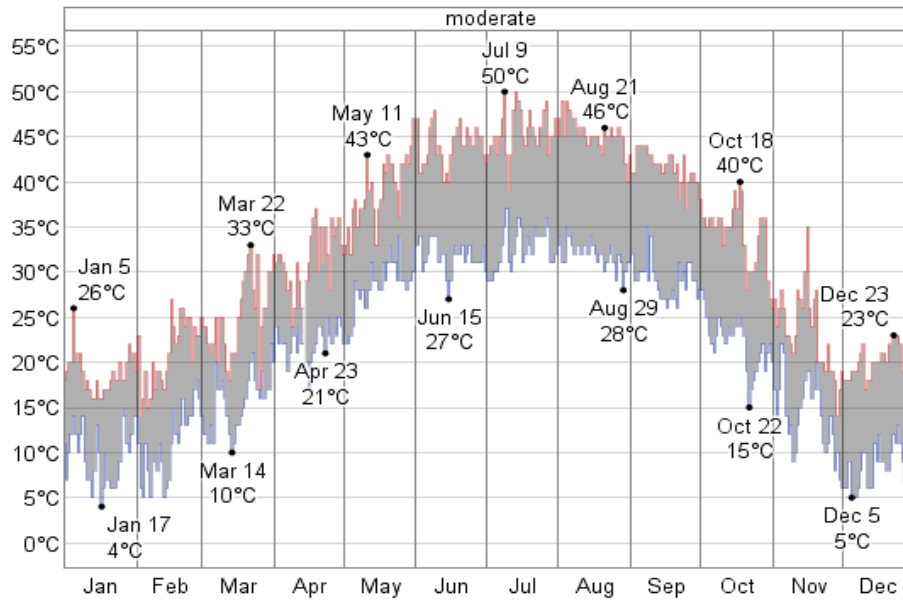
Fig. 1.12 Temprature variation in Kuwait

1.12.2 Cloud Coverage

The fraction of time spent in each of the five sky cover categories over the course of 2011 on a daily basis. From top (most blue) to bottom (most gray), the categories are clear, mostly clear, partly cloudy, mostly cloudy, and overcast. Pink indicates missing data. The bar at the top of the graph is gray if the sky was cloudy or mostly cloudy for more than half the day, blue if it is clear or mostly clear for more than half the day, and blue-gray otherwise.

The cloudiest month of 2011 was June, with 27% of days being more cloudy than clear. The longest spell of cloudy weather was from February 20 to February 25, constituting 6 consecutive days that were cloudier than they were clear.
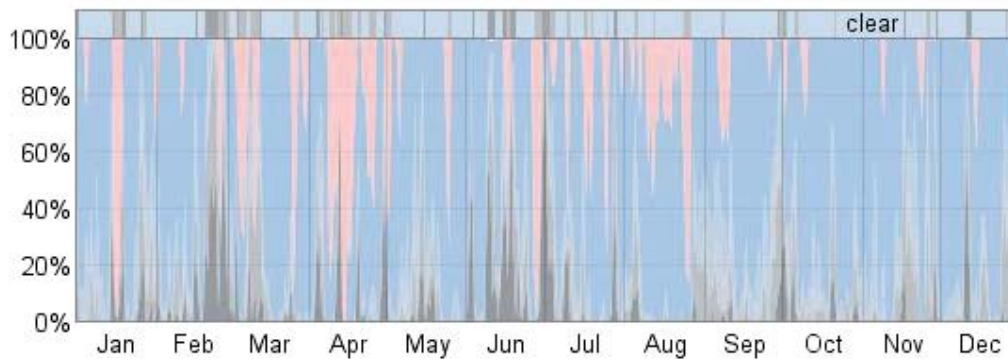
Fig. 1.13 Cloud Coverage in year 2011

1.12.2.1 Hourly Cloud Coverage

The full year of hourly cloud coverage reports with the days of the year on the horizontal and the hours of the day on the vertical. The sky cover is color coded: from most blue to most gray, the categories are clear, mostly clear, partly cloudy, mostly cloudy, and overcast. Pink indicates missing data.
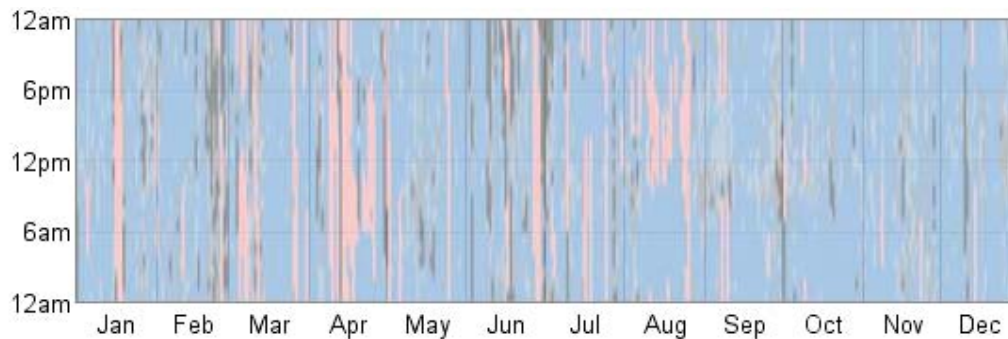
Fig. 1.14 Hourly Cloud Coverage

1.12.3 Precipitation

This station reports the quantity of liquid precipitation but not observations of weather events in the area. For this reason, this section will only discuss the quantity of precipitation and not its type.
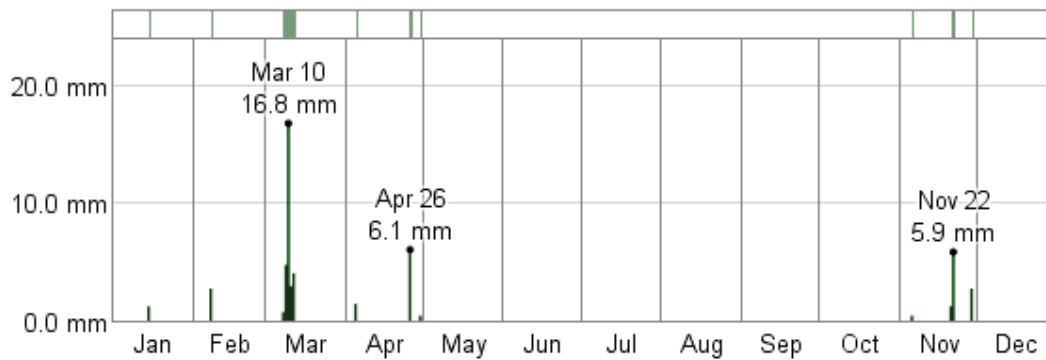

Fig. 1.15 Precipitation amount during 2011

1.12.4 Humidity

Humidity is an important factor in determining how weather conditions feel to a person experiencing them. Hot and humid days feel even hotter than hot and dry days because the high level of water content in humid air discourages the evaporation of sweat from a person's skin.

When reading Fig. 1.16, keep in mind that the hottest part of the day tends to be the least humid, so the daily low (brown) traces are more relevant for understanding daytime comfort than the daily high (blue) traces, which typically occur during the night. Applying that observation, the least humid month of 2011 was June with an

average daily low humidity of 6%, and the most humid month was January with an average daily low humidity of 37%.

But it is important to keep in mind that humidity does not tell the whole picture and the dew point is often a better measure of how comfortable a person will find a given set of weather conditions. Please see the next section for continued discussion of this point.
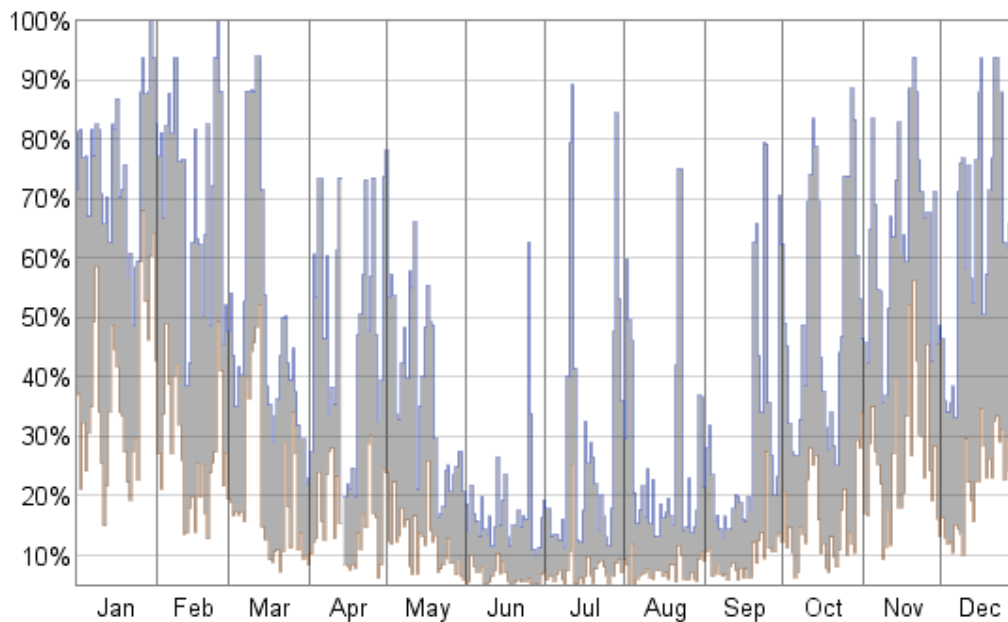
Fig. 1.16 Humidity Variation for year 2011

The daily low (brown) and high (blue) relative humidity during 2011 with the area between them shaded gray and superimposed over the corresponding averages (thick lines), and with percentile bands (inner band from 25th to 75th percentile, outer band from 10th to 90th percentile).

1.12.5 Dew Point

Dew point is the temperature below which water vapor will condense into liquid water. It is therefore also related to the rate of evaporation of liquid water. Since the

evaporation of sweat is an important cooling mechanism for the human body, the dew point is an important measurement for understanding how dry, comfortable, or humid a given set of weather conditions will feel.

Generally speaking, dew points below 10°C will feel a bit dry to some people, but comfortable to people accustomed to dry conditions; dew points from 10°C to 20°C are fairly comfortable to most people, and dew points above 20°C are increasingly uncomfortable, becoming oppressive around 25°C.

To take some examples from Fig. 1.17, and basing our categorization on the daily high dew point in 2011, January had 19 dry days, 12 comfortable days, and no humid days; April had 11 dry days, 18 comfortable days, and no humid days; July had 15 dry days, 10 comfortable days, and 6 humid days; and October had 8 dry days, 14 comfortable days, and 9 humid days.

Fig. 1.17 Dew Point Variation during 2011

The daily low (blue) and high (red) dew point during 2011 with the area between them shaded gray and superimposed over the corresponding averages (thick lines), and with percentile bands (inner band from 25th to 75th percentile, outer band from 10th to 90th percentile).
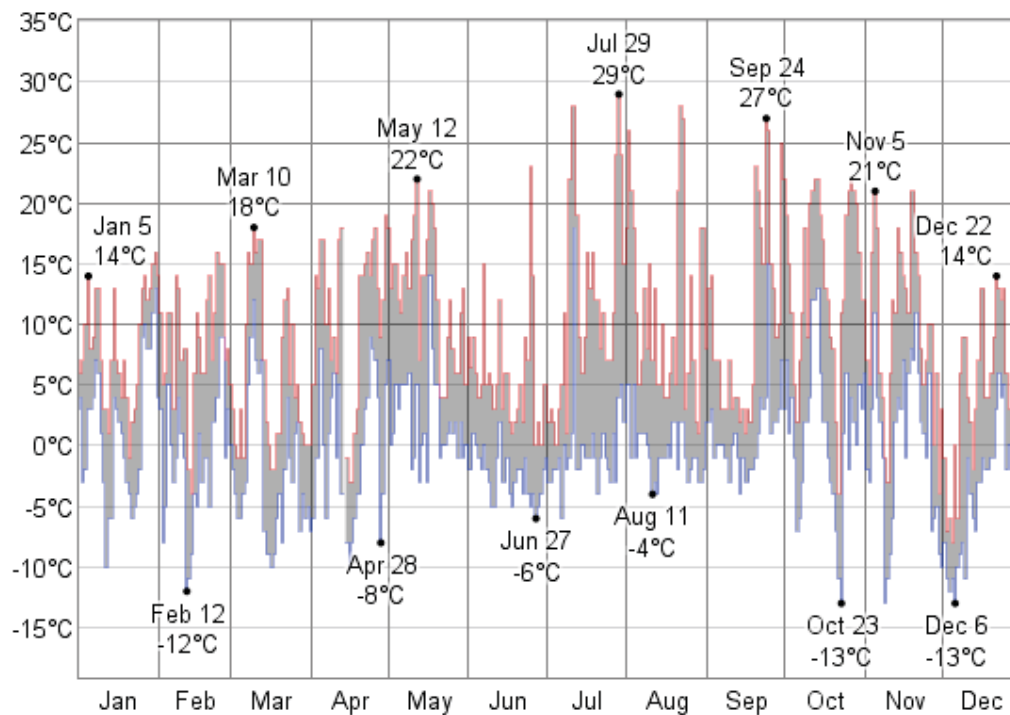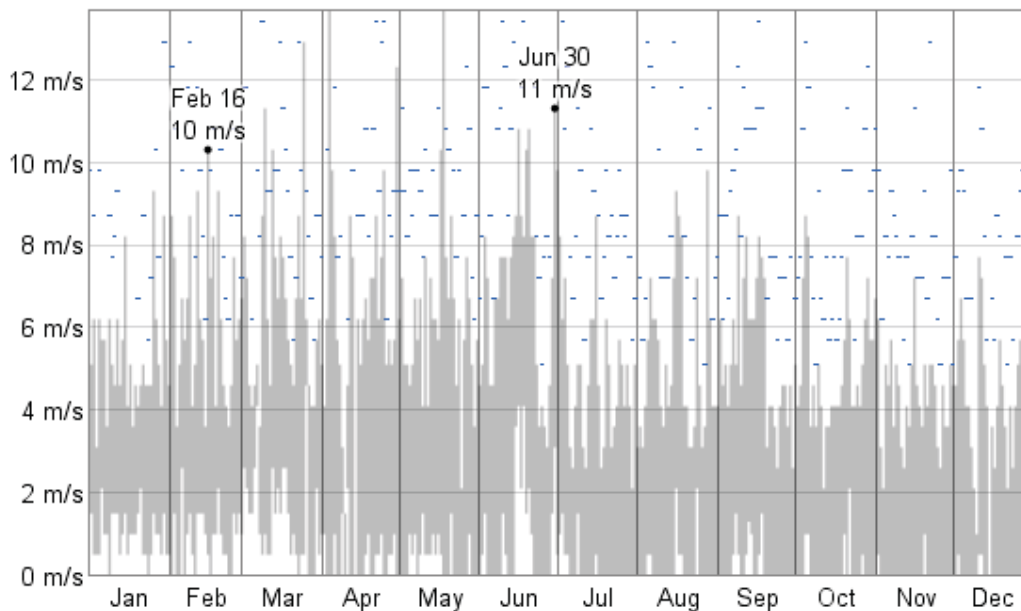
1.12.6 Wind

The highest sustained wind speed was 16 m/s, occurring on April 4; the highest daily mean wind speed was 7 m/s (June 16); and the highest wind gust speed was 21 m/s (April 4). As indicated in Fig. 1.18, the windiest month was March, with an average wind speed of 4 m/s. The least windy month was December, with an average wind speed of 2 m/s.

Fig. 1.18 Wind Speed Variation

The daily low and high wind speed (light gray area) and the maximum daily wind gust

speed (tiny blue dashes).
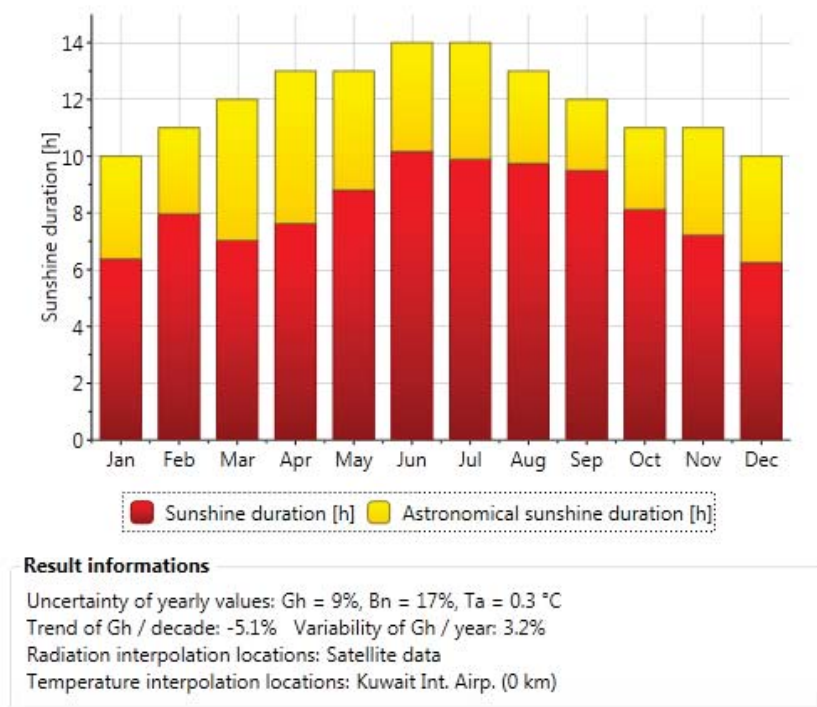
Fig. 1.19 Sunshine Duration
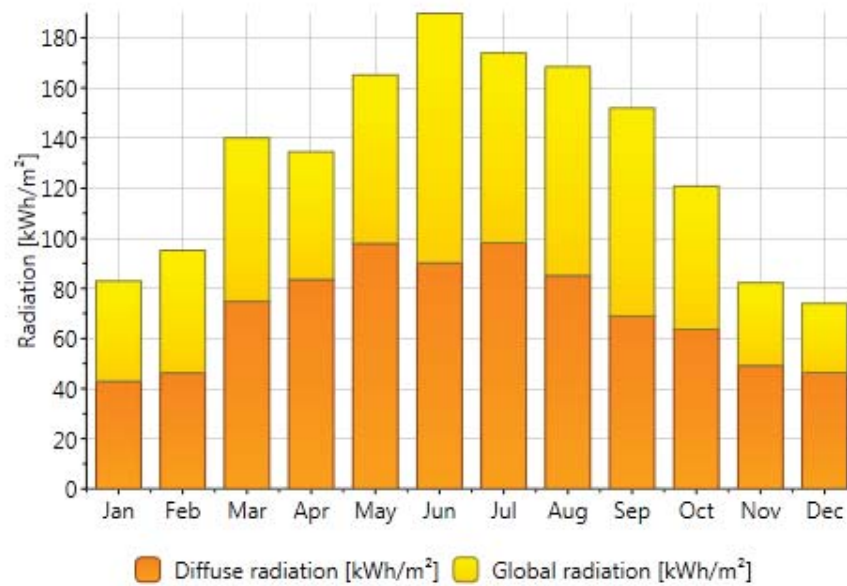
Fig. 1.20 Diffuse Radiation

1.12.7 Measurement of meteorological data

The site of the measurement station was located at Kuwait International Airport (29.217_Latitude N, 47.983_Longitude E). The meteorological data were collected stored to calculate the mean, maximum and minimum hourly values of these data. From the hourly data set, daily and monthly statistics were made for the stored meteorological data. As an example, Figs. 1.19 and 1.20 display the monthly sunshine duration and solar radiation.

1.12.8 Global Solar Radiation

From the recorded meteorological data it is clear that the daily average and maximum global radiation as well as temperatures are higher in summer time and lower in the winter. Fig. 1.21 describes the daily average global solar radiation for the whole period of 2007-2011. The graph shows that the daily highest global radiation of 2650 W/m2 was recorded in July, while the lowest daily average solar radiation of 930 W/ m2 was recorded in February. Fig. 1.21 also shows downward excursions in winter, especially in January and February. These excursions might be due to sandstorms, rain events and higher air mass in winter. The higher air mass in winter somewhat reduces the clear sky data by the absorption along the longer path length. The measurements agreed with the 22-year average global solar radiation data of the NASA SSE model [1.6].
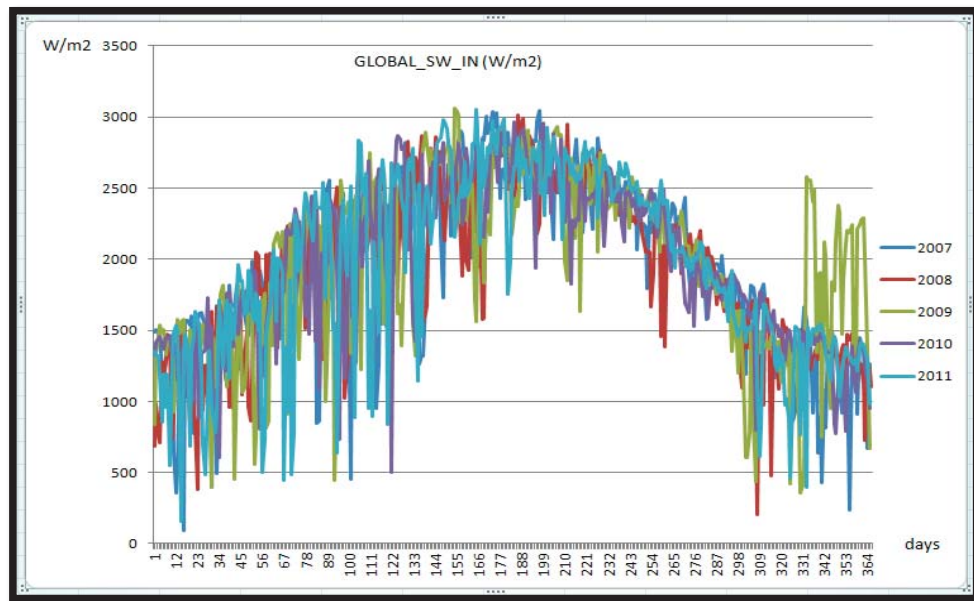
Fig. 1.21 Daily Variation of Global solar radiation from 2007-2011

1.12.9 Wind Energy conversion

The feasibility of wind energy conversion is under investigation by the Kuwaiti Institute for Scientific Research (KISR). The main objective of this study is to develop sustainable building with integrated renewable energy systems, in particular wind power. Fig. 1.22 shows a sketch of how the power output from a wind turbine varies with steady wind speed.

Typical wind turbine power output with steady wind speed.
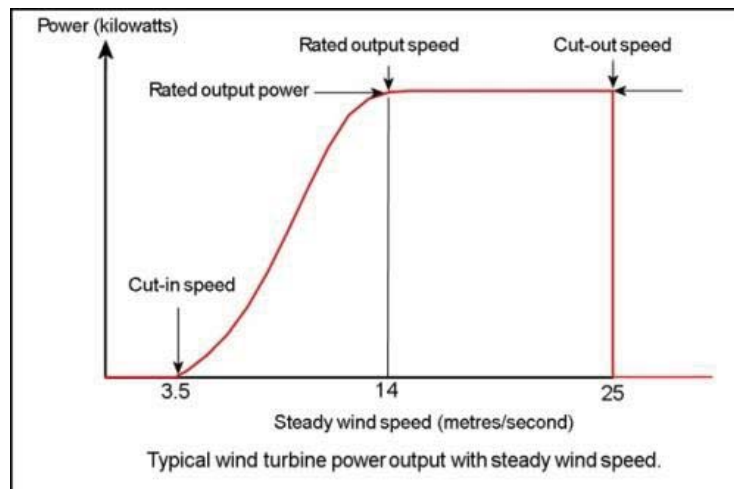
Fig. 1.22 Wind Turbin Characterstics

1. Cut-in speed

At very low wind speeds, there is insufficient torque exerted by the wind on the turbine blades to make them rotate. However, as the speed increases, the wind turbine will begin to rotate and generate electrical power. The speed at which the turbine first starts to rotate and generate power is called the cut-in speed and is typically between 3 and 4 meters per second.

2. Rated output power and rate output wind speed

As the wind speed rises above the cut-in speed, the level of electrical output power rises rapidly as shown. However, typically somewhere between 12 and 17 metres per second, the power output reaches the capacity limit of the electrical generator. This limit to the generator output is called the rated power output and the wind speed at which it is reached is called the rated output wind speed. At higher wind speeds, the design of the turbine is arranged to limit the power to this maximum level and there is no further rise in the output power. How this is done varies from design to design but typically with large turbines, it is done by adjusting the blade angles so as to keep the power at the constant level.

3. Cut-out speed

As the speed increases above the rate output wind speed, the forces on the turbine structure continue to rise and, at some point, there is a risk of damage to the rotor. As a result, a braking system is employed to bring the rotor to a standstill. This is called the cut-out speed and is usually around 25 metres per second.

By comparing the recorded wind speed with the wind power curve results in a significant number of days per year when wind speed is less than 4 m/s and hence the wind power would drop to zero. Therefore, the potential of utilizing wind energy is generally lower than that of solar energy. This creates a serious problem in planning a nation's electricity supply system. In Kuwait, the government target is to increase the share have of electricity supply by provided by renewable sources - which will

effectively all be provided by solar energy. In the following sections characteristics of

Photovoltaic cells are studied under the climate conditions of Kuwait.

References

[1.1]   Statistical Year Book 2010 - Electrical Energy - Ministry of Electricity & Water

[1.2]   Ali Hajiah," Sustainable Enrgy in Kuwait: Challenges and opportunities", UNDP Regional Meeting, 6 Oct. 2010.

[1.3]   F. Q. Al-Enezi and J. K. Sykulski, Modeling of a Photovoltaic Module Considering the Solar Energy Available from Horizontal Surfaces over Kuwait Area, JOURNAL OF ELECTRONIC SCIENCE AND TECHNOLOGY, VOL. 10, NO. 2, JUNE 2012

[1.4]   Renewable Energy Applications and Potentials in MENA Region, National Links with EU or Other Organizations: UNDP

[1.5]   Kasten, F., and Czeplak, G., 1980, "Solar and Terrestrial Radiation Dependent on the Amount and Type of Cloud," Sol. Energy **24_2_**, pp. 177–189.

[1.6]   NASA SSE Model, 1983−2005, Atmospheric Science Data Center.

[1.7]   Dr. Volker Quaschning, Dr. Manuel Blanco Murie, Photovoltaics or Solar Thermal Power Plants?, DLR, Plataforma Solar de Almería, Spain, CIEMAT, Plataforma Solar de Almería, Spain, VGB Congress Power Plants 2001 • Brussels • October 10 to 12, 2001, the contents available at : http://volker-quaschning.de/downloads/VGB2001.pdf.

[1.8]   M.Eltawil and D.Samuel "Vapour Compression Cooling System Powered By Solar PV Array for Potato Storage" Agricultural Engineering International: the CIGR Ejournal. Manuscript EE 06-003. Vol. IX. June, 2007

[1.9]   Al-Salaymeh, Al-Hamamre, Sharaf, Abdelkader, a Technical and economical assessment of the utilization of photovoltaic systems in residential buildings: The case of Jordan, December 2009, contents lists available at Science Direct Website, www.sciencedirect.com.

[1.10] Hining ,H.-M(Ed): Solar-Assisted Air – Conditioning in Building –A Handbook for planners. Springer-Verlag/wien, 2004.

[1.11] Nada Mekki, Application of absorption solar air-conditioning Technology depending on climate and building standard, Energy and semiconductor Research Laboratory, Department of physics, Faculty of Mathematics &Science ,Carl Von Ossietzky University, Oldenburg/F.R. Germany, 2008.

[1.12] Mohamed Sebzali, Assessment of Cool Thermal Storage Strategies in Kuwait, Ph.D Theses, Cranfield University, 2007.

[1.13] Grell et al. 1995, A Description of the Fifth-Generation Penn State/NCAR.

[1.14] R. Perez, S. Wilcox, D. Renne, K. Moore, A. Zelenk, " Forecasting Solar Radiation: Preliminary Evaluation of an Approach based upon the National Forecast Data Base", Solar Energy, Vol. 81, Issue 6, June 2007, pp. 809-812.

[1.15] M. De Pondeca, X. Zou, " A Case Study of Variation Assimilation of GPS Zenith Delay Observation into a Mesoscale Model", J. Appl. Meteoro., Vol. 40, 2001, pp. 1559-1576.

[1.16] X. Zou, Q. Xiao, A. Lipton, Q. Modica, " A Numerical Study of the Effect of GOES Sounder Cloud-Cleared Brightness Temperature on the Prediction of Hurricane Felix", J. Appl. Meteoro., Vol. 40, 2001, pp. 34-35.

[1.17] Y. Lui, D.-L. Zhang, M. Yau, " A Multi-Scale Numerical Study of Hurricane Andrew 1992- Part II: Kinematics of Inner-Core Structure", Mon. Weather Rev., Vol. 127, 1999, pp 2597-2616.

Chapter 2

Design and Modeling of Photovoltaic Systems

2.1 Definition

A photovoltaic system consists generally of one or more solar panels to convert solar energy into electricity. It consists of multiple components, including the photovoltaic modules, mechanical and electrical connections and mountings as well as electronic devices to regulate and/or modify the electrical output [2.1].

2.2 Photovoltaic Arrangements

2.2.1 Photovoltaic Cell

PV cells are made of semiconductor materials, such as silicon. For solar cells, a thin semiconductor wafer is specially treated to form an electric field, positive on one side and negative on the other. When light energy strikes the solar cell, electrons are knocked loose from the atoms in the semiconductor material. If electrical conductors are attached to the positive and negative sides, forming an electrical circuit, the electrons can be captured in the form of an electric current and generate electric power. This electric power can then be used to power a load [2.1]. A PV cell can either be circular or square in construction.

2.2.2 Photovoltaic Module

Due to the low voltage generated in a PV cell (around 0.5V), several PV cells are connected in series (for high voltage) and in parallel (for high current) to form a PV module for the desired output. Separate diodes may be needed to avoid reverse currents,

in case of partial or total shading, and at night. The p-n junctions of mono-crystalline silicon cells may have adequate reverse current characteristics and these are not necessary. Reverse currents can cause power loss and also lead to overheating of shaded cells. Solar cells become less efficient at higher temperatures and in extreme cases ventilation is required for solar panels [2.2].

2.2.3 Photovoltaic Array

The power that one module can produce is not sufficient to meet the requirements of home or business. Most PV arrays use an inverter to convert the DC power into alternating current that can supply loads such as motors, lights etc. The modules in a PV array are usually first connected in series to obtain the desired voltages; the individual modules are then connected in parallel to allow the system to produce more current [2.2]. The different PV system configurations are displayed in Fig. 2.1.
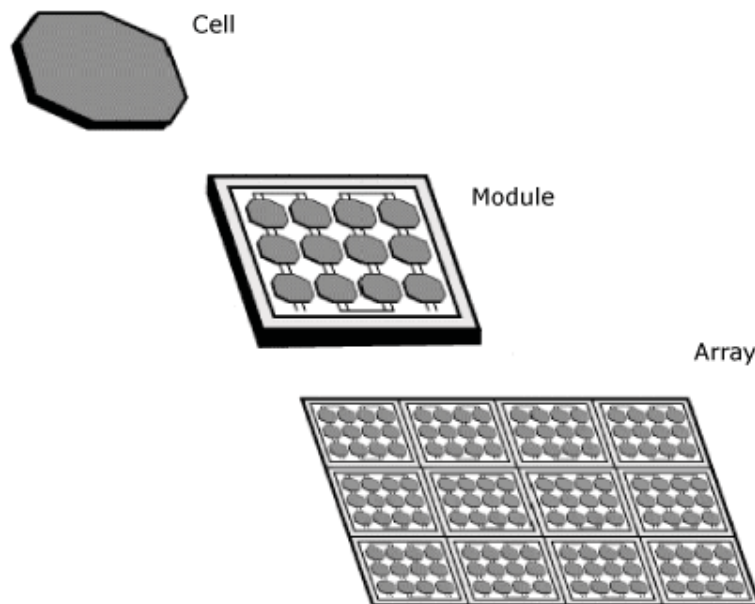
Fig. 2.1 Photovoltaic systems

66

2.3 Materials Used in PV Cells

The materials used in PV cells are classified as follows:

2.3.1 Single-Crystal Silicon

Single-crystal silicon cells are the most common in the PV industry. The main technique for producing single-crystal silicon is the Czochralski (CZ) method. High-purity polycrystalline is melted in a quartz crucible. A single-crystal silicon seed is dipped into this molten mass of polycrystalline. As the seed is pulled slowly from the melt, a single-crystal ingot is formed. The ingots are then sawed into thin wafers about 200-400 micrometers thick. The thin wafers are then polished, doped, coated, interconnected and assembled into modules and arrays [2.2].

2.3.2 Polycrystalline Silicon

Consisting of small grains of single-crystal silicon, polycrystalline PV cells are less energy efficient than single-crystalline silicon PV cells. The grain boundaries in polycrystalline silicon hinder the flow of electrons and reduce the power output of the cell. A common approach to produce polycrystalline silicon PV cells is to slice thin wafers from blocks of cast polycrystalline silicon. Another more advanced approach is the "ribbon growth" method in which silicon is grown directly as thin ribbons or sheets with the approach thickness for making PV cells [2.2].

2.3.3 Gallium Arsenide (GaAs)

A compound semiconductor made of two elements: Gallium (Ga) and Arsenic (As). GaAs has a crystal structure similar to that of silicon. An advantage of GaAs is that it

has high level of light absorptivity. To absorb the same amount of sunlight, GaAs requires only a layer of few micrometers thick while crystalline silicon requires a wafer of about 200-300 micrometers thick. Also, GaAs has much higher energy conversion efficiency than crystal silicon, reaching about 25 to 30%.The only drawback of GaAs PV cells is the high cost of single crystal substrate that GaAs is grown on [2.2].

2.3.4 Cadmium Telluride (CdTe)

It is a polycrystalline compound made of cadmium and telluride with a high light absorbility capacity (i.e a small thin layer of the compound can absorb 90% of solar irradiation).The main disadvantage of this compound is that the instability of PV cell or module performance. As it a toxic substance, the manufacturing process should be done by extra precaution [2.1, 2.2].

2.3.5 Copper Indium Diselenide (CuInSe$_2$)

It is a polycrystalline compound semiconductor made of copper, indium and selenium. It delivers high energy conversion efficiency without suffering from outdoor degradation problem. It is one of the most light-absorbent semiconductors. As it is a complex material and toxic in nature so the manufacturing process face some problem [2.2].

2.4 Characteristics of PV Cell

A photovoltaic cell is simply represented by a forward biased diode of large area with a photo-voltage. The photo-voltage is created from the dissociation of electron hole pairs created by incident photons within built-in field of the junction [2.3, 2.4]. In the dark, the solar cell is not an active device; it works as a diode (p-n junction). However, if it is

connected to an external supply (large voltage) it generates a current I_D, called the diode current or dark current. Fig. 2.2 illustrates the I-V characteristic of the solar cell for a fixed ambient irradiation G and a given cell temperature T_c.

If the cell's terminals are connected to a variable resistance R, the operating point is determined by the intersection of the I-V curve of the solar cell with the load I-V curve. For a resistive load, the load characteristic is a straight line with a slope I/V=1/R. Note that the power delivered to the load depends on the value of the resistance only. However, if the load R is small, the cell operates in region MN of the curve, where the cell behaves as a constant current source, almost equal to the short circuit current. On the other hand, if the load R is large, the cell operates on the region PS of the curve, where the cell behaves more as a constant voltage source, almost equal to the open circuit voltage.
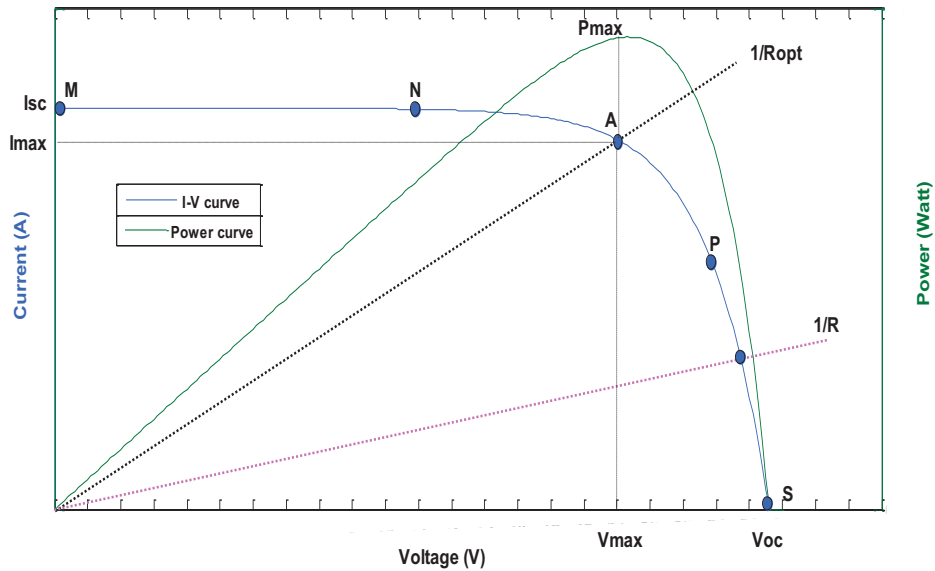
Fig. 2.2 Characteristic of a PV cell

A solar cell can be characterized by the following fundamental parameters as indicated in Fig. 2.2.

Short Circuit Current I_{sc}

It is the greatest value of the current generated by a cell. It is produced under short circuit conditions ($V=0$). The short circuit current can be considered equivalent to the photocurrent ($I_{sc} = I_{ph}$).

Open Circuit Voltage V_{oc}

This corresponds to the voltage drop across the diode (p-n junction), when it is traversed by the photocurrent I_{ph} ($I_D = I_{ph}$), when the generated current is $I = 0$. It reflects the voltage of the cell at night and can be expressed as:

$$V_{oc} = \frac{BKT_c}{q} \ln\left(\frac{I_{ph}}{I_o}\right)$$

(0.6)

where, B is the ideality factor, K is Boltzmann's constant, T_c is the absolute temperature of the cell, q is the electronic charge and I_{ph} is the photocurrent. I_o is the dark saturation current and it is strongly dependent on temperature [2.1, 2.2].

Maximum Power Point P_{max}

It is the operating point A (V_{max}, I_{max}) in Fig. 2.2, at which the power dissipated in the resistive load is maximum:

$$P_{max} = I_{max} \times V_{max}$$

(0.7)

Maximum Efficiency η

It is the ratio between the maximum power and the incident light power:

$$\eta = \frac{P_{max}}{P_{in}} = \frac{I_{max} \times V_{max}}{A_c \times G} \qquad (0.8)$$

where, G is the ambient radiation and A_c is the cell area.

Fill Factor *FF*

It is the ratio of the maximum power that can be delivered to the load and the product of I_{sc} and V_{oc}:

$$FF = \frac{P_{max}}{V_{oc} \times I_{sc}} = \frac{I_{max} \times V_{max}}{V_{oc} \times I_{sc}} \qquad (0.9)$$

The fill factor is a measure of the real I-V characteristic. Its value is higher than 0.7 for good cells. The fill factor diminishes as the cell temperature is increased.

2.4.1 PV Module

Cells are normally grouped into modules in order to meet specified power output requirements as previously shown in Fig. 2.1. The cells are encapsulated with various materials to protect them and the electrical connectors from the environment. Fig. 2.3 represents how I-V characteristics are modified in the case when two identical cells are connected in series or in parallel [2.2].

(a)   (b)
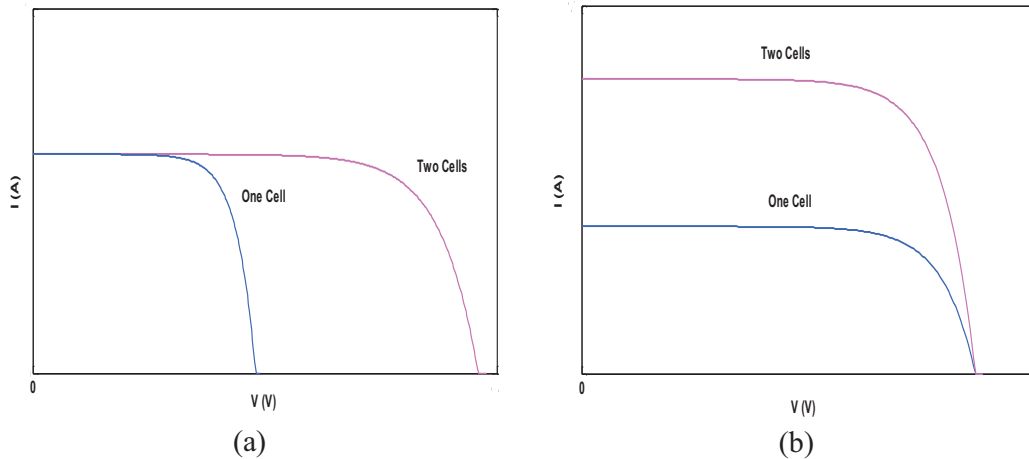
Fig. 2.3 I-V characteristics of two identical PV cells. (a) In series. (b) In parallel.
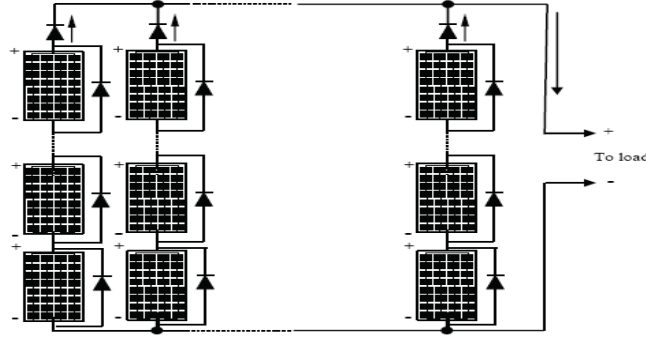
Fig. 2.4 PV array

2.4.2 PV Array

The modules in a PV system are typically connected in arrays. Fig. 2.4 illustrates the array configuration with M_p parallel branches each with M_s modules in series. If it is assumed that the modules are identical and the ambient irradiation is the same on all the modules then, the array's terminal voltage can be determined by:

$$V_A = M_S \times V_M \tag{0.10}$$

and the array's current is:

$$I_A = M_P \times I_M \tag{0.11}$$

2.4.3 Effect of irradiance and temperature on the module characteristics

The photocurrent I_{ph} is proportional to solar irradiance. The open circuit voltage increases slightly with increasing irradiance, while the short circuit current and the optimal power increase linearly with irradiation increase. Temperature has a significant effect on the solar cell I-V characteristics. The photocurrent will increase slightly with

increasing cell temperature. The open circuit voltage decreases linearly with increasing cell temperature owing to the exponential increase in saturation current [2.3, 2.4]. These effects will be discussed in details later in the report.

2.5 Types of PV Systems

There are two basically different PV systems: those with a connection to an (available) electric grid and remote or "stand-alone" systems. While in the first case the grid serves as an ideal storage component and ensures system reliability, the stand-alone systems require a storage battery. This battery serves as a buffer between the fluctuating power generated by the PV cells and the load. In order to ensure continuous power supply, even under extreme conditions, a back-up generator is often also installed. Building-integrated PV systems have an economical advantage over conventional PV generator systems: The PV modules serve for multiple purposes. They are part of the building envelope, ideally replacing conventional facade or roof material. Modem commercial building facades often cost as much as a PV façade which means immediate or short-term payback for the PV system. Depending on the type of integration, the PV modules may also provide shading or noise protection. Here again, the costs for replaced conventional means for these purposes may be deducted from the initial PV costs.

2.5.1 Stand-Alone Systems

PV systems are most effective at remote sites off the electrical grid. Their high reliability and low servicing requirements make them ideally suited for applications at (for parts of the year) unattended sites. The costs for a PV system compete in this case against the cost for a grid connection or other possible ways of remote energy supply.

As stated above, a storage battery is needed. Excess energy produced during times with no or low loads charges the battery, while at times with no or too low solar radiation the
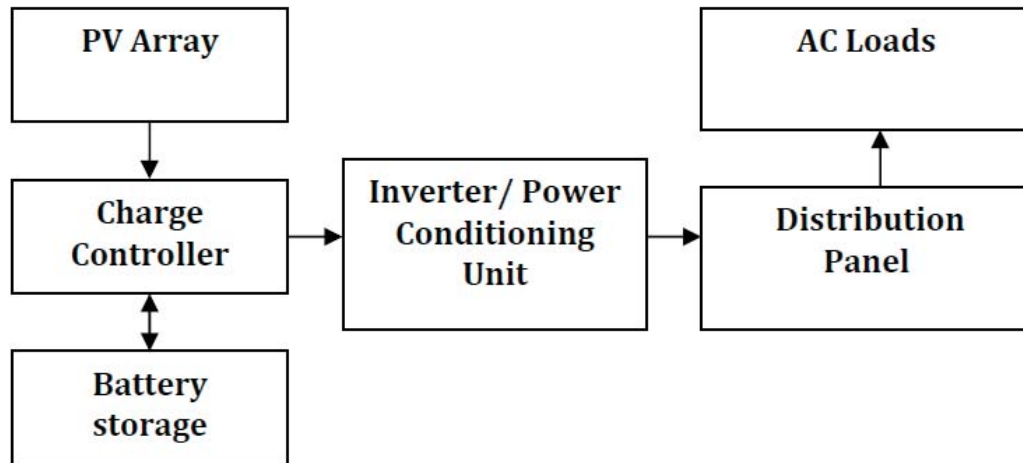
Fig. 2.5 Block diagram of a stand-alone PV system

loads are met by discharging it. A charge controller supervises the charge/discharge process in order to ensure a long battery lifetime. As in the grid-connected systems, an inverter, when required, transforms DC to AC electricity as given in Fig. 2.5 which represents the main components of stand alone PV system.

Due to the variable nature of the energy source (solar radiation), one of the most expensive aspects of a PV power system is the necessity to build in system autonomy. Autonomy is required to provide reliable power during "worst case" situations, which are usually periods of adverse weather, seasonally low radiation values or unpredicted increased demand for power. The addition of autonomy could be accomplished by over-sizing the PV array and greatly enlarging the battery storage bank - generally the two most costly system components. Substantial operating cost savings (compared to a generator-set system without PV) are achieved through the greatly reduced need for

generator-set operation. An additional benefit of this approach is the added system reliability provided by the incorporation of the back-up energy source.

Hybrid systems may contain more than one renewable power source. Adding a wind turbine to a PV generator-set system is a common combination in areas with -high wind energy potential [2.5].

2.5.2 Grid Connected PV Systems

A grid-connected photovoltaic system is an electrical power generating system that uses a photovoltaic (PV) array as the primary source of electricity generation. It is intended to operate synchronously and in parallel with the electric utility network. As shown in Fig. 2.6, such systems may also include battery storage, other generating sources, and may operate on site loads independent of the utility network during outages [2.6].

Photovoltaic power systems have made a successful transition from stand-alone to large grid-connected systems where the photovoltaic modules are connected to the grid. There are a two ways in which the modules can be integrated into the grid: connected photovoltaic arrays on the residential, commercial sites (i.e. on rooftops) or, large arrays of photovoltaic modules that act as generating stations.
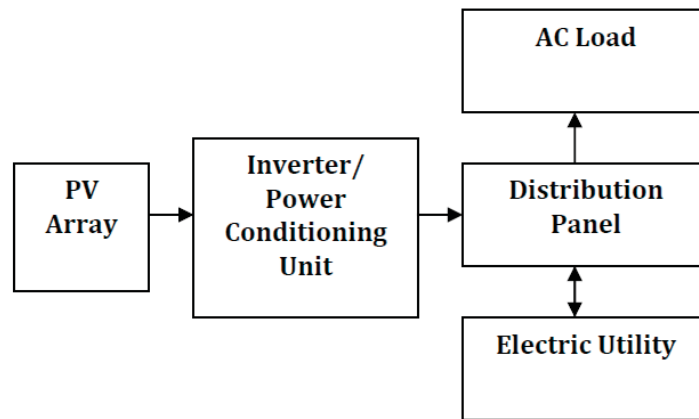
Fig. 2.6 Block diagram of a grid-connected PV system

Grid connected photovoltaic systems can vary in size but have common components including: PV arrays, an inverter to convert the DC power to AC power, a controller (i.e. protect the PV arrays from any voltage and frequency deviations), metering equipment to monitor the power that is feed into the grid and vice versa, MPPT (Maximum Power Point Tracker), module and other structures for mounting. Arrays from residential and commercials can sell their excess power to the grid during the day when more power than needed is obtained. When these sites need more power, (i.e. at night) they can buy it from the grid. Thus, the grid acts as storage means for the PV arrays during the day. Sometimes these PV arrays also have batteries and can choose whether to store the excess power in the batteries or sell it to the grid.

In recent years, technological advances and price reductions have resulted in numerous applications and increasing markets for grid-connected PV systems on residential and commercial buildings. The primary component in grid-connected PV systems is the inverter, or power-conditioning unit (PCU). The PCU converts the DC power produced by the PV array into AC power consistent with the voltage and power quality requirements of the utility grid. A bi-directional interface is made between the PV

system AC output circuits and the electric utility network, typically at an onsite distribution panel or service entrance. This allows the AC power produced by the PV system to either supply on-site electrical loads, or to back feed the grid when the PV system output is greater than the on-site load demand. At night and during other periods when the electrical loads are greater than the PV system output, the balance of power required by the loads is received from the electric utility. When the utility grid is down, these systems automatically shut down and disconnect from the grid. This safety feature is required in all grid-connected PV systems to ensure that the PV system will cease to operate and feed back into the utility grid when the grid is down for service or repair.

2.6 Modeling of PV Systems

Photovoltaic (PV) cells are basically transducers that directly convert solar energy into electrical energy. The physics behind such cells is similar to that of the basic p-n junction [2.3, 2.4]. It follows that an appropriate model of the PV cell should be able to predict its electrical characteristics under different irradiance and temperature levels. Most of the widely used models of PV cells follow the equivalent circuit approach where a PV cell is represented by an equivalent circuit that consists of one or two diodes [2.7-2.12]. A simple and popular model of the PV cell is the one representing it with an equivalent circuit consisting of a single diode [2.7]. In such a model, the ohmic losses can be taken into consideration by including a series resistance and/or a shunt resistance. When both the series and shunt resistances are considered, the model of the PV cell, which is shown in Fig. 2.7 (a), requires computation of five parameters in order to establish the current-voltage relationship that characterizes the cell [2.8]. The number of parameters becomes four when only the series resistance is taken into consideration [2.9]. The four parameters model is shown in Fig. 2.7 (b). An attractive feature of the

77

aforementioned models is that most of the calculations only rely on the data provided by the manufacturer. Another important feature is the fact that these models can be used in representing a single cell, a module of connected cells, or even an array of modules.

The single diode model is suitable for system-level designs. However, experiments requiring high accuracy at the expense of complication can use more complicated models such as the two diodes model [2.12]. In this model, an additional diode is placed

(a)   (b)
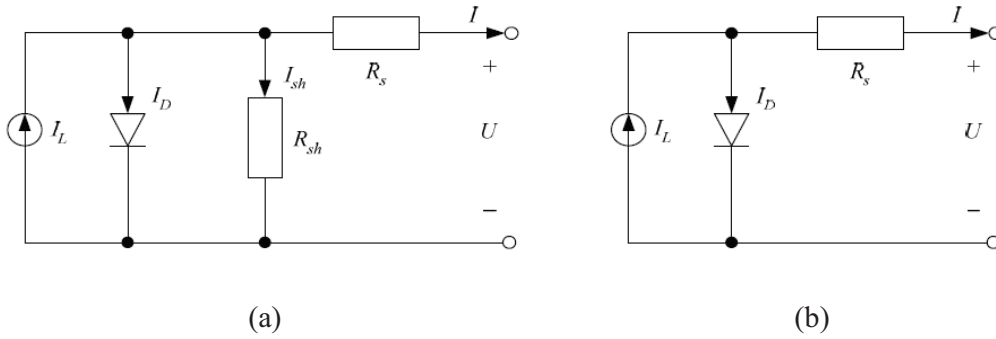
Fig. 2.7 The equivalent circuit in single diode PV models. (a) Five parameters model. (b) Four parameters model.

in parallel to that of the single diode model shown in Fig. 2.7 (a). To completely establish the current-voltage characteristics of the cell, eight parameters need to be calculated, hence the complication. A comprehensive review of the equivalent circuit models can be found in [2.13].

An important issue to consider when modeling a PV cell is the cell temperature. The cell temperature mainly depends on ambient and operating conditions. This dependency is accounted for using what is called the thermal models of the PV cell [2.8, 2.14]. A popular lumped thermal model has been proposed in [2.8] where the heat losses are all lumped together in one coefficient. This thermal model, in conjunction with the four parameters single diode model, is ideal for system level design. Detail thermal models have also been proposed in the literature as in [2.14].

In this section, a practical PV cell is modeled and simulated. First, the four parameter single diode PV model is discussed in section 2.6.1. A Simulink program based on this model is developed in section 2.6.2. In section 2.6.3, the developed program is used in the simulation of a practical PV cell and the results are shown to demonstrate its functionality.

2.6.1 The Four-Parameter Single-Diode Equivalent Circuit Model

The equivalent circuit of a PV module according to this model is shown in Fig. 2.7 (b). The model consists of a single diode, and the ohmic losses are represented by a series resistance. The expression governing the relationship between the load current and the output voltage in the single-diode model is as follows:

$$I = I_L - I_D = I_L - I_0 \left[\exp\left(\frac{U + I R_s}{\alpha} \right) - 1 \right] \qquad (0.12)$$

where I_L, I_D, I_0, and I are the light, dark, saturation and load currents, respectively, all measured in (A); U is the output voltage (V); R_s is the series resistance (Ω); and α is the thermal voltage timing completion factor (V). For the $I - U$ relationship to be completely defined, the quadruplet (I_L, I_0, R_s, α) needs to be determined. For this reason, the discussed single diode model is also called a four parameter model. The four parameters depend on I_L, temperature, and/or solar irradiance. This dependency will be discussed in what to follow.

First, the calculation of the parameter α is discussed. To calculate α, the parameter α_{ref} needs to be determined first as in [2.15]:

$$\alpha_{ref} = \frac{2U_{mp,ref} - U_{oc,ref}}{\dfrac{I_{sc,ref}}{I_{sc,ref} - I_{mp,ref}} - \ln\left(1 - \dfrac{I_{mp,ref}}{I_{sc,ref}}\right)} \tag{0.13}$$

where $U_{mp,ref}$ (V) and $I_{mp,ref}$ (A) are the maximum power point voltage and current, respectively, at the reference condition; $U_{oc,ref}$ (V) is the open circuit voltage of the module at the reference condition; and $I_{sc,ref}$ (A) is the short circuit current of the module at the reference condition. The values of $U_{mp,ref}$, $I_{mp,ref}$, $U_{oc,ref}$, and $I_{sc,ref}$ should be provided by the manufacturer at the reference condition which is associated with a specific reference irradiance level and a specific reference temperature. The parameter α depends on the temperature as follows:

$$\alpha = \frac{T_c + 273}{T_{c,ref} + 273}\alpha_{ref} \tag{0.14}$$

where T_c (°C) is the PV cell temperature, and $T_{c,ref}$ (°C) is the reference temperature which is usually taken to be 25 °C. After the calculation of α, the series resistance R_s can be easily found using the following expression [2.15]:

$$R_s = \frac{\alpha_{ref}\ \ln\left(1 - \dfrac{I_{mp,ref}}{I_{sc,ref}}\right) - U_{mp,ref} + U_{oc,ref}}{I_{mp,ref}} \tag{0.15}$$

However, the previous expression is an estimation of the value of R_s which in most cases is provided by the manufacturer. The two remaining parameters are the currents I_L and I_0. The saturation current I_0 is calculated using the following expression:

$$I_0 = I_{0,ref}\left(\frac{T_{c,ref} + 273}{T_c + 273}\right)^3 \exp\left[\frac{e_{gap}\ N_s}{q\ \alpha_{ref}}\left(1 - \frac{T_{c,ref} + 273}{T_c + 273}\right)\right] \tag{0.16}$$

where e_{gap} (J) is the band gap energy of the material which is 1.17 eV for silicon; N_s is the number of cells connected in series in the PV module; q (C) is the charge of an electron; and $I_{0,ref}$ (A) is the saturation current at the reference condition and can be calculated as follows [2.16]:

$$I_{0,ref} = I_{L,ref} \, \exp\left(-\frac{U_{oc,ref}}{\alpha_{ref}}\right)$$
(0.17)

where $I_{L,ref}$ (A) is the light current at the reference condition, and it can be obtained from the PV module data sheet supplied by the manufacturer. The last parameter to be calculated is I_L, and it can be found using:

$$I_L = \frac{\phi}{\phi_{ref}}\left[I_{L,ref} + \mu_{I,SC}\left(T_c - T_{c,ref}\right)\right]$$
(0.18)

where ϕ (W/m^2) is the irradiance; ϕ_{ref} (W/m^2) is the reference irradiance; and $\mu_{I,SC}$ (A/°C) is the temperature coefficient of the short-circuit current which is provided by the manufacturer.

2.6.1.1 Thermal Model of the PV Module

The cell temperature T_c used in the calculation of the four parameters of the PV model is not necessarily the temperature of the surrounding environment (ambient temperature). However, the two are related along with the output voltage and the load current in the thermal model the PV cell [2.16] which is given by the following differential equation:

$$C_{PV}\frac{dT_c}{dt} = k_{in,PV}\,\phi - \frac{U\cdot I}{A} - k_{loss}\left(T_c - T_a\right)$$
(0.19)

where C_{PV} [J/(°C.m^2)] is the overall heat capacity per unit area of the PV cell; $k_{in,PV}$ is the transmittance-absorption product of PV cells; k_{loss} [W/(°C.m^2)] is the overall heat loss coefficient; T_a (°C) is the ambient temperature; and A (m^2) is the effective area of the PV cell.

2.6.2 Simulink Implementation of the PV Model

In this section, a Simulink program is developed for the PV model based on (2.7)-(2.13). The block diagram for the Simulink implementation is shown in Fig. 2.8, whereas a detailed block diagram of the PV module is shown in Fig. 2.9. The program is conducted in two steps. The first step is to calculate the four parameters of the single diode model with the irradiance, cell temperature, and the manufacturer data as inputs. After these parameters are calculated, the program solves the $I - U$ relationship numerically using the algebraic constraint block as shown in Fig. 2.9.
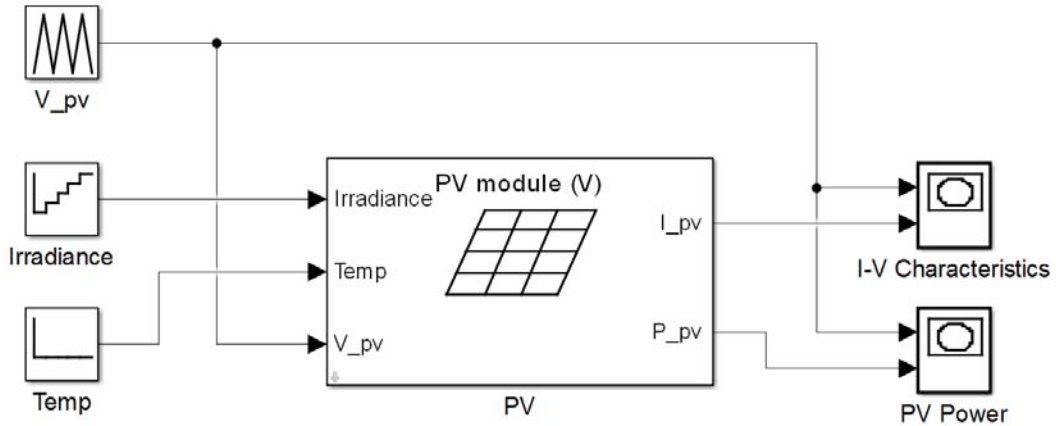

Fig. 2.8 Block diagram for the PV model implementation in Simulink.
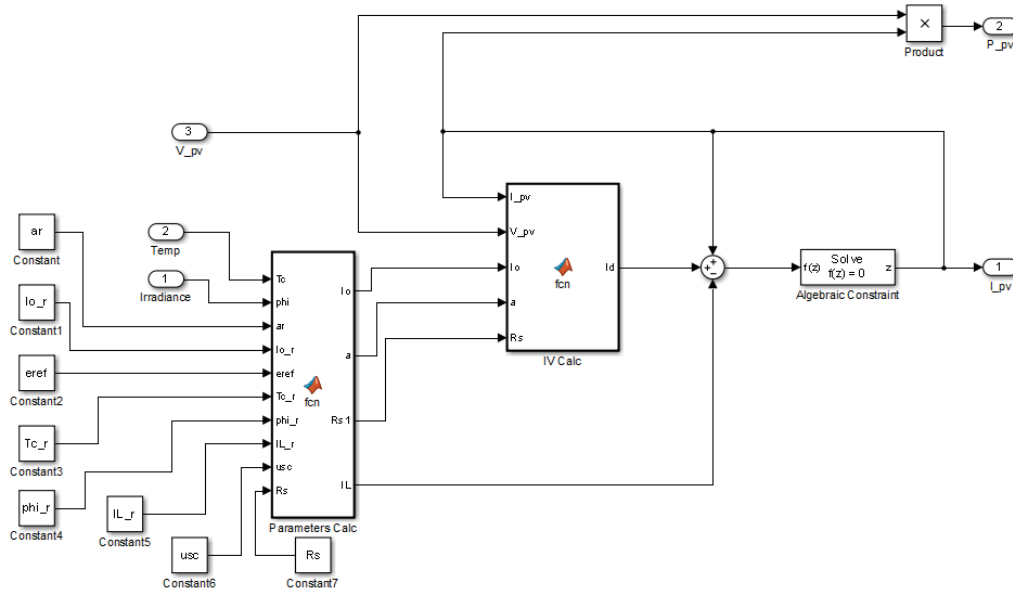
Fig. 2.9 Detailed Block diagram for the PV module of Fig. 2.8.

The manufacturer data are provided to the program by double-clicking the PV module block diagram in Fig. 2.8. The data entry window is shown in Fig. 2.10 (a). Before being processed by the program, simple initialization commands are carried out and are shown in Fig. 2.10 (b). In Fig. 2.9, two Matlab function blocks are present. The first called "Parameters Calc" is responsible for calculating the four parameters of the single diode model based on the manufacturer data, irradiance, and cell temperature. The code for this function is listed in Fig. 2.11 (a). The second function block called "IV Calc" is responsible for the calculation of the current I in (2.7) for a given voltage U and the knowledge of the model's four parameters. The code for the "IV Calc" function is listed in Fig. 2.11 (b).
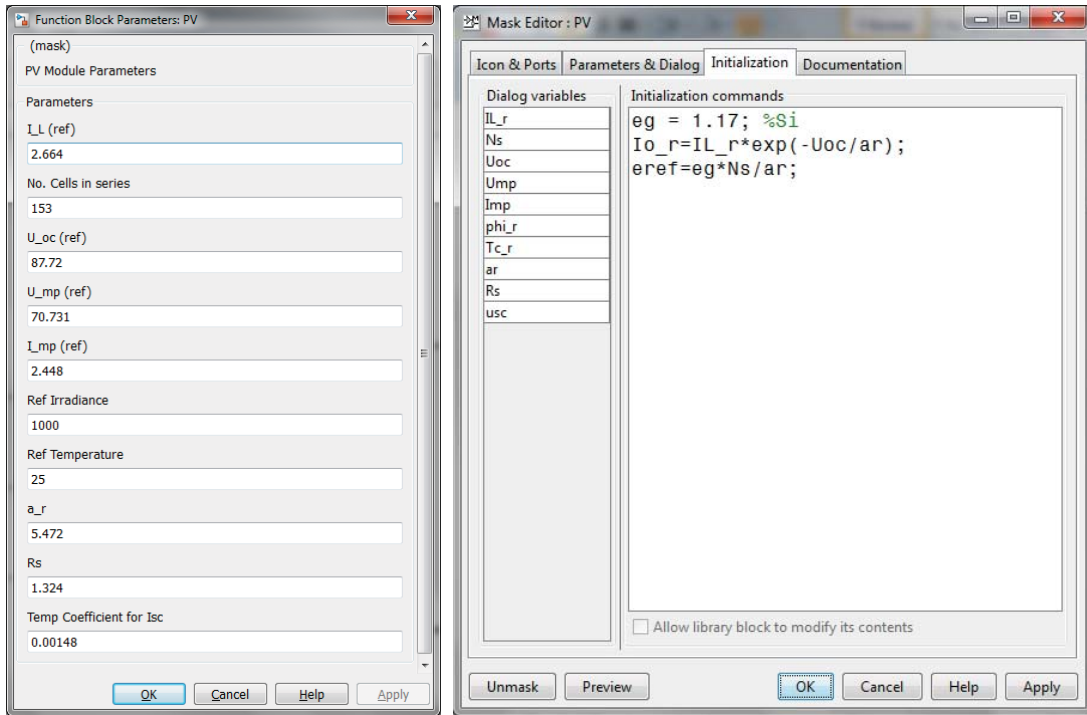
(a)   (b)

Fig. 2.10 Dialogs related to the manufacturer data. (a) Data entry. (b) Initialization code.

```
1 function [Io,a,Rs1,IL]  = fcn(Tc,phi,ar,Io_r,eref,Tc_r,phi_r,IL_r,↙
usc,Rs)
2 %#codegen
3 Io=Io_r*((Tc_r+273)/(Tc+273))^3*exp(eref*(1-((Tc_r+273)/(Tc+273))));
4 a =ar*(Tc+273)/(Tc_r+273);
5 IL = (phi/phi_r)*(IL_r+usc*(Tc-Tc_r));
6 Rs1=Rs;
7
```

(a)

```
1 function Id = fcn(I_pv,V_pv,Io,a,Rs)
2 %#codegen
3 Id = Io*(exp((V_pv+I_pv*Rs)/a)-1);
4
```

(b)

Fig. 2.11 Code listings for the function blocks used in the Simulink program. (a) Parameters Calc. (b) IV Calc.

2.6.3 Simulation of a PV module using the Simulink Program

The developed Simulink program will be used in this section to simulate the behavior of a PV module whose data are reported in [2.16]. The module consists of 150 cells that are connected in series. The data of this module are listed in Table 2.1. Two studies will be conducted on the PV module using the Simulink program. In the first study, the effect of the irradiance on the performance of the PV module is investigated. This is done by simulating the module under irradiance values between 200-1000 W/m^2 in 200 W/m^2 steps while maintaining the cell temperature at a constant level which is taken to be 25 °C in our case. The $I-U$ characteristic curves of the PV module for the different values of irradiance are shown in Fig. 2.12. It can be observed from the curves that the short circuit current I_{sc} and the open circuit voltage U_{oc} of the PV module increase with increasing irradiance levels. Accordingly, the maximum power of the module increases.

For the different irradiance levels, the relationship between the output voltage and the output power is shown in Fig. 2.13.

In the second study, the effect of the cell temperature on the performance of the PV module is investigated. This is done by simulating the module with the temperature values 0 °C, 25 °C, and 50 °C, while maintaining the irradiance at its reference level of 1000 W/m^2. The $I-U$ and $P-U$ characteristic curves of the simulated PV module for

Table 2.1 Parameters of the PV Module

Parameter	Value

α_{ref}	5.472 V
R_s	1.324 Ω
ϕ_{ref}	1000 W/m^2
$T_{c,ref}$	25 °C
$I_{L,ref} = I_{sc,ref}$	2.664 A
$U_{mp,ref}$	70.731 V
$U_{oc,ref}$	87.72 V
$I_{mp,ref}$	2.448 A
C_{PV}	5×10^4 J/(°C.m^2)
$k_{in,PV}$	0.9
k_{loss}	30 W/(°C.m^2)
A	1.5 m^2
$\mu_{I,SC}$	0.00148 A/°C

the different values of temperature are shown in Figs. 2.14 and 2.15, respectively. It can be observed that the maximum power and U_{oc} increase with decreasing temperature. However, decreasing the temperature leads to a slight decrease in I_{sc}.
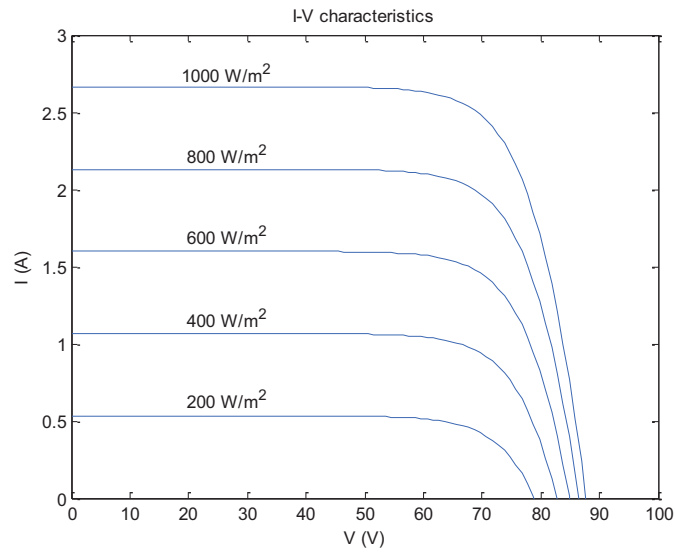
Fig. 2.12 $I-U$ **curves for different irradiance levels at** $T_c = T_{c,ref}$ **.**
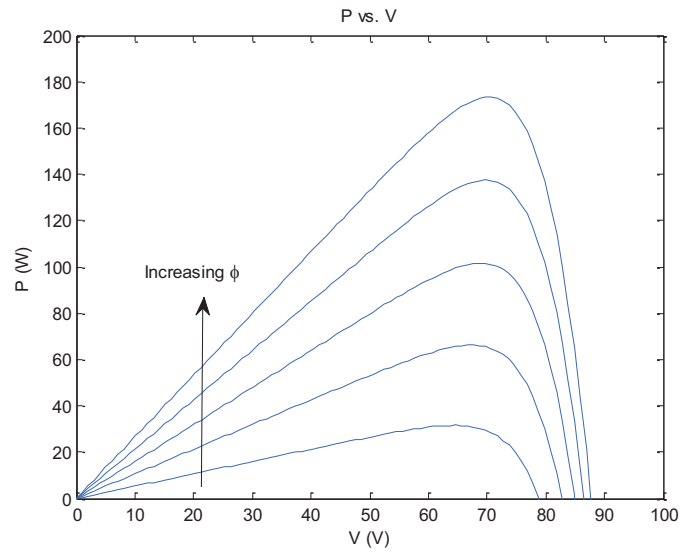
Fig. 2.13 $P-U$ **curves for different irradiance levels at** $T_c = T_{c,ref}$ **.**
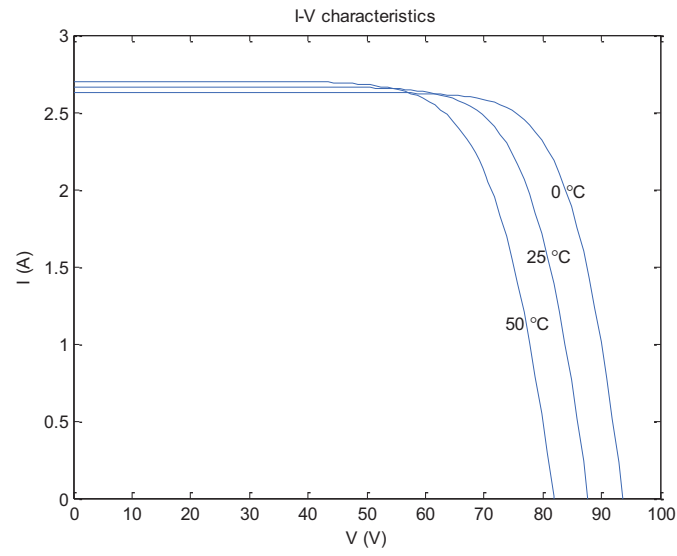
Fig. 2.14 $I - U$ **curves for different temperature values with** $\phi = \phi_{ref}$.

Fig. 2.15 $P - U$ **curves for different temperature values with** $\phi = \phi_{ref}$.

References

[2.1] Martin A. Green, Solar Cells Operating Principles, Technology and System Applications, Published by the University of New South Wales, 1992.

[2.2] D. Yogi Goswami, Frank Kreith and Jan F. Kreider, Principles of Solar Engineering, Taylor & Francis, USA, 2000.
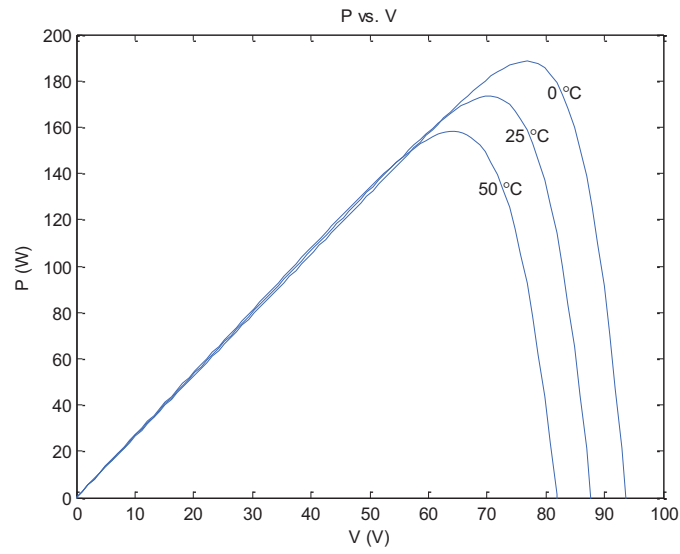
[2.3] M. R. Patel, Wind and Solar Power Systems, CRC Press LLC, 1999.

[2.4] R. Messenger and J. Ventre, Photovoltaic Systems Engineering, CRC Press LLC, 2000

[2.5] D. Hancen, H. Lars and H. Bindner, "Models for stand alone PV system", Riso National Laboratory, Roskilde, Norway, December 2000.

[2.6] Bouna Ould Zeidane, "Contribution to the Study Of Grid Connected Photovoltaic System", M.Sc, Université De Batna, 2003.

[2.7] Loferski J. J. (1972) An introduction to the physics of solar cells. In *Solar Cells— Outlook for Improved Efficiency*, pp. 47–53, National Academy of Sciences– Space Science Board, Washington, DC.

[2.8] Duffie, J.A., Beckman, W.A., 1991. Solar Engineering of Thermal Processes. John Wiley & Sons Inc, New York.

[2.9] Rauschenbach H. S. (1980) *Solar Cell Array Design Handbook: the Principles and Technology of Photovoltaic Energy Conversion*, Van Nostrand Reinhold, New York.

[2.10] Roger, J.A., Maguin, C., 1982. Photovoltaic solar panels simulation including dynamical thermal effects. Solar Energy, 29(3):245-256.

[2.11] Green, M. A. (1982). Solar cells: operating principles, technology, and system applications. *Englewood Cliffs, NJ, Prentice-Hall, Inc., 1982. 288 p.*, *1*.

[2.12] Gergaud B, Multon B, Ben Ahmed H (2002) Analysis and experimental validation of various photovoltaic system models. In: Proceedings of the 7th international ELECTRIMACS'2002 congress, Montréal

[2.13] Rekioua, D., and Matagne, E. (2012). Optimization of photovoltaic power systems. Springer.

[2.14] Mayer O. (1996). *DASTPVPS Simulation Tool Manual*, Universitat der Bundeswehr Munchen, Neubiberg, Germany.

[2.15] T.U. Townsend, A Method for Estimating the Long-Term Performance of Direct-Coupled Photovoltaic Systems, MS thesis, University Of Wisconsin – Madison, 1989.

[2.16] Øystein Ulleberg, Stand-Alone Power Systems for the Future: Optimal Design, Operation & Control of Solar-Hydrogen Energy Systems, Ph.D. Dissertation, Norwegian University of Science and Technology, Trondheim, 1998.

Chapter 3

Improvement of PV Panel Performance Using Switched Capacitor Converters

## 3.1 Improvement of Energy Extraction from Photovoltaic Panels with Multilevel Output DC-DC Switched Capacitor Converters

3.1.1 Introduction

The total installed cost ($/W) and total cost of ownership ($/Wh) have been well-studied as the key metrics controlling the grid penetration of solar power [3.1-3.4]. Among the factors impacting installed cost (per Watt) are power converter cost and total (tracking x conversion) efficiency, both of which share strong relations to converter and system complexity. A critical factor impacting the cost of ownership is the lifetime of the power converter (and implied replacement costs). Cost-effective solutions for solar energy extraction should address system cost and complexity, conversion and tracking efficiencies and converter lifetime simultaneously.

The need for suitable tracking efficiency is normally addressed with a maximum power point tracking (MPPT) algorithm embedded in the control of the converter or inverter [3.5, 3.6]. In the important grid-tied case, 100 Hz power ripple at the panel terminals negatively impacts the MPPT function, but this may be addressed by augmenting the source with a large electrolytic capacitor [3.7-3.15]. However, the limited lifetime of electrolytic capacitors contends directly with the long-life characteristic of cost-effective solar conversion. To reconcile this, [3.1] proposed the "ripple port" inverter, which still directly interfaces the PV cell, but directs the 100 Hz ripple power to a transformer coupled ripple port and away from the cell.

There is a growing need to implement per panel MPPT to contend with varying light levels, temperatures, panel ages, etc. across physically widespread solar arrays [3.7-3.15]. There are advantages of a DC-DC MIC + central DC-AC approach over a DC-AC MIC approach. These include the availability of a single DC bus for an entire array and intermediate power ripple filtering, as well as added degrees of freedom for MPPT control [3.7, 3.8, 3.16]. With per-panel MPPT, global tracking efficiency can be significantly improved over simple series or parallel connections of those panels (see Section 3.1.2.4), but the installation of per-panel converters impacts the important cost metrics above. Converter lifetime and replacement costs become even more critical with per panel conversion.

Many inductor based converters and inverters have been proposed as module integrated converter (MIC) topologies, but they require magnetic components to be either purchased per panel or to be integrated into the converter IC [3.7, 3.11]. Multilevel converters have been proposed as per panel DC-AC converters, but they suffer from either 120 Hz power ripple at the panel terminals or the need for cost-prohibitive and / or electrolytic energy storage [3.12-3.15].
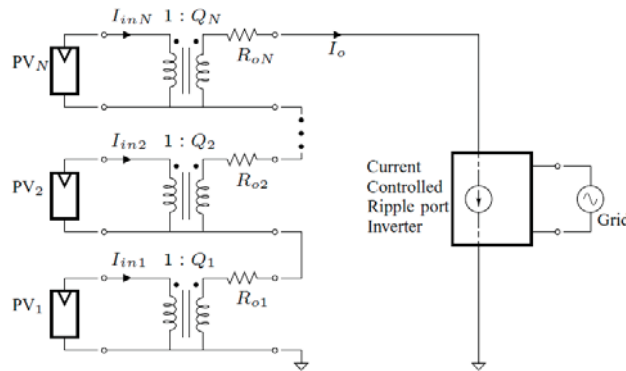

Fig. 3.1 A DC linearized model with an N-panel PV string illustrates the system-level approach. The ideal transformers model the function of the DC-DC MICs.

3.1.1.1 System Overview

The system level approach that we are pursuing for this joint project is illustrated by the DC linearized circuit model in Fig. 3.1. This system shares some key features with other systems employing DC-DC MICs and a central inverter but differs in at least one key way [3.7]. The DC-DC MICs typically operate with local autonomous MPPT control. In the system proposed here, the responsibility of MPPT is shared among the DC-DC modules and the central inverter. As a result, the required complexity of the DC-DC MICs is simplified. Significantly, the system can be implemented with switched capacitor multilevel DC-DC converters and a central ripple-port inverter. Per panel magnetics are eliminated as are electrolytic capacitors. Any magnetics that are required for the ripple port inverter need only be purchased once per string. The DC-DC module conversion ratios are selectable, but discrete. A central question that is addressed in this work concerns the tracking efficiency that is possible with this system.

3.1.1.2 Switched Capacitor Benefits

Switched capacitor converters achieve current and voltage conversion without magnetic energy storage. Fig. 3.2 shows the cost and volume per energy storage (J for a sample of discrete capacitors and inductors suitable for power applications. These data imply a-priori expected cost and volume benefits of switched capacitor converters when compared to inductor-based converters. A detailed discussion can be found in [3.17].
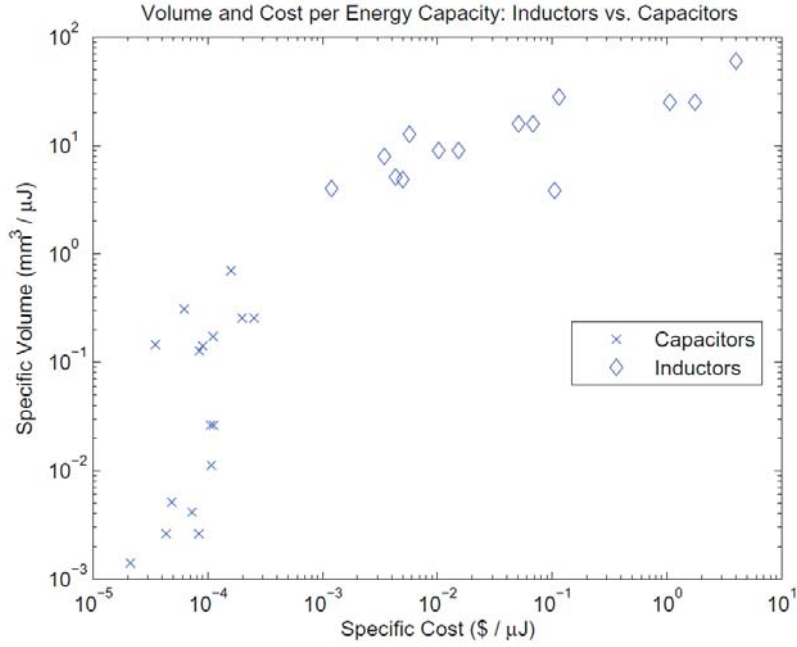
Fig. 3.2 Specific cost and volume: Discrete inductors (10 µH- 1 mH/100 mA-1 A) and capacitors (Ceramic and Film 1-10 µF/10-100 V) sampled from Digikey. Energy was calculated as 1/2 CV^2 or 1/2 LI^2 for maximum rated voltages and currents.

3.1.1.3 Total Efficiency

Total efficiency is central to the design and evaluation of the systems in this work. Here we define total efficiency, η, as the product of tracking efficiency, η$_p$, and conversion efficiency, η$_c$:

$$\eta = \eta_p \times \eta_c \tag{0.20}$$

Fig. 3.3 depicts a sample of reported tracking and conversion efficiencies in MPPT algorithms and DC-DC MICs respectively. The two ranges are multiplied yielding a third range corresponding to total efficiency η.
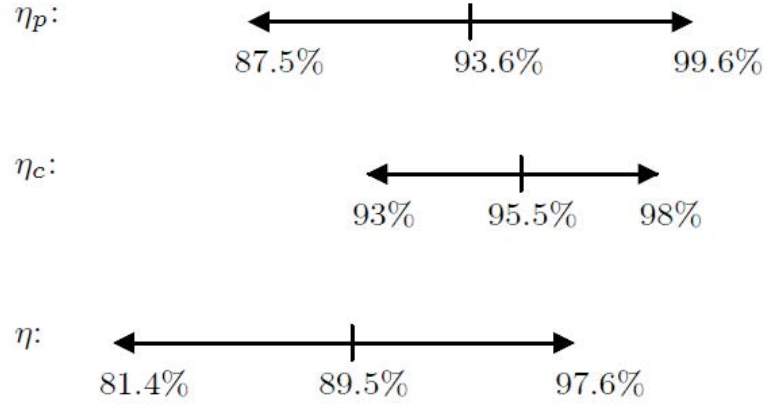
Fig. 3.3: A literature survey of total energy extraction efficiency, DC-DC MICs: [3.7, 3.8, 3.18–3.23] and MPPT algorithms: [3.6, 3.23–3.27]

3.1.2 Maximum Power Point Tracking

Maximum power point tracking in the system of Fig. 3.1 is simplified by the input current control of the central inverter and the series connection of the MICs. The selectable conversion ratios, Q_i, allow the DC-DC modules to track local MPP's as the string current varies. The central inverter tracks the global MPP by adjusting its input current.

The run-time global MPPT can be implemented by exploiting time-scale separation. Here, we take the local MPPT control to operate fast, and the global MPPT control to operate relatively slowly. Specifically, on the time-scale of local MPPT control, the string current, Io, may be taken to be static or "quasi-static." Because the maximum power point of each panel is defined by a unique maximum power current, $I_{mp,i}$, the quasi-static string current naturally decouples MPPT control among the modules.

3.1.2.1 PV Model

Before discussing system performance further, we establish a model of the photovoltaic panel and its parameters. The circuit model used here (Fig. 3.4) is common in the literature, e.g. [3.16]. Given the parameters quoted in a typical datasheet, V_{oc}, I_{sc}, and the maximum power voltage and current, V_{mp}, and I_{mp}, analysis of the circuit in Fig. 3.4 yields (3.2)-(3.5).

$$V_{dp} = V_{oc} \tag{0.21}$$

$$R_s = \frac{V_{oc} - V_{mp}}{I_{mp}} \tag{0.22}$$

$$R_p = \frac{I_{sc}R_s - V_{oc}}{I_{mp} - I_{sc}} \tag{0.23}$$

$$I_{ph} = I_{mp} + \frac{V_{fwd}}{R_p} \tag{0.24}$$

where V_{dp} is the forward voltage of the diode, D_p, in the model. In Fig. 3.4, when $I_{in} < I_{mp}$, the diode, D_p, is forward-biased and it is reverse-biased otherwise. The resulting panel voltages are:

$$
\begin{aligned}
V_{in} &= V_{dp} - I_{in}R_s, & I_{in} < I_{mp} \\
V_{in} &= R_p I_{ph} - (R_s + R_p)I_{in}, & I_{in} \geq I_{mp}
\end{aligned}
\tag{0.25}
$$
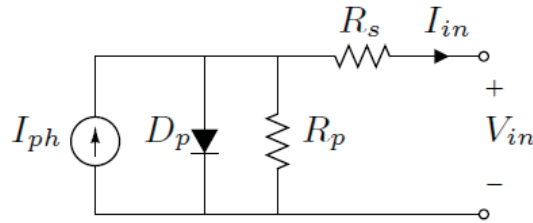
Fig. 3.4: PV circuit model

and the panel power is simply:

$$P_{in} = I_{in}V_{in} \qquad (0.26)$$

For simplicity, the rest of this work assumes the following nominal datasheet values adapted from a Mitsubishi PV-MF170EB4 [3.28]:

$$
\begin{aligned}
I_{mp} &= 6.93\text{A} \\
V_{mp} &= 24.6\text{V} \\
I_{sc} &= 7.38\text{A} \\
V_{oc} &= 29\text{V}
\end{aligned}
\qquad (0.27)
$$

3.1.2.2 Local Maximum Power Point Tracking

Local MPPT control consists of matching the string current, to the panel's own $I_{mp,i}$'s. From Fig. 3.1, the ith panel current is

$$I_{in,i} = Q_i I_o \qquad (0.28)$$

Given a quasi-static string current, Io, the modules each choose a Q_i to maximize their panel power. This maximization step can be performed a number of ways. For instance, the modules may estimate their $I_{mp,i}$'s via short-circuit current measurements. References [3.29]-[3.33] discuss MPPT control by this method. A perturb and observe step may be necessary for good accuracy following the initial Imp guess. In our system, having discrete conversion ratios, a maximum of two additional observations should be required to determine the actual optimal conversion ratio.

In the simulations that follow, the local algorithm for choosing conversion ratios was implemented as follows. Given $I_{mp,i}$ either by the short-circuit method described above or otherwise, the modules attempt to minimize the error $\left| I_{in,i} - I_{mp,i} \right|$. This

96

minimization is constrained according to the nonlinear behavior of the PV indicated in

Fig. 4. Combining (3.6) and (3.7), the panel power for the ith panel can be written:

$$
\begin{aligned}
P_{in,i} &= I_{in,i} V_{dp,i} - I_{in,i}^2 R_{s,i} & I_{in,i} < I_{mp,i} \\
P_{in,i} &= I_{in,i} R_{p,i} I_{ph,i} - \left(R_{s,i} + R_{p,i} \right) I_{in,i}^2 & I_{in,i} \geq I_{mp,i}
\end{aligned}
\tag{0.29}
$$

Taking the derivative of (3.10) with respect to $I_{in,i}$ yields

$$
\begin{aligned}
\frac{\partial P_{in,i}}{\partial I_{in,i}} &= V_{dp,i} - 2 I_{in,i} R_{s,i} & I_{in,i} < I_{mp,i} \\
\frac{\partial P_{in,i}}{\partial I_{in,i}} &= R_{p,i} I_{ph,i} - 2 \left(R_{s,i} + R_{p,i} \right) I_{in,i} & I_{in,i} \geq I_{mp,i}
\end{aligned}
\tag{0.30}
$$

The term, $-2\left(R_{s,i} + R_{p,i} \right) I_{in,i}$, in the derivative typically leads to a steep decrease in

panel power for $\left| I_{in,i} - I_{mp,i} \right|$. Absolute errors $\left| I_{in,i} - I_{mp,i} \right|$; impact the panel power

less for $I_{in,i} < I_{mp,i}$. Accordingly, the algorithm adopted in this work attempts to

minimize the error $\left| I_{in,i} - I_{mp,i} \right|$ with the following order of preference:

1) $I_{in,i} = I_{mp,i}$
2) $I_{in,i} < I_{mp,i}$
3) $I_{in,i} > I_{mp,i}$

In the examples presented here, the DC-DC modules each continuously attempt to

match the string current to their own MP currents according to the above algorithm.

Generally, the modules can choose from a set of integral conversion ratios [0,1...Q$_{max}$].

The Q = 0 module configuration is important for good average tracking efficiency. It is

equivalent to the passthrough mode discussed in [3.7] and represents the option for a

panel to "sit out" when its maximum power is so low that including it in the string

would have a negative impact on the global MPP.

3.1.2.3 Global Maximum Power Point Tracking

The string inverter can track the global MPP by adjusting its input current. Fig. 3.5 depicts an example of the tracking efficiency achieved as Io is swept, while the DC-DC modules adjust their conversion ratios. For this example, and for the rest of this section, tracking efficiency is considered in an otherwise lossless system (η_c = 100%). Section 3.1.4 addresses the effect of converter efficiency on MPPT control. The I_o sweeps, like the one depicted in Fig. 3.5, may be performed on a scheduled basis. Alternatively, I_o may be varied continuously according to a particular runtime MPPT algorithm. Section 3.1.4.5 presents a simulation of a likely input current-controlled inverter.
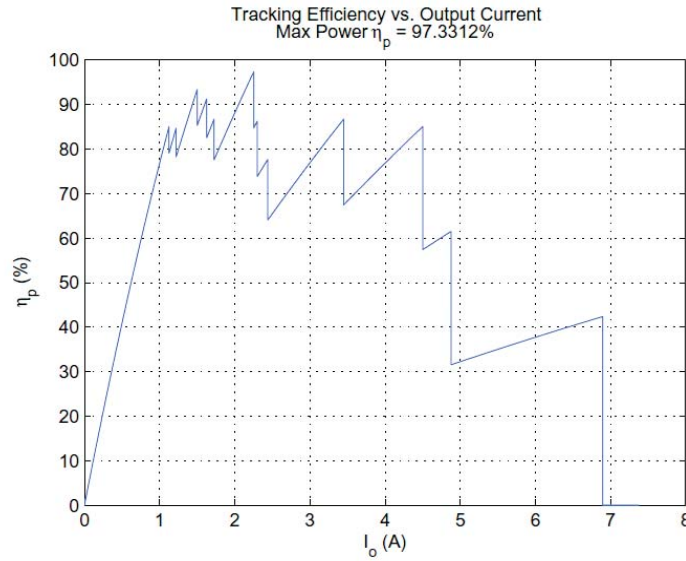

Fig. 3.5 A single I_o sweep with the following paramters: 3 panels, Q_{avail} = [0,1,2,3,4], $I_{mp;vec}$ = [6.898, 4.503, 4.878] A, ΔIo = 1 mA

3.1.2.4 Statistical Performance Evaluation

A statistical performance evaluation method was adopted to account for variations in panel MPP's. Monte Carlo simulations were performed by allowing MATLAB to

choose random (normalized) $I_{mp,i}$'s for each panel. For each simulation, the string current, I_o, was swept as in Fig. 3.5 and the maximum efficiencies (tracking, converter, and total) were recorded. Repeating this many times and averaging the results yielded a prediction of average performance.

An example output plot is shown in Fig. 3.6. The plot in Fig. 3.6 reveals that tracking efficiency can be very high for only a few panels. As panels are added, η_p diminishes to a limited extent. The local MPPT algorithm implemented impacts this behavior significantly. For instance, if the order of preferences listed in Section 3.1.2.2 is reversed, the tracking efficiency diminishes steadily as panels are added rather than flattening as it does in Fig. 3.6. The Monte Carlo simulation results also show how average tracking efficiency improves as the number of available levels increases. The tracking efficiency predicted for a 3-panel, 5-level system is approximately 90%. Increasing the number of available levels to 8 increases the predicted tracking efficiency to 95%.
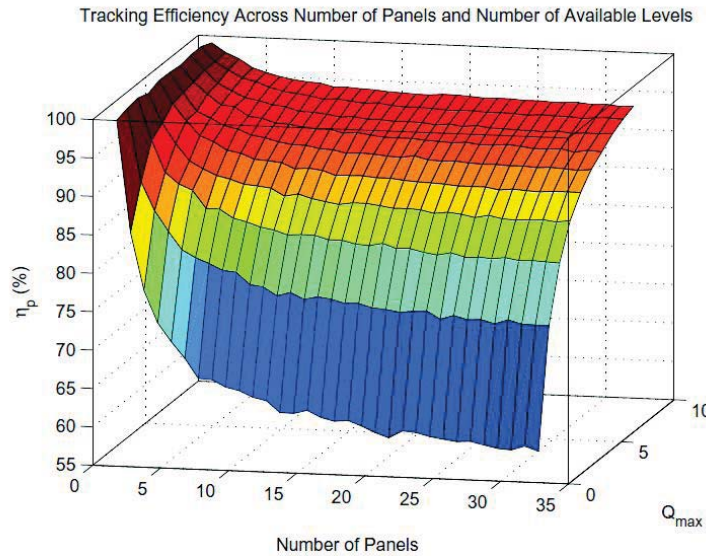
Fig. 6: Monte Carlo performance prediction: Q_{avail} = [0 : 1 : Q_{max}], Monte Carlo Length = 200, $I_{o,sweep}$ = [0.01 : 0.02 : 6.93] A

Finally, it should be noted that the $Q_{max} = 1$ case (i.e. $Q_{avail} = [0; 1]$) is somewhat representative of a simple series string of panels with bypass diodes. The statistical data predict roughly 65% average tracking efficiency while a 5-level MIC would improve that efficiency to roughly 90%

3.1.2.5 Effect of spatial panel separation

In the above example, the panels are assumed to have a random and uncorrelated distribution of MPP's. Intuitively, this model becomes inappropriate as panels become closely spaced. To model the effect of statistical correlation between MPP's for panels arranged in a non-infinite area, the randomly assigned panel MPP's can be constrained to a fraction of the full range. The simulation above was repeated having forced the MPP's to lie within 50% of the full range for each Monte Carlo iteration. The results show universally higher average tracking efficiencies. For instance, the tracking efficiency predicted for a 3-panel, 5-level system is approximately 95:5% and for a 3-panel, 8-level system, 97:4%.

3.1.2.6 Non-integral level selections

So far, we have considered only switched capacitor multilevel converters having integral, boosting sets of conversion ratios. There are many switched capacitor topologies that can achieve rational and bucking conversion ratios as well. Such a topology choice may be beneficial when considering upper bounds on DC bus voltages or other practical issues. A more thorough investigation will be the subject of future work.

3.1.3 Switched Capacitor Implementation

One particular realization of the switched capacitor MICs in Fig. 3.1 is the Marx Multilevel converter. By forming series and parallel combinations of the the input source and the switched capacitors, the 5-level Marx converter shown in Fig. 3.7 can achieve conversion ratios $Q_{avail} = [0; 1; 2; 3; 4]$.

3.1.3.1 Efficient Switching Patterns

Switching cycles consist of a recharge phase, ϕ_1, and an output phase, ϕ_2. During ϕ_1, the switched capacitors are disconnected from the load and charged in parallel with the source. During ϕ_2, one of several series-parallel configurations of the switched capacitors and input source is chosen to achieve the desired conversion ratio. Many redundant switching configurations are possible. The switching configurations shown in Fig. 3.8 were chosen for the 5-level Marx to minimize the conduction losses that will be quantified shortly. Generally, the switching configurations were chosen to minimize capacitor droop and the number of switches in the output current path, both of which lead to loss and load regulation. Rules of thumb to minimize capacitor droop include 1) utilize the input source to drive the output during ϕ_2 when possible and 2) utilize all of the switched capacitors when driving the output, e.g. parallel-connect redundant capacitors when possible.
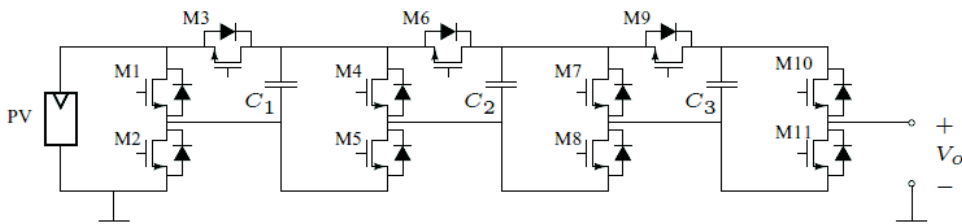
Fig. 3.7 A 5-Level Marx converter
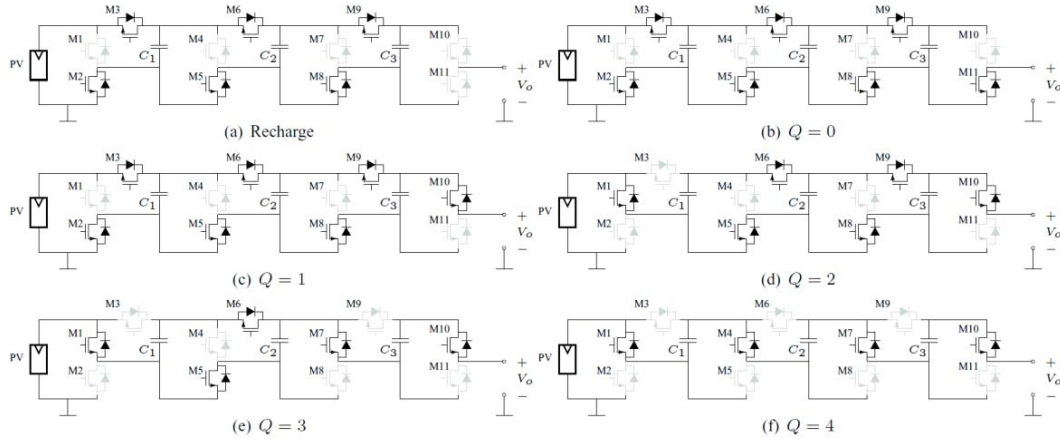
Fig. 3.8 Switching configurations

Switched capacitor circuits can achieve very high conversion efficiency by minimizing the instantaneous current flow through their effective output resistance, $R_{out,i}$. In a DC-DC switched capacitor circuit, the output is slowly-varying on the time-scale of one switching period. These facts guide us to particular modes of operation. In particular, efficient operation can be achieved when the same output phase (ϕ_2) configuration is repeated every cycle. In contrast, modulation of the ϕ_2 configuration on a per cycle basis, e.g. to achieve intermediate conversion ratios, would be ill-advised as it would lead to continuously varying open circuit converter voltages resulting in high instantaneous currents (high AC rms currents) through $R_{out,i}$. This observation leads directly to the constraint that the Marx Multilevel converter can (efficiently) achieve a discrete set of conversion ratios.

3.1.3.2 Linear Modeling

A linear modeling approach was adapted from the work in [3.34]. This linear modeling effort yielded quantitative support for the linear circuit models shown in Fig. 3.1

including the output resistances, $R_{out,i}$ which represent both loss and load regulation in the switched capacitor circuits [3.34].

3.1.3.3 Switching Speed Limit Definitions

According to [3.34], loss and load regulation mechanisms can be differentiated among two switching speed limiting cases. In the slow-switching-limit (SSL), the switched capacitors fully equilibrate yielding impulsive capacitor currents. In the fast switching-limit (FSL), the switched capacitors maintain fixed voltages while capacitor currents during each switching state are constant [3.34]. The two switching speed limits can be understood by considering the classic capacitor charging loss problem depicted in Fig. 3.9. The total energy lost in charging the capacitor is the time-integral of $I_C(t)^2 R$:

$$Etot = -\frac{\left(V_s - V_C(0)\right)^2}{2R} RC \left(e^{-2t/RC}\right)\Bigg|_0^t \qquad (0.31)$$

In the SSL, the exponential term is allowed to collapse to -1 and the energy lost becomes

$$E_{tot,SSL} = \frac{1}{2} C \Delta V_C^2 \qquad (0.32)$$
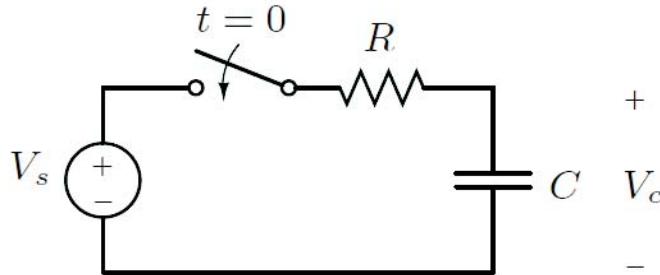
Fig. 3.9 The canonical circuit for studying the fundamental loss associated with charging a capacitor.

103

independent of R, and in agreement with the classical result. In the FSL, (3.12) can be viewed near t = 0 with the Taylor series approximation to the exponential term. This leads to

$$E_{tot,FSL}(t) = \frac{\left(V_s - V_C(0)\right)^2 t}{R} \tag{0.33}$$

i.e. the loss we would expect for two fixed voltages connected across the resistor. Reference [3.34] shows how these two loss mechanisms yield asymptotic limits to the output resistance with proportionalities

$$R_{SSL} \propto \frac{1}{Cf_{sw}}$$
$$R_{FSL} \propto R_{ds,on} \tag{0.34}$$

The method developed in [3.34] for computing the multipliers to quantify R_{SSL} and R_{FSL} was adapted to the Marx Multilevel converter here. The results are summarized in Tables 3.1 and 3.2 for Marx converters having between two and eight available levels. Note that the multipliers in the tables need to be computed for each conversion ratio (switching pattern) for each number of available levels (topology). Also note that R_{FSL} depends on the duty ratio between ϕ_1 and ϕ_2, which was taken as D = 0.5 for all switching patterns here. Given the asymptotic limits, the actual output resistance for any combination of topology, C, f_{sw}, and $R_{ds;on}$ is generally

$$R_{out} \approx \max\left(R_{FSL}, R_{SSL}\right) \tag{0.35}$$

and the conduction loss per module is simply

$$P_{rloss} = I_o^2 R_{out} \tag{0.36}$$

Table 3.1 R_{SSL} Multipliers: $(x1/Cf_{sw})$

Levels Available:	2	3	4	5	6	7	8
Q = 0	0	0	0	0	0	0	0
Q= 1	0	0	0	0	0	0	0
Q = 2	-	1	1/2	1/3	1/4	1/5	1
Q = 3	-	-	2	3/2	1	5/6	2/3
Q = 4	-	-	-	3	5/2	2	3/2
Q = 5	-	-	-	-	4	7/2	3
Q = 6	-	-	-	-	-	5	9/2
Q = 7	-	-	-	-	-	-	6

Table 3.2 R_{FSL} Multipliers: $(xR_{ds,on})$

| Levels Available:	2	3	4	5	6	7	8
Q = 0	2	4	6	8	10	12	14
Q = 1	2	4	6	8	10	12	14
Q = 2	-	8	10	12.4	8.2	17.6	32.4
Q = 3	-	-	26	24	38	48.4	50.8
Q = 4	-	-	-	64	90	100	100
Q = 5	-	-	-	-	130	180	206
Q = 6	-	-	-	-	-	232	307
Q = 7	-	-	-	-	-	-	378

3.1.3.4 Switching Loss

The linearized model above captures loss due to output current conduction. When evaluating the design in Section 3.1.4, it will also be important to include switching loss, a loss mechanism not explicitly contained in the linearized circuit model of Fig. 3.1. The switching loss for any active switch (one that changes state between the two switching phases) can be quantified by considering the circuit shown in Fig. 3.10. All MOSFETs in the Marx converter reside in at least one loop consisting only of one or two other MOSFETs and a switched capacitor. In the Marx converter, the switched capacitor, C, in Fig. 3.10 will nominally exhibit a voltage equal to the panel voltage, V_{in}, because it is recharged to that potential each cycle. The total switching loss was estimated in terms of typical data sheet values using [3.35] for N active devices as

$$P_{swloss} = N \left(Q_g V_g + \frac{1}{2} Q_{loss} |V_{in}| + Q_{rr} |V_{in}| \right) f_{sw} \tag{0.37}$$

Examining the switching patterns shown in Fig. 3.8, one can extract the following pattern generalizing the number of active switches according to conversion ratio:

$$\begin{aligned} N &= 1, & Q &= 0 \\ N &= 3Q - 2, & Q &> 0 \end{aligned} \tag{0.38}$$
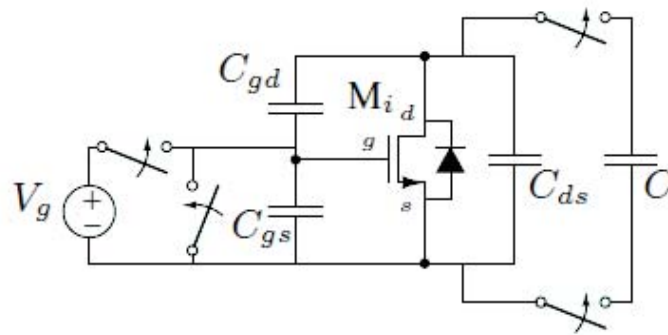
Fig. 3.10 Switching loss evaluation in the Marx converter for active MOSFETs

3.1.3.5 Inherent Features

Inherent to the topology of the Marx converter are a few interesting features that may add significant value to a solar power system. As mentioned previously, the Marx converter has a natural pass-through feature, replicating the function of bypass diodes and also the pass-through mode presented in [3.7]. The ability to disconnect each module from the load may be beneficial when implementing safety disconnect features. Reference [3.36] discusses the need for a disconnect in the event of a fire to prevent electrocution hazards that would otherwise result from the high voltage string output. This disconnect feature may also be particularly beneficial in implementing an anti-islanding mode. A good discussion of anti-islanding control and solutions for solar power systems can be found in [3.37].

The run-time local MPPT algorithm described above can be designed to automatically prevent under-voltage conditions at the panel output. Because the DC-DC modules continuously choose Q_i to closely match $I_{in,i}$ to $I_{mp,i}$, they automatically adjust to over-current conditions, choosing $Q_i = 0$ in the limiting case. This feature is advantageous when the local control circuitry is powered by the panel itself.

3.1.3.6 Gate Drive

The gate drive for the Marx converter needs to operate with a continuous floating gate drive voltage. The converter itself does not guarantee a periodic charging path to recharge a bootstrap capacitor. A level shift circuit is also required to translate ground-referenced logic signals to the gate drive output. The recommended topology (not necessarily the specific parts), adapted from [3.38], is shown in Fig. 3.11.

107
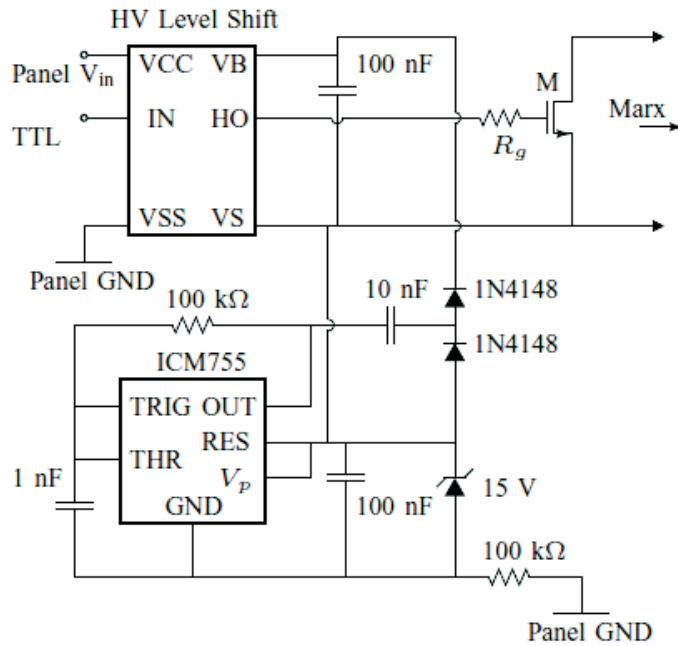
Fig. 3.11 The recommended gate drive adapted from IR AN-978 [3.38].

The 555 timer IC, 1N4148 diodes and floating capacitor form a charge pump circuit. The 100 kΩ resistor between the 555 timer GND and Panel GND and the 15 V zener allows the timer IC to float 15 V below the source of the driven MOSFET.

The low power version of the 555 timer IC (ICM755) is needed in this circuit to achieve low power dissipation in the part itself and to achieve sufficient quiescent current despite the 100 k resistor to ground. The charge pump drives the VB node to twice its supply voltage referenced to its own floating GND leading to a 15 V floating drive referenced to the MOSFET source. This voltage can be adjusted by choosing the voltage of the Zener diode. The "HV Level Shift" could be a commercial high side driver IC such as the IR2125. However, the high voltage rating of such a part would be under-utilized for a typical implementation of the system in this work. Therefore, a more cost-effective gate drive would include a custom level shift circuit.

108

3.1.4 Design Example

A 3-panel 510 W system was designed and simulated in SPICE and in MATLAB. Among the key topological considerations for implementing a practical Marx DC-DC MIC is the need for a power diode in series with the output of each module. This diode is required to block current from conducting backwards through the body diode of the upper MOSFET in the output stage during ϕ_1. In order to alleviate any need to synchronize switching action among modules, a local output non-electrolytic capacitor was placed across each module to create a local DC bus.

3.1.4.1 Number of Levels

The number of levels was chosen using the same Monte Carlo prediction methods described in Section 3.1.2.4. Having enumerated loss mechanisms, total efficiency was used to determine performance. To choose an appropriate number of levels, an unoptimized but lossy system was simulated using nominal circuit parameters and MOSFET device characteristics. The predicted performance is plotted in Fig. 3.12. The data show diminishing returns in total efficiency beyond 5 levels. Therefore a 5-level Marx converter was chosen as the MIC.

3.1.4.2 MOSFET Choice and Switching Frequency Optimization

Having chosen a reasonable value for the non-electrolytic (metal film) switched capacitors in the 5-level marx, the choice of MOSFET and switching frequency were optimized together. It is significant that all MOSFETs in the Marx converter reside in loops containing a switched capacitor and other MOSFETs only. MOSFET drain-source voltages are therefore upper bound by the maximum panel voltage. Accordingly, it is
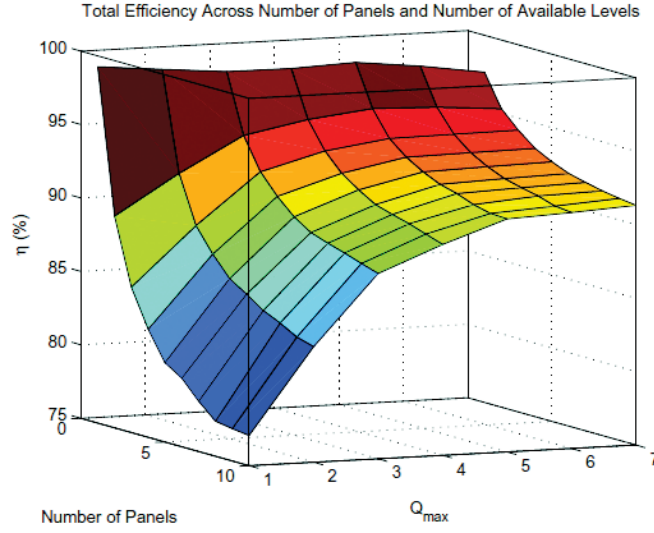
Fig. 3.12 Unoptimized system performance prediction: Q_{avail} = [0 : 1 : Q_{max}], **Monte Carlo Length = 400,** $I_{o;sweep}$ = [0.01 : 0.02 : 6.93] **A, C = 12.5 µF, f_{sw} = 250 kHz, R_{dson} = 10 m, Q_g = 10 nC, Q_{oss} = 5 nC, Q_{rr} = 25 nC, V_g = 15 V, V_{oc} = 29 V, V_{mp} = 24.6V, I_{sc} = 7.38 A, I_{mp} = 6.93 A, Distribution Compression = 50%**

particularly advantageous to choose a panel whose open-circuit voltage is just below a standard value for V_{dss}. Over-sizing the MOSFET beyond the required V_{ds} rating would lead to unneeded switching or conduction loss and a suboptimal design. A number of likely MOSFETs were identified having V_{dss} = 30 V for the panel open-circuit voltage of 29 V. The likely MOSFETs were chosen based on their on-resistance, $R_{ds;on}$, and gate capacitance, C_g. With the losses derived in (3.17) and (3.18), the performance was plotted for each MOSFET across switching frequency and conversion ratios. Fig. 3.13 shows such a plot for the selected MOSFET. A maximum average converter efficiency (across all conversion ratios) of > 98% was predicted at a switching frequency of 360 kHz. Note that the gate drive voltage was decreased from 15 V in the unoptimized system to 10 V in the optimized system. Adjusting the gate drive voltage trades off conduction loss (on-resistance) for switching loss.

MPP Converter Efficiency vs. Switching Frequency across Conversion Ratio
IRF8721----: Max Avg Efficiency = 98.3396% @ f_{sw} = 360 kHz
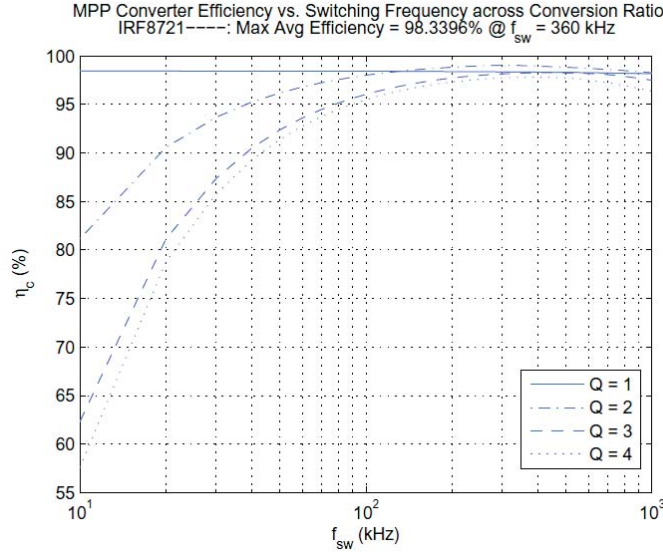
Fig. 3.13 MOSFET and switching frequency evaluation at peak power: IRF8721, C = 12.5 μF, V_{mp} = 24.6 V, I_{mp} = 6.93 A, MP = 170 W, V_g = 10 V

3.1.4.3 Power Diode

The power diode was chosen primarily to support the peak output current and to block the peak reverse voltage safely. Secondly, it was chosen for low capacitance, forward voltage, and ESR. Having added output diodes to the implemented system, the additional losses can be estimated as follows:

$$V_{fwd,i} = \ln\left(\frac{I_o}{I_s+1}\right)n\frac{kT}{q} + ESR_{diode}I_o \qquad (0.39)$$

$$P_{diode} = I_o \sum_i V_{fwd,i} + f_{sw}C_{j,i}V_{rr,i}^2 \qquad (0.40)$$

where V_{rr} is the reverse voltage during ϕ_1 and C_j is the junction capacitance of the diode. This expression can be used to improve the accuracy of the Monte Carlo performance predictions. The power diode chosen for this example was the Motorola MBR20100C Shottky [3.39]

111

3.1.4.4 Simulated Prototype

The optimized system was simulated using SPICE and MATLAB. The performance of this system was predicted with Monte Carlo methods having incorporated the losses derived in (3.17), (3.18) and (3.21). The results are shown in Table 3.3. A summary of circuit elements selected for the simulated prototype is shown in Table 3.4.

Table 3.3 Simulated statistical performance: 5-level, 3 Panel optimized system: Monte Carlo Length = 100, Distribution Compression = 50%, ΔIo = 1 mA, Diode Loss = [on]

Efficiency	symbol	simulated result
tracking	η_p	95.43%
conversion	η_c	97.56%
total	η	93.10%

Table 3.4 Circuit component summary

Component	Part No. / Value	Note
Switched Capacitors, Output Capacitor	12.5 μF	Metal Film 1‖4.7 ‖ 6.8 μF
Panel Capacitor	25 μF	12.5 ‖ 12.5 μF
MOSFET	IRF8721	
Output Diode	MBR20100C	

112

It is important to realize that the central inverter cannot track panel power, corresponding to η_p, directly. Instead it tracks its input power, corresponding to η. Having incorporated the loss mechanisms from Section 3.1.3 and in (3.21), this observation was accounted for in simulation by allowing the inverter to choose the I_o that maximized its input power. Tracking efficiency was recorded for comparison to total efficiency. A single experiment was performed in simulation to validate the linear modeling effort and loss calculations above. A fixed set of conversion ratios and MPPs was chosen for the three panels. Tracking, conversion, and total efficiencies were plotted for a single Io sweep. Fig. 3.14 compares the results for calculated data based on Section 3.1.3 and (3.21), a SPICE simulation of the linearized model and a SPICE simulation of the MOSFET system. The difference in η_c between the linearized model
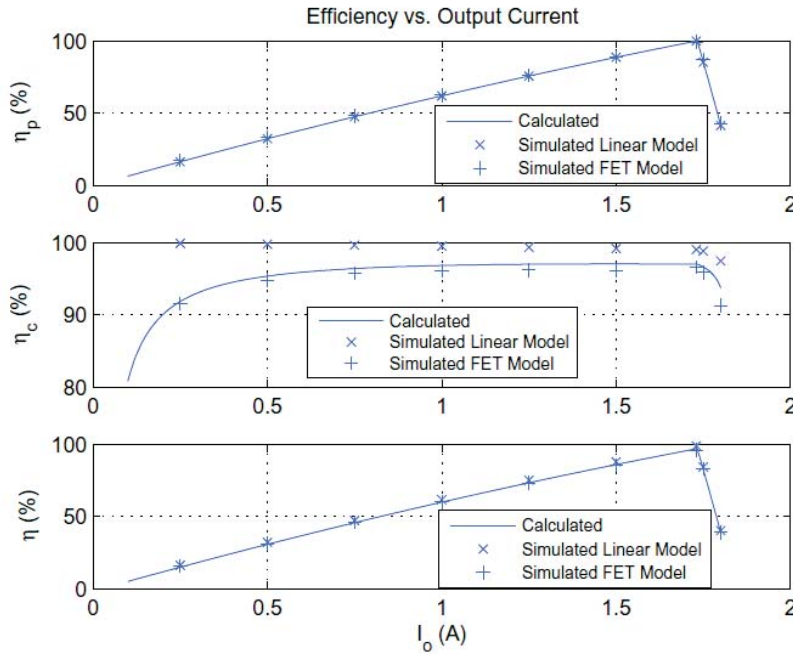

Fig. 3.14 Model Validation: Single I_o sweep, 3 sources, Q = [0, 2, 4], $I_{mp;vec}$ = [0.007 3.465 6.93] A, C = 12.5 μF, f_{sw} = 360 kHz, MOSFET: IRF8721, Vg = 10 V, deadtime = 100 ns, Rg = 4 Ω

and the other two data sets represents switching and output diode loss. Errors between the calculated model and FET simulation are likely due to estimation errors in computing diode and switching losses. Note that in the plots of Fig. 3.14, the maximum in total efficiency lines up closely with the maximum in tracking efficiency.

Time domain waveforms from the simulated system are shown in Fig. 3.15. Fig. 3.15(a) shows a zoom-in of the capacitor currents. The shape of those currents indicates operation between the slow and fast switching limits defined in Section 3.1.3.3.

This result is a natural outcome of the MOSFET choice and switching frequency optimization step above. Fig. 3.15(b) shows panel input currents during a step change in the load current from 90% to 100% of the predicted maximum power current.

In this example, Panel 1 is bypassed ($Q_1 = 0$) because its MPP is quite low; $I_{in1} = 0$ in the plots. The other two panels initially settle close to their respective $I_{mp;i}$'s - Panel 2 exhibits half of the photovoltaic current that Panel 3 does. When the load current steps to its maximum power value, Iin2 and Iin3 settle on their respective $I_{mp;i}$'s.

(a) Capacitor Currents   (b) Load Step - Currents
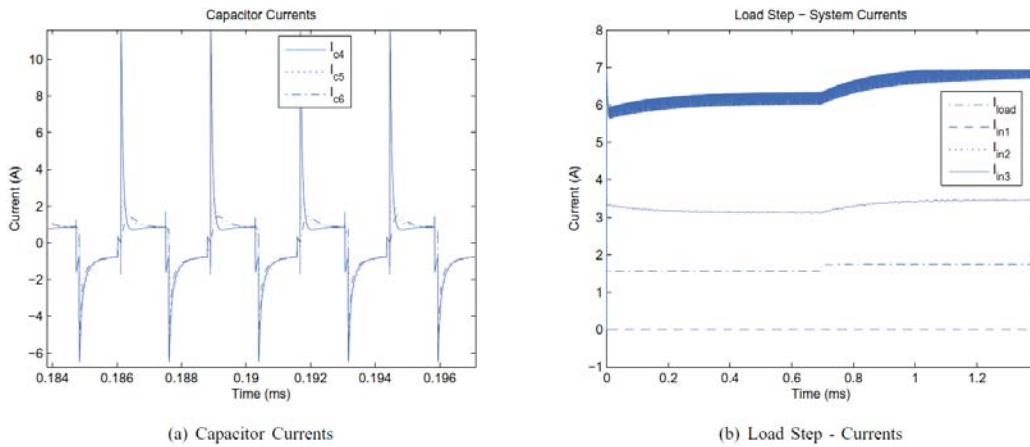
Fig. 315 Time-domain waveforms.

114

3.1.4.5 DC AC Dynamics

A linearized model of the central input current-controlled inverter is shown in Fig. 3.16.

The closed-loop transfer functions of particular interest can be derived from that circuit.

They are:

$$\frac{\hat{i}_{in}}{v_{in}}(s) = \frac{M^2(D)}{sL_e + R_e + R \square \frac{1}{sC}}\left(\frac{1}{1+T(s)}\right) \tag{0.41}$$

$$\frac{\hat{i}_{in}}{v_{ref}}(s) = \frac{A(s)}{1+A(s)} \tag{0.42}$$

$$A(s) = G_c(s)F_m\left(j(s)+e(s)\frac{M^2(D)}{sL_e + R_e + R \square \frac{1}{sC}}\right) \tag{0.43}$$

$$F(s) = HR_{sense} \tag{0.44}$$

$$T(s) = AF \tag{0.45}$$
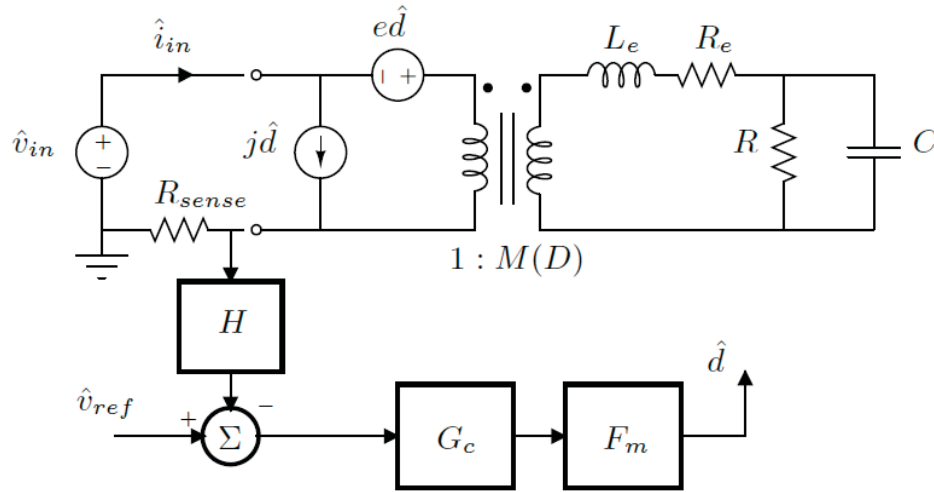
Fig. 3.16 A linearized model of an input current-controlled inverter front-end.

115

The linear model parameters, e, j, M(D), L_e, and R_e were chosen for a 500 W buck-derived inverter topology [40]. Fig. 3.17 shows step responses of the closed-loop transfer functions in (3.22) and (3.23). They show relatively fast settling times in the input current upon step transients in the input voltage (corresponding to the string DC bus voltage) and the reference voltage (corresponding to the control for the sweepable input current). The lower plot also indicates a significant attenuation of the input current response to changes in the input voltage. This attenuation is largely dependent on the low-frequency magnitude of the loop gain T(s) as indicated by (3.22).
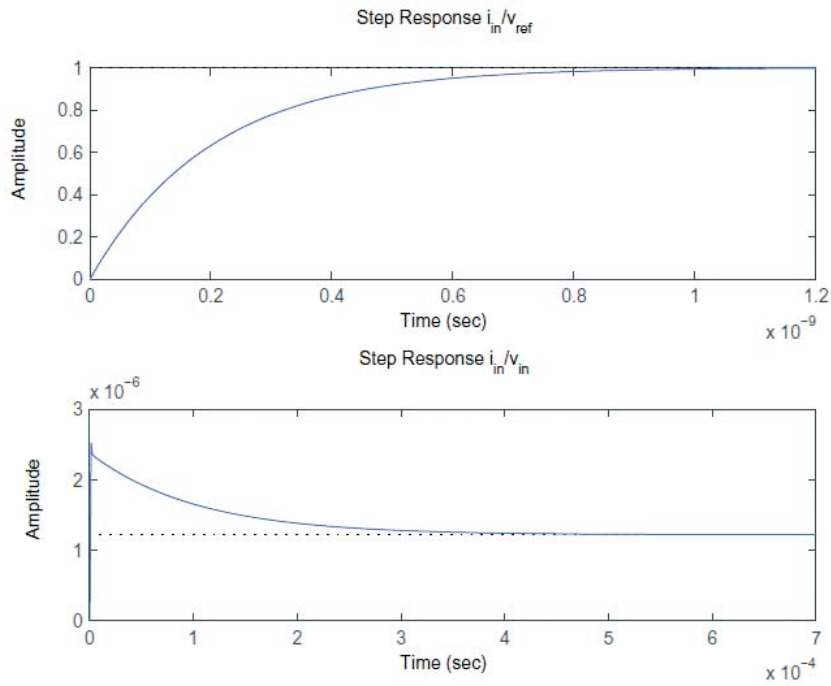
Fig. 3.17: Inverter closed-loop step responses

3.2 Improved Transient Response Control Strategy and Design Considerations for Switched- Capacitor (SC) Energy Buffer Architectures

3.2.1 Introduction

A power conversion interface between a DC and a single-phase AC system requires an energy buffer to store the instantaneous power difference between the constant power of the DC port and the time-varying power of the AC port. Traditionally, this energy buffer is implemented with large electrolytic capacitors. As the system reaches periodic steady state with unity power factor, the instantaneous power difference manifests itself as a voltage ripple on the energy buffering capacitor at double-line frequency. However, the single capacitor approach is known to achieve poor energy utilization [3.41].

Energy utilization is defined as the ratio of the energy used to buffer the instantaneous power difference to the maximum stored energy on the capacitor. Energy utilization for single capacitor energy buffers with respect to the peak-to-peak ripple ratio can be derived as:

$$E_{util} = \frac{2r}{1+r+0.5r^2} \qquad (0.46)$$

where r is the prescribed peak-to-peak ripple ratio. For instance, in a system with 10% peak-to-peak ripple ratio, the single capacitor energy buffer implementation has an energy utilization of less than 20%. In other words, the capacitor has to store more than 5 times the energy as actually needed.

Many alternative techniques have been proposed to manage the double-frequency energy flow [3.41-3.45]. In particular, the recently introduced switched-capacitor (SC) energy buffer architectures [3.46, 3.47] can achieve higher energy utilization and lower

117
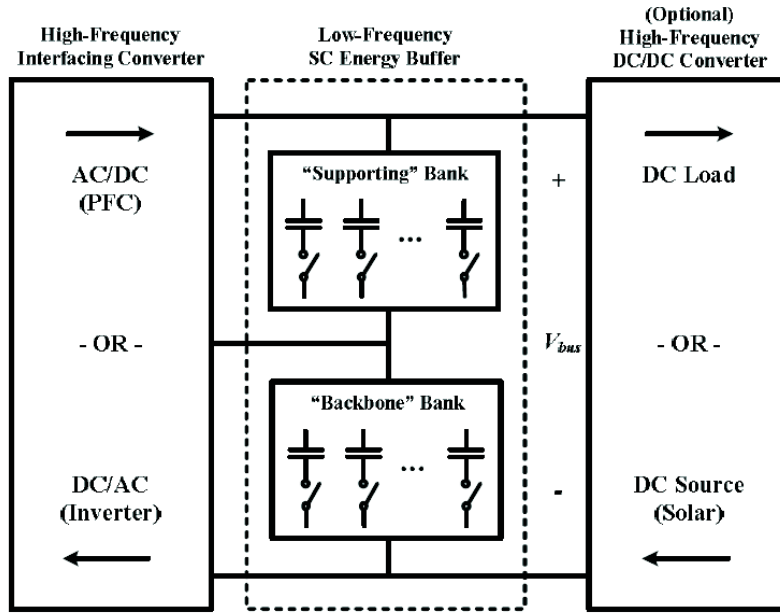
Fig. 3.18 General architecture of the SC energy buffer.

voltage ripple. Fig. 3.18 shows the general architecture of the proposed SC energy buffer. The SC energy buffer consists of two banks of capacitors shown as one possible example in Fig. 3.18: "backbone" capacitors and "supporting" capacitors. The configuration will be described as y-z, where y is the number of capacitors in the backbone bank and z is the number of capacitors in the supporting bank.

The backbone capacitor bank contains capacitors that withstand large voltage variations during the ripple cycle, where the voltage variations are typically much greater than the prescribed peak-to-peak ripple allowance. In order to bring the bus voltage ripple within bound, the supporting capacitor bank is switched so that the voltages of the supporting capacitors are either added to or subtracted from the voltage of the backbone capacitor bank. The switching pattern is defined such that the resulting bus voltage satisfies the ripple specification. The supporting capacitors have to withstand a much smaller voltage variation during the ripple cycle. Specifically, in this two-bank energy buffer

architecture, the voltage variations on the supporting capacitors are limited to one-half the specified peak-to-peak bus ripple magnitude if the supporting capacitors and backbone capacitors are equally sized.

Using this technique with a peak-to-peak ripple ratio of 10%, energy utilization can be improved to >70% with one backbone capacitor and >80% with three backbone capacitors. Moreover, this technique enables the use of capacitors with smaller capacitance and lower voltage ratings, thereby making it possible to replace limited-life electrolytic capacitors with ceramic or film capacitors. Practical uses of this technique require control schemes that can produce acceptable transient responses to timevarying power levels. Section 3.2.2 examines different control schemes and exposes undesirable behavior under certain operating conditions. The second part of this section proposes a two-step control scheme while taking a comprehensive view of the design space, exploring tradeoffs between circuit topology and control. Topology selection and switching configurations are discussed in Section 3.2.3. Control strategy requirements and tradeoffs are examined in in Section 3.2.4. Finally, simulation results of the proposed control strategy in two different circuit topologies are presented in Section 3.2.5.

3.2.2 Control Algorithms

Different control schemes have been proposed for the SC energy buffer shown in Fig. 3.18 [3.46, 3.47]. Two approaches are reviewed briefly here, neither of which is necessarily satisfactory during transient operation. These two approaches illustrate different control design philosophies with regard to the bus voltage ripple relative to the overall level of power being processed. In the first case, discussed below in the context

119

of a PFC utility interface for providing power to a load, the controller offers a fixed peak-to-peak bus ripple, $\Delta V_{r,pp}$, for all but very low power levels during steady-state operation. In the second case, discussed in the context of a grid-tie inverter, the controller varies the steady-state bus ripple with the power level injected to the grid. In both cases, power delivery changes can result in large bus voltage transients.

3.2.2.1 Bus-Voltage Monitoring, Finite State Machine Control

We first illustrate a control problem in the case of a SC energy buffer inside a PFC utility interface. In this example, discussed in [3.47], the controller directly monitors the bus voltage and triggers finite-state-machine state transitions when the bus voltage is about to exceed pre-defined bounds. The switching pattern associated with each state is defined so that an increase in state number would boost the bus voltage up by $\Delta V_{r,pp}$ when the bus voltage dips below the lower trigger threshold, and a decrease in state number would drop the bus voltage down by $\Delta V_{r,pp}$ when the bus voltage rises above the upper trigger threshold.

Because the supporting capacitor voltages are not individually monitored, state transitions do not guarantee the desired boost or drop on the bus voltage, e.g., as shown in [3.47]. Also, the state machine is unaware of the power level and is not reset or "recentered" between ripple cycles, so power transients may cause the state to saturate at either the state associated with the lowest or the highest apparent energy. During this state saturation, the SC energy buffer no longer has any available state to contain the ripple in the saturation direction. Finally, because the controller attempts to maintain the bus voltage within constant DC boundaries at all times, a transient response to a new
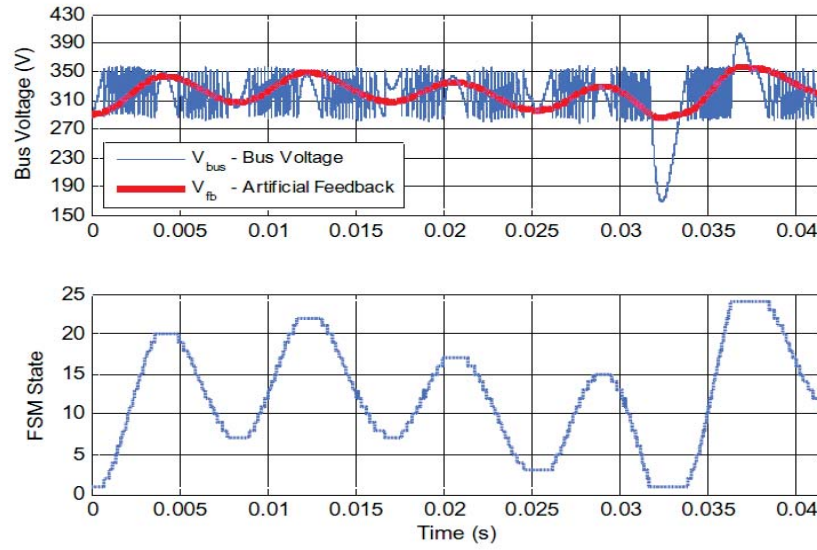
Fig. 3.19 Transient bus voltage response of a 2-6 SC energy buffer in a PFC due to a 30% load power step. The energy buffer uses bipolar switching configuration and is controlled by the bus voltage monitoring, finite state machine controller in [3.46]. The state variable saturates at the terminal states, 1 and 24, during the power transient, causing unacceptable ripple shootthrough.

steady-state power level can lead to extreme bus voltage transients as the controller will attempt to maintain the DC boundaries until it is driven into state saturation.

To investigate such undesirable behaviors, a SPICE simulation is performed using LTSpice from Linear Technology. A LT1249 active power factor controller is selected for the simulation because the model is readily available in the bundled component library. The simulated testbench circuit is derived from the typical application example in the datasheet [3.48] with the output filter capacitor replaced by the 2-6 SC energy buffer presented in [3.47]. In addition, the simulation model also incorporates the controller implemented with a 24-state finite state machine and an "artificial feedback voltage" reported in [3.47]. The design specifications include a nominal output voltage of 320V and a 20% peak-to-peak ripple ratio. The simulation results are shown in Fig. 3.19, where the bus voltage exhibits unacceptable over- and undershoots when the state

machine state saturates at states 1 and 24 in response to 30% load power level transients. Note that the artificial feedback voltage does not faithfully reproduce the over- and under-voltage conditions. The extreme overshoots from the shortcomings of the controller are amplified by two additional factors. The capacitances of the capacitors in the energy buffer are greatly reduced under the assumption of proper ripple reduction. Moreover, the capacitors are linked in series, which further diminishes the effective capacitance seen on the bus.

3.2.2.2 Supporting Capacitor Monitoring, Timing Interval Control

A similar control problem can be illustrated considering Fig. 3.18 in its inverter configuration. In this case, discussed in [3.46], the individual supporting capacitor voltages are monitored while giving up the task of controlling the backbone capacitor voltage to the energy-balance controller of the inverter. The control logic pre-computes the charge and discharge intervals for each supporting capacitor relative on the phase of the ripple cycle and enables these intervals when the capacitor voltages are within their reference minima and maxima [3.46]. The reference voltages scale linearly with power level and the ripple is reduced by a fixed ratio. Therefore, the resulting bus voltage behavior is very similar to that of a single capacitor implementation – the backbone capacitor experiences the natural transient and settling behaviors from the energy-balance controller, and the supporting capacitors are used to keep the ripple voltage within the prescribed limits.

However, this controller makes inefficient use of the supporting capacitor bank – all capacitors in the supporting bank are used regardless of power level. As a result, the supporting capacitor voltage references must be adjusted significantly in response to

power variations. Since the voltage on capacitors cannot change instantaneously, the supporting capacitors will need time to be charged or discharged to the new reference levels. This introduces a few cycles where the supporting capacitors experience large imbalance in their charge and discharge times. In the extreme case, the supporting capacitors may not be used in either the charge or the discharge cycle at all, thus exposing the bus to the full-swing ripple from the backbone capacitor with reduced capacitance during the corresponding half cycle.

A SPICE simulation is again used to demonstrate the potential problems with this control strategy. The simulated testbench circuit is implemented using the feedforward energy-balance controlled solar inverter demonstrated in [3.46] along with a 1-8 SC energy buffer. The nine supporting capacitors are monitored and managed by the controller with pre-computed switch timings discussed above, and the backbone capacitor is controlled by the feedforward energy-balance controller of the solar inverter. The design specifications include a nominal output voltage of 250V and a 10% peak-to-peak ripple at maximum power. As shown in Fig. 3.20, the bus voltage experiences an unacceptable undershoot when the supporting capacitor voltages references are dramatically increased in response to 30% power level transients. The second subplot in Fig. 3.20 shows the nonparticipation of the supporting capacitors during their discharge half-cycles, resulting in the lack of buffering during the discharge half cycle.

### 3.2.3 SC Energy Buffer Design Considerations

There are many tradeoffs to be considered in designing an SC energy buffer. A basis for making these tradeoffs is developed in this section. In principle, energy utilization can
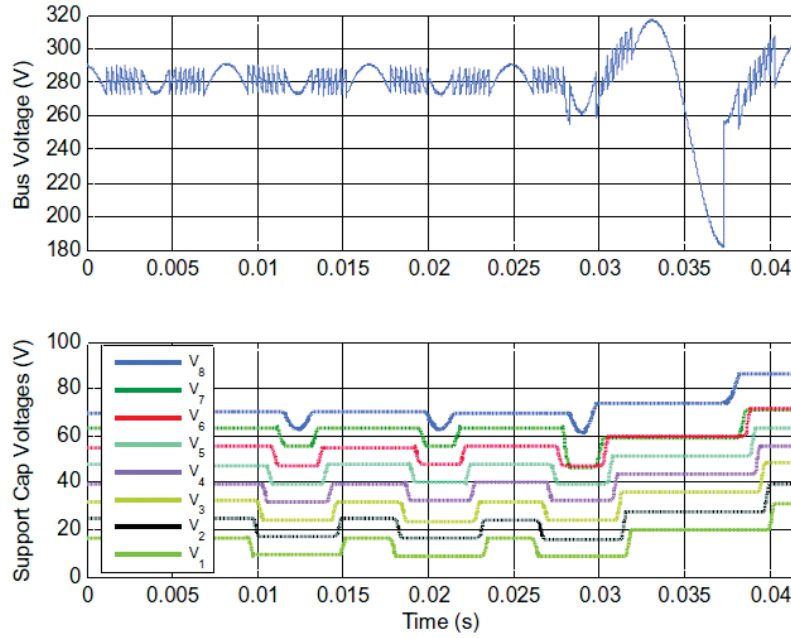
Fig. 3.20 Transient bus voltage response of a 1-8 SC energy buffer in a solar inverter due to a 30% input power step. The energy buffer uses the unipolar switching configuration and is controlled by the supporting capacitor monitor, timing interval controller. The discharge is disabled in order to charge the supporting capacitors up to the new reference values, exposing the full-swing backbone capacitor ripple.

be increased arbitrarily at the expense of switching frequency and buffer complexity.

Desirable transient performance implies new control requirements that also impact SC

buffer design. We consider these tradeoffs in the context of two general SC buffer

architectures, unipolar and bipolar switching configurations shown in Fig. 3.21.

A first consideration in designing the energy buffer is energy utilization when the

design goal is to reduce the overall amount of physical capacitance in the system.

Equation (3.27) summarizes the energy utilization for a non-switching, single

capacitance buffer. The energy utilization equation can be generalized for the SC case

shown in Fig. 3.18 by taking the sum of ΔE , the change in energy stored, divided by the

124
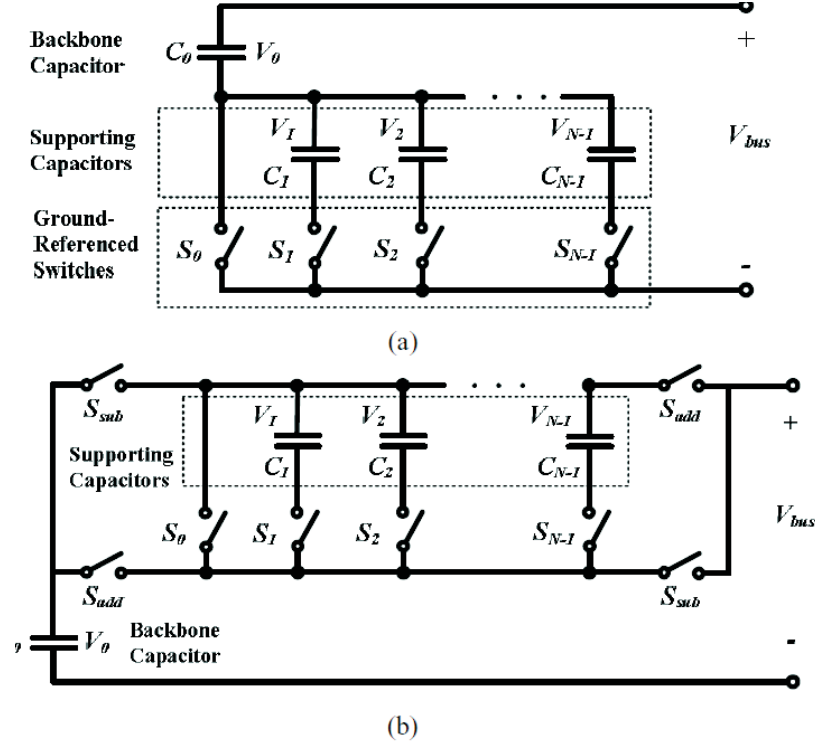
Figure 3.21 General 1-*z* architecture of SC energy buffer. (a) Implementation with ground-referenced switches only for unipolar switching configuration. (b) Implementation with four additional switches to achieve bipolar switching configuration.

sum of E_{max} , the maximum energy stored, of all the capacitors in the energy buffer . This is shown in (3.28).

$$
E_{util} = \frac{\displaystyle\sum_{j=1}^{y} \Delta E_{\text{backbone}}(j) + \sum_{i=1}^{z} \Delta E_{\text{support}}(j)}{\displaystyle\sum_{j=1}^{y} E_{\text{max,backbone}}(j) + \sum_{i=1}^{z} E_{\text{max,support}}(j)}
\tag{0.47}
$$

The variables in (3.28) depend on not only the nominal bus voltage, the specified ripple ratio and the selected capacitor size, but also the switching configuration. Thus, the two cases shown in Fig. 3.21 illustrate a tradeoff between topology and switching complexity versus capacitor utilization. Note that Fig. 3.21 illustrates the two cases with

a single backbone capacitor, i.e., y = 1 in each case, although more backbone capacitors could be employed with arbitrary y.
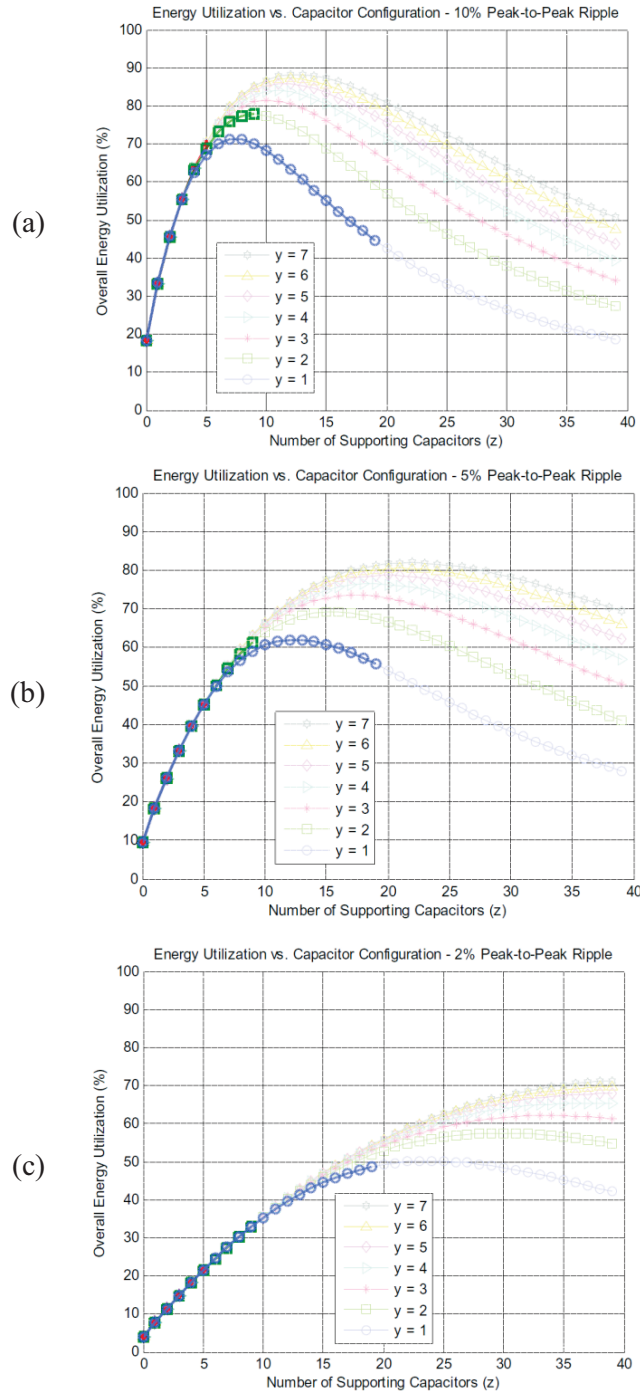
3.2.3.1 Capacitor Configurations

For illustration, the energy utilization of an SC energy buffer with bipolar switching configuration versus different numbers of backbone and supporting capacitors for three different ripple ratios is shown in Fig. 3.22. Two important conclusions can be drawn from these plots. First, for each ripple ratio and number of backbone capacitors used, there exists an optimal number of supporting capacitor which maximizes the energy utilization of the overall energy buffer. Secondly, the energy utilization can be improved with diminishing return by introducing more backbone capacitors.

However, the number of backbone capacitors cannot be increased indefinitely. The switching frequency of the SC energy buffer is directly proportional to the number of capacitors in the energy buffer. In particular, the switching frequency can be approximated as

$$f_{sw} \approx 2f_{grid} \square p \square y \square (z + 1) \tag{0.48}$$

where p = 2 for unipolar switching schemes and p = 4 for bipolar switching schemes. Clearly, increasing the number of capacitors would unavoidably increase the incurred switching loss. Also, excessive number of capacitors would cause the SC buffer switching frequency to approach that of the PFC or inverter controllers, consequently causing undesirable interactions between the two control loops.

In order to guarantee time-scale separation between the low frequency energy buffer control and high-frequency PFC or inverter control, the number of capacitors must be limited. When designing a switching converter, the switching frequency is expected to

Fig. 3.22 Overall energy utilization of the SC energy buffer as a function of the capacitor configuration. These numbers are computed for SC energy buffers with equally sized backbone and supporting capacitors using the bipolar switching configuration. Recall that y denotes the number of backbone capacitors and z denotes the number of supporting capacitors.

be high with respect to the natural frequency of the energy storage elements. This extends to the case of a SC energy buffer. While any specific case requires a control loop and stability analysis, a similar rule-of-thumb to keeping the natural time constant in the canonical models long compared to the switching period, e.g. 10 times the switching period, is to have the SC buffer switching at below 1/10 the frequency of the interfacing switching converter. As illustrated in Fig. 3.18, high frequency switching converters can be found on either side of the SC energy buffer.

For example, assuming the switching frequency of the high frequency loop is on the order of a hundred kilohertz, average switching frequency of the energy buffer control might be constrained to be less than approximately ten kilohertz. In other words, the relationship in (3.30) must hold.

$$p \Box y \Box (z+1) \le \frac{10\text{kHz}}{2f_{grid}} \tag{0.49}$$

This establishes an upper bound on the number of capacitors that can be incorporated in these SC energy buffers. Referring back to Fig. 3.22, the unfeasible combinations of capacitor configurations are greyed out. As shown, the achievable improvement in energy utilization is limited, albeit still significant, as this becomes a constrained optimization problem. For peak-to-peak ripple ratios of 2%, 5%, and 10%, the optimal achievable energy utilizations are realized with only one or two backbone capacitors.

In a SC energy buffer, the bus voltage is no longer an accurate measure of the energy stored in the energy buffer. Therefore, when integrating with conventional power-factor correction controllers or energy-balance inverter controllers, the bus voltage cannot be directly used as the feedback voltage. Reference [3.47], for example, uses an artificial feedback voltage to ensure compatibility with existing hardware. However, such an

artificial feedback voltage is not guaranteed to be sinusoidal and may not reliably detect under- and over-voltage conditions as shown previously.

By implementing the backbone capacitor bank with only one capacitor, a voltage feedback signal is available at the single backbone capacitor for interfacing with conventional power-factor correction controllers or energy-balance inverter controllers. Because there is a single path in the backbone capacitor bank through which the energy buffering current must flow, the single backbone capacitor voltage can be treated as an AC-scaled version of the single electrolytic capacitor voltage in traditional energy buffers.

Energy utilization is still high with a single backbone capacitor. Specifically, in the case of 10% peak-to-peak ripple ratio, using a single backbone capacitor reduces the achievable energy utilization from 77.9% to 71.2%, still a sizable improvement from 18.1%. In the cases of 5% and 2% peak-to-peak ripple ratios, the optimal energy utilizations remain unchanged. Also, this simplification enables the exclusive use of ground-referenced switches in unipolar switching configurations.

3.2.3.2 Switching Topology Tradeoffs

We therefore focus on the 1-z architecture shown in Fig. 3.21, where we define $N = z + 1$ as the total number of capacitors in the SC energy buffer. The backbone capacitor is denoted as C_0, and the supporting capacitors are denoted as C_1 through C_{N-1}. Two types of switching configurations can be explored: unipolar and bipolar. In unipolar switching, supporting capacitor voltages are added to the backbone capacitor voltage when it is too low, but are never subtracted. With equally sized capacitors, the resulting peak-to-peak bus voltage ripple with respect to the total number of capacitors is

$$\Delta V_{r,pp,unipolar} = \frac{2}{N+1} \cdot \left(\frac{P}{\omega_o \cdot C \cdot V_C} \right)$$

(0.50)

where P is the power level, ω_o is the angular frequency of the grid, C is the capacitance of all capacitors in the SC energy buffer, and V_C is the nominal voltage of the grid.

If the backbone capacitor voltage is regulated by energy balance control, i.e., to achieve constant mean squared voltage, using the unipolar switching configuration will result in a variable mean bus voltage. Specifically, the mean bus voltage will increase with increasing power level, but will always be above the regulated mean voltage of the backbone capacitor. For this reason, the unipolar switching configuration is unsuitable for PFC applications with constant output voltage requirements. However, it is compatible with solar inverters where the bus voltage must remain sufficiently high in order to maintain control of the grid. In addition, because the mean bus voltage is positively correlated to the power level, it ensures fast response time in hysteresis current controlled inverters when the output current amplitude is increased. Finally, the one-sided switching configuration also has the added benefit of being able to utilize ground-referenced switches only. By rearranging the supporting capacitor bank and the backbone capacitor as shown in Fig. 3.21 (a), the unipolar SC energy buffer avoids high-side gate drives.

In the bipolar switching configuration, four additional switches are added in order to invert the polarity of the supporting capacitor voltages during parts of the ripple cycle. This enables ripple reduction with a constant mean bus voltage. Supporting capacitor voltages are added to the backbone capacitor voltage when it is too low and are subtracted from the backbone capacitor voltage when it is too high. As such, the bipolar switching configuration is compatible with power-factor correction applications without

an additional dc-dc converter at the output. Moreover, the bipolar switching configuration uses the supporting capacitors more efficiently; it achieves a peak-to-peak voltage ripple of

$$\Delta V_{r,pp,bipolar} = \frac{1}{N} \cdot \left(\frac{P}{\omega_o \cdot C \cdot V_C} \right) \tag{0.51}$$

approximately twice as effective, in terms of ripple reduction capability versus number of capacitor added, as the unipolar switching configuration. The ripple adavantage requires four extra switches and high-side gate drives, which contribute to additional switching losses.

The steady-state maximum supporting capacitor voltages under maximum power rating for both switching configurations are outlined here to supplement energy utilization calculations and to facilitate capacitor selections.

$$V_{max,unipolar}(i) = \frac{i+1}{N+1} \cdot \left(\frac{P_{max}}{\omega_o \cdot C \cdot V_C} \right) \tag{0.52}$$

$$V_{max,bipolar}(i) = \frac{i+1}{2N} \cdot \left(\frac{P_{max}}{\omega_o \cdot C \cdot V_C} \right) \tag{0.53}$$

for $i = \{1,2, ..., N-1\}$. For the backbone capacitor, the maximum capacitor voltage is the same for both switching configurations and can be calculated as

$$V_{max}(0) = V_C + \frac{1}{2} \cdot \left(\frac{P_{max}}{\omega_o \cdot C \cdot V_C} \right) \tag{0.54}$$

In the following section, control strategies for both switching configurations are presented.

3.2.4 Two-Step Control Strategy

A controller capable of handling power level transients must not prescribe strict DC voltage boundaries constraints on the bus voltage. Instead it should allow the DC level of the bus voltage to undergo natural settling while maintaining the AC ripple magnitude within specification around the DC level. This enables the controller to evenly distribute the charge buffering to the supporting capacitors instead of leaving the terminal-state capacitors to absorb an unusual large amount of leftover charges. Also, the controller must effectively reset its state from ripple cycle to ripple cycle in order to guarantee the availability of reserve buffering states in the event of power transients. Finally, the controller must intelligently manage the supporting capacitors so they can remain effective in reducing the ripple magnitude at all time. This translates to maintaining the reference voltage levels of the supporting capacitors relatively constant regardless of power level.

These requirements can be satisfied by adopting a two-step control strategy: capacitor participation optimization and switch timing determination. The controller first determines the optimal number of capacitors to use in buffering the bus voltage, and then compute the switch timings for the allocated supporting capacitors to maximally reduce the bus voltage ripple. In a 1-z SC energy buffer configuration, the single backbone capacitor voltage is used as the feedback node to either a PFC or an inverter controller. Thus, the SC energy buffer controller discussed here passes the regulation of the backbone capacitor voltage to an external interfacing controller.

Two design examples will be presented to better illustrate the operation and the effectiveness of the proposed control strategy. The specification for the design examples is a 500W inverter with a 250V nominal bus voltage and a 10% peak-to-peak ripple
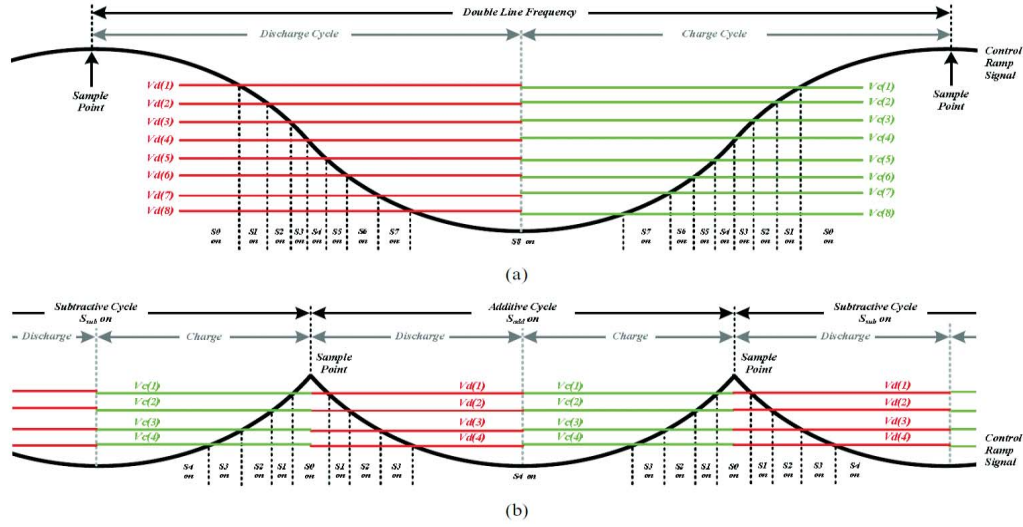
Fig. 3.23 Sampling points and control variables, $v_c(i)$ and, $v_d(i)$ in relation to the ripple cycle and the control ramps for (a) unipolar switching configuration and (b) bipolar switching configuration

ratio. For maximum energy utilization, a 1-8 SC configuration is chosen for the unipolar switching scheme. For the bipolar switching scheme, a 1-4 SC configuration is chosen for comparable switching complexity and ripple reduction power.

3.2.4.1 Capacitor Participation Optimization

In order to optimize the supporting capacitor participation, the controller samples the current power level and calculates the minimum number of capacitors required to keep the voltage ripple within the specification. The sampling frequency is twice the line frequency for the unipolar switching configuration and four times the line frequency for the bipolar switching configuration.

The sampling points with respect to the ripple cycle are illustrated in Fig. 3.23. Note that the minimum required number should have a lower bound at 1 because the backbone capacitor is always used, and can be derived by inverting the ripple magnitude (3.31) and (3.32) for the two different switching topologies. Equation (3.36) shows the

133

solution for the unipolar switching configuration and (3.37) shows the solution for the bipolar switching configuration. Note that *P[n]* is the sampled power level during the current ripple cycle.

$$N_{unipolar}[n] = \max\left(\text{ceil}\left(\frac{2P[n]}{\omega_o \cdot C \cdot V_C \cdot \Delta V_{r,pp}} - 1 \right), 1 \right) \tag{0.55}$$

$$N_{bipolar}[n] = \max\left(\text{ceil}\left(\frac{P[n]}{\omega_o \cdot C \cdot V_C \cdot \Delta V_{r,pp}} \right), 1 \right) \tag{0.56}$$

By only using the minimum required number of capacitors, the controller ensures that there is a sufficient number of capacitors in reserve, ready to kick in during a sudden power level increase. In addition, relatively constant energy storage in the supporting capacitors is maintained over a wide range of power levels. Consequently, the system is able to respond to large power transients by adjusting the number of capacitors used, rather than drastically changing the energy stored on all the supporting capacitors. Fig. 3.24 illustrates the supporting capacitor voltages and the expected ripple size across all possible power levels in the 1-8 unipolar SC energy buffer design example. The number of switching events is reduced as the power level decreases, which improves the overall system efficiency.

3.2.4.2 Switch Timing Determination

Given the number of capacitors to use, the controller proceeds to compute the switch timings for the capacitors based on the current power level. That is, the charge and discharge cycle durations are adjusted for each supporting capacitor based on the current sample of its voltage and its respective reference values.
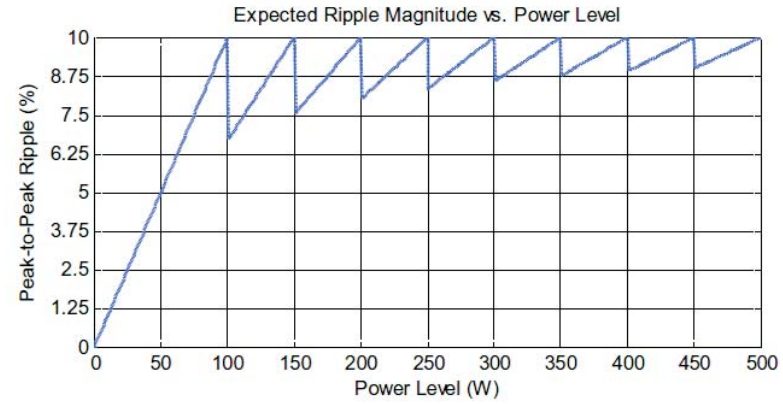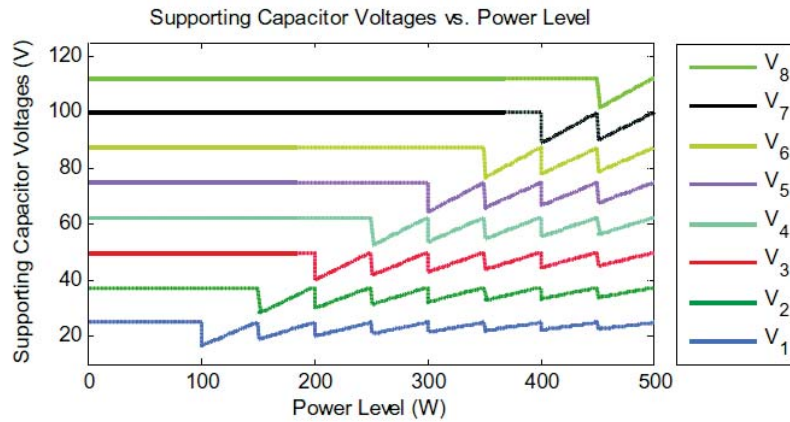
Fig. 3.24 Expected ripple magnitude and the supporting capacitor voltages as a function of power level for the 1-8 unipolar design example.

Since the charging and discharging of the capacitors by the double-line frequency energy flow are inherently nonlinear with respect to time, a nonlinear element is inserted into the control loop to enable the use of simple linear function in the rest of the controller. The nonlinear element takes form of a control ramp on which the switching event is triggered. For the unipolar switching configuration, the control ramp is a double-line frequency sine wave phase-locked to the grid. In addition, the unipolar control ramp is assumed to be normalized with unit peak-to-peak amplitude and ramps from 0V to 1V.

135

For the bipolar switching configuration, the ripple cycle can be further broken up into two sub-cycles. There is the additive sub-cycle where the supporting capacitor voltages are added to the bus voltage, and the subtractive sub-cycle where the supporting capacitor voltages are subtracted from the bus voltage. Thus, the same cycle duration computation needs to be performed twice as often as in the unipolar case. The control ramp function for the bipolar switching configuration then must be periodic at four times the line frequency. Specifically, the bipolar control ramp is a rectified and inverted version of the unipolar control ramp and ramps from 0V to 0.5V. The two control ramp signals in relation to their respective control voltages and sampling points are shown in Fig. 3.23.

Because the control ramps are assumed to be normalized, the control equations will also be defined in a power-independent fashion. All sampled values are normalized to the full-swing ripple magnitude on the backbone capacitor. The normalizing function is defined as

$$\overline{v}[n] = \frac{v[n]}{P[n]/(\omega_o \cdot C \cdot V_C)} \tag{0.57}$$

where v[n] is the sampled supporting capacitor voltage.

Based on the normalized sampled supporting capacitor voltages, the allowable discharge and charge durations for each capacitor are calculated from (3.39) and (3.40),

$$\mathrm{disch}(i) = \max\left(\min\left[\overline{v}_i[n] - \frac{i}{D_x[n]}, \frac{1}{D_x[n]} \right], \frac{k}{D_x[n]} \right) \tag{0.58}$$

$$\mathrm{charg}(i) = \max\left(\min\left[-\overline{v}_i[n] + \frac{i+2}{D_x[n]}, \frac{1}{D_x[n]} \right], \frac{k}{D_x[n]} \right) \tag{0.59}$$

Where $i=[1,2...N-1]$ denotes the supporting capacitor index, $1/D_x[n]$ is the normalized step in voltage between the supporting capacitors, and $k \in [0,1]$ determines the minimum

duration. The variable x in $D_x[n]$ denotes the switching configuration. The discrete step size definitions differ in the two switching configurations and are shown in (3.41) and (3.42).

$$\frac{1}{D_{unipolar}[n]} = \frac{1}{N_{unipolar}[n]+1} \tag{0.60}$$

$$\frac{1}{D_{bipolar}[n]} = \frac{1}{2N_{bipolar}[n]} \tag{0.61}$$

The minimum duration defined by k determines the tradeoff between transient ripple size and settling time. If k is very close to zero, the controller may allow the capacitor voltages to reach their new reference values quicker by imposing a large imbalance between their charge and discharge cycles. However, larger imbalances between the charge and discharge cycles increase exposure of the bus voltage to the ripples of the backbone capacitor, resulting in larger transient ripple. If k is very close to one, the controller will maintain ripple buffer throughout more of the ripple cycle. But the limited imbalance between the charge and discharge cycles results in longer settling times. Note that by managing the capacitor participation based on power level, the reference voltages for the supporting capacitors are kept fairly constant. Therefore, k can be set very close to one for adequate buffering without the risk of unreasonably long settling times.

Having computed the allowable charge and discharge durations for each supporting capacitor, the actual control voltages can be calculated by a cumulative sum. More specifically, the individual charge and discharge control trigger levels are

$$v_d(i) = \sum_{m=i}^{N_x[n]-1} \text{disch}(m) \tag{0.62}$$

.
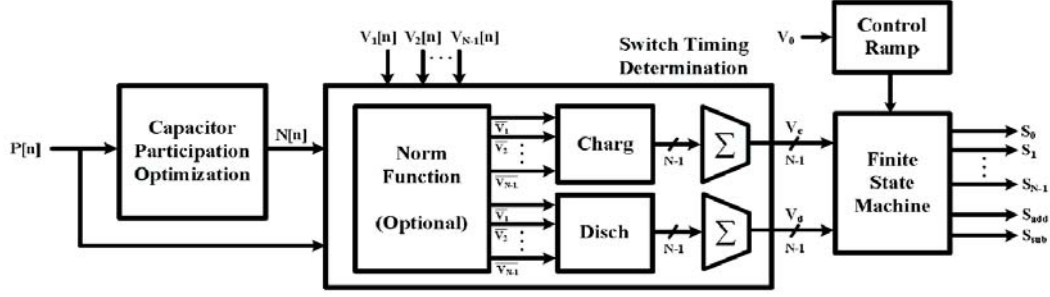
Fig. 3.25 Proposed two-level SC energy buffer controller block diagram, where V_o denotes the backbone capacitor voltage $V_i[n]$, for *i=[1,2,..N-1]* denotes the sampled supporting capacitor voltage V_c, and V_d correspond to the charge and discharge control signals respectively.

$$v_c(i) = \sum_{m=i}^{N_x[n]-1} \text{charg}(m) \qquad (0.63)$$

When $N_x[n]-1 < i$, the control voltage is set to zero, which means that supporting capacitor i is not being used in the current ripple cycle. Furthermore, higher-indexed switches have precedence over lower-indexed switches. That is, if $v_c(1)$, $v_c(2)$, … , $v_c(M) > v_{ramp}$, switches 1, 2, … , M-1 are all disabled, and only switch M is turned on. The complete two-step controller block diagram is shown in Fig. 3.25.

3.2.4.3 Distortion and Phase Error

In the previous section, the control ramps are assumed to be perfectly sinusoidal, or rectified sinusoidal, with zero phase error. Practical phase-locked loops may not guarantee zero steady-state phase error. If a phase error persists between the control ramp and the actual ripple cycle, systematic errors would be introduced to the steady-state voltages of all supporting capacitors, which would result in an increased overall bus voltage ripple. Additionally, the grid voltage may not be perfectly sinusoidal and the ripple voltage may exhibit distortions. Distortion from the assumed sinusoidal

profile would introduce unsystematic imbalances in the charge and discharge of the supporting capacitors, which again causes the overall bus voltage ripple to increase.

Therefore, the generated phase-locked signal cannot always be used. Instead, the control ramps can be derived from the backbone capacitor voltage. By passing the AC component of the backbone capacitor voltage through a clamped capacitor circuit, a unipolar control ramp signal from 0V to the peak-to-peak ripple magnitude can be extracted. Similarly, the bipolar control ramp can be created by inverse rectifying the AC component of the backbone capacitor voltage, then processing the resulting signal with a clamped capacitor circuit. This yields a bipolar ramp signal from 0V to the peak ripple amplitude. Alternatively, both control ramp signals can be produced digitally after sampling the backbone capacitor voltage.

Generating the ramp functions directly from the backbone capacitor voltage guarantees zero distortion and phase error between the control signals and the actual ripple cycle. Furthermore, normalization of the sampled signals may not be required because the normalization factor is the inverse of the peak-to-peak ripple amplitude on the backbone capacitor. In practice, implementing control logic with the large voltages may not be feasible. Therefore, resistive dividers can be employed as long as the divider ratio is consistent between the control ramp generation and the supporting capacitor sampling.

3.2.4.4 Pre-charge Circuit Requirement

It is not necessary to have a pre-charge circuit used in [3.47] when using the control strategy described in the previous sections. By adjusting the switch timings, the controller automatically introduces imbalances between the allowable charge and

discharge durations of the supporting capacitors so the capacitor voltages reach their reference.

This is a tradeoff. The pre-charge circuit can facilitate the process of charging the supporting capacitors to their reference levels at startup, which allows the system to reach steady-state operation faster. Secondly, the pre-charge circuit can assist in maintaining the charges on unused capacitors. The proposed controller only controls charge and discharge duration on the active supporting capacitors in the ripple cycle; it has no control over the nonparticipating capacitors in reserve. Thus, having a precharge circuit adds an extra layer of security to ensure that the capacitors in reserve remain ready in the event of a power level increase. Finally, by using a pre-charge circuit to set up all the capacitors to known states initially, the SC energy buffer can in principle be operated without a requirement to monitor the voltage on every supporting capacitor in the buffer.

3.2.4.5 Over- and Under-voltage Protection

Aside from the overvoltage protection circuitry commonly found in PFC and inverter controllers, the SC energy buffer controller can incorporate an additional layer of protection to guard against large transients between sampling periods. Switching duration computations are performed at the beginning of each sampling period. If the transient between sampling periods is large enough, the computed and ideal switch timings may differ significantly, resulting in over- or under-buffering conditions.

"Over-buffering" occurs when the actual ripple magnitude is significantly smaller than the expectation of the controller. When such an event occurs, the boost and drop in the bus voltage from switching the supporting capacitors will be greater than what is

actually needed. Similarly, "under-buffering" occurs when the actual ripple magnitude is significantly larger than the expectation of the controller. Consequently, the boost and drop in the bus voltage from switching the supporting capacitors will be smaller than the required values. Both over- and under-buffering conditions result in larger than expected ripple.

Such undesirable conditions can be avoided by introducing feedforward compensation, i.e., a forced resampling triggered on over- and undervoltage thresholds. Once the bus voltage exceeds the defined thresholds, the controller resamples the current power level and the supporting capacitor voltages to recompute the number of active capacitors required and recalculate the switch timings. In over-buffering conditions, the recomputed number of active capacitors would be decreased, whereas in underbuffering conditions, the recomputed number of active capacitors would be increased.

3.2.5 Simulation Results

The unipolar 1-8 SC energy buffer and the bipolar 1-4 SC energy buffer design examples have been successfully implemented and simulated in SPICE with a 500W inverter. The system is implemented with control ramps generated from the backbone capacitor voltage to avoid distortion and phase errors. In addition, the minimum duration constant k is set to 0.9 and a pre-charge circuit is configured to manage the voltages of supporting capacitors in reserve. The steady-state bus voltage ripple and the backbone capacitor feedback voltage are shown in Fig. 3.26. The simulated result matches the analytical solution quite well. The external inverter control manages the backbone voltage and holds it to 250V. The peak-to-peak ripple is set to 10% by inverting (3.31) and (3.32) and solving for the required capacitance.
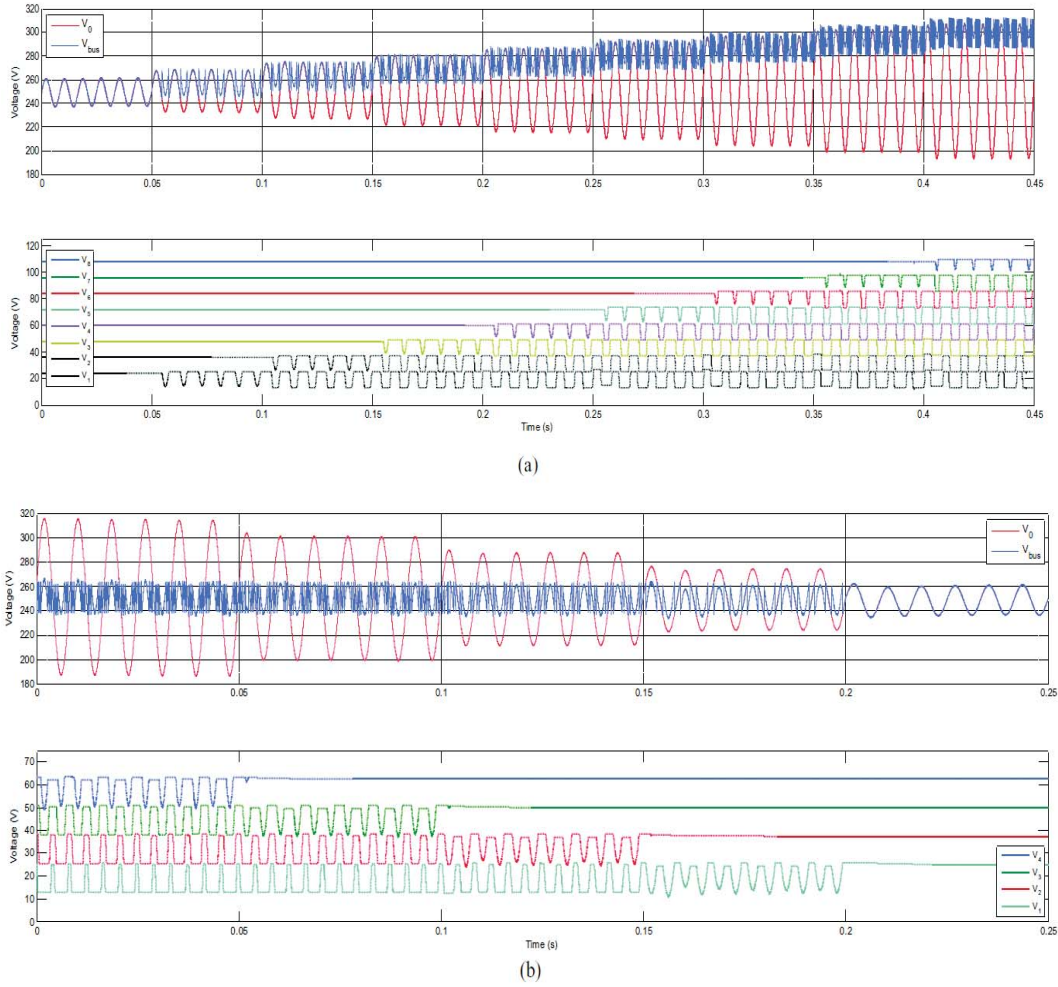
Fig. 3.26 Steady-state bus voltage waveforms of the (a) 1-9 SC energy buffer with unipolar switching experiencing increasing power level and (b) 1-4 bipolar SC energy buffer with bipolar switching experiencing decreasing power level. In (a), the power level increases from 96W to 480W with +48W step size every 50ms. In (b), the power level decreases from 480W to 96W with a -96W step size every 50ms.

The bus voltage in the unipolar switching energy buffer exhibits a power-dependent mean as discussed in Section 3.2.3, and remains well above the grid voltage to retain control. As the power level increases, more supporting capacitors become involved in ripple buffering, as demonstrated by the capacitor activities in the subplot of Fig. 3.26(a). Conversely, the bus voltage in the bipolar switching energy buffer has a constant mean over the all power levels as shown in Fig. 3.26(b). With decreasing

power level, the supporting capacitors sequentially become inactive, leaving only the backbone capacitor to buffer the small power ripple. In a sampled system, the worst-case behavior occurs if a large transient occurs immediately after sampling has taken place.

Thus, this is the case chosen for the transient response characterization. Positive and negative 30% steps in input power level are introduced to the inverter with the bipolar 1-4 SC energy buffer. As shown in Fig. 3.27, the positive step in power causes an underbuffering condition until the bus voltage crosses the upper threshold. Note that the over and undervoltage thresholds are defined to be 1.5 times the ripple specification, i.e. 15% peak-to-peak from 250V, and shown in Fig. 3.27 as dotted lines. At this point, the
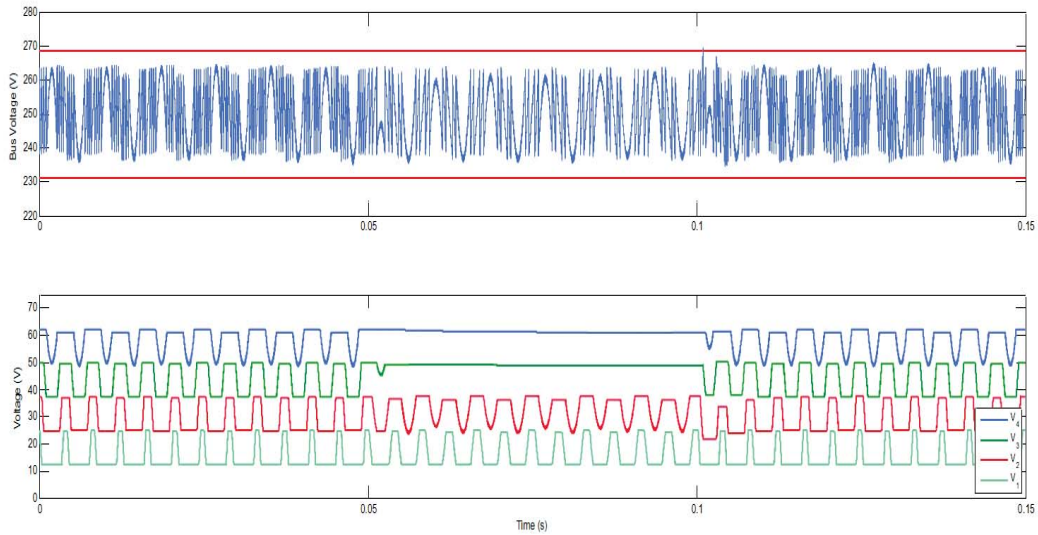
Fig. 3.27 Transient bus voltage response of the example bipolar 1-4 SC energy buffer in a solar inverter due to 30% input power step. The power steps from 480W to 336W at 50ms and back to 480W at 100ms. The second supporting capacitor voltage is shown to deviate from its reference value shortly after 100ms, but the two-step controller brings it back to its reference level in less than 2 ripple cycles.

143

controller immediately resamples and recomputes the switch timings to pull the bus voltage back within bounds. Even though the transient may cause some supporting capacitor voltages, V_2 in this particular example, to deviate from their reference values, the two-step controller is able to bring the system back to steady-state in just a few cycles, without any unacceptably large transient ripple.

3.3 Conclusion

Widespread grid penetration of PV will rely on the reduction of capital cost and total cost of ownership for solar power systems. It is critical that these factors guide the design of photovoltaic power circuits and system architectures. This work has presented a full system approach utilizing switched capacitor multilevel DC-DC converters. Substantial cost reductions may be possible by providing per panel MPPT without the need for per panel magnetics. Coupling the DC-DC modules with a ripple port inverter eliminates the need for electrolytic capacitors, enabling long-life operation.

Topics of ongoing research include investigation of MPPT algorithms and related system level tradeoffs for control of the central inverter. There exist necessary tradeoffs among switching frequency, converter efficiency, and global tracking efficiency (Io step size) when considering the dynamics and runtime MPPT approaches for the full system. Not addressed in this work was the dual case of paralleled strings of panels. This will also be a topic of ongoing investigation.

Switched-capacitor energy buffers have been shown to achieve much better energy utilization than their single electrolytic counterparts. However, overshooting and the possibility of losing control to the grid are major concerns. The proposed control strategy can potentially minimize the possibility of such undesirable behaviors by

maintaining an appropriate number of supporting capacitors in reserve to guard against sudden transients in power level.

Two SC energy buffers – 1-8 with unipolar switching and 1-4 with bipolar switching – have been examined in a 500W inverter. The simulated models show excellent agreement with the calculated results. Furthermore, the system is able to maintain a minimum bus voltage of 250V and limit the peak-to-peak ripple to 10% under steady-state operation . It is also shown that the new control strategy can successfully maintain the ripple specification under significant power level transients.

References

[3.1] P. Krein and R. Balog, "Cost-effective hundred-year life for single-phase inverters and rectifiers in solar and led lighting applications based on minimum capacitance requirements and a ripple power port," in *Applied Power Electronics Conference and Exposition, 2009. APEC 2009. Twenty-Fourth Annual IEEE*, feb 2009, pp. 620 –625.

[3.2] P. T. Krein, "Power electronics needs and performance analysis for achieving grid parity solar energy costs," power point presentation.

[3.3] R. W. Erickson, "Future of power electronics for photovoltaics," power point presentation.

[3.4] J. K. Mapel, "Organic photovoltaics and concentrators," Ph.D. dissertation, Massachusetts Institute of Technology,, 2006.

[3.5] T. Esram, J. Kimball, P. Krein, P. Chapman, and P. Midya, "Dynamic maximum power point tracking of photovoltaic arrays using ripple correlation control," *Power Electronics, IEEE Transactions on*, vol. 21, no. 5, pp. 1282 –1291, sept 2006.

[3.6] R. Faranda, S. Leva, and V. Maugeri, "Mppt techniques for pv systems: Energetic and cost comparison," in *Power and Energy Society General Meeting - Conversion and Delivery of Electrical Energy in the 21st Century, 2008 IEEE*, july 2008, pp. 1 –6.

[3.7] L. Linares, R. Erickson, S. MacAlpine, and M. Brandemuehl, "Improved energy capture in series string photovoltaics via smart distributed power electronics," in *Applied Power Electronics Conference and Exposition, 2009. APEC 2009. Twenty-Fourth Annual IEEE*, feb 2009, pp. 904 –910.

[3.8] G. Walker and P. Sernia, "Cascaded dc-dc converter connection of photovoltaic modules," *Power Electronics, IEEE Transactions on*, vol. 19, no. 4, pp.1130 – 1139, july 2004.

[3.9] H. Patel and V. Agarwal, "Mppt scheme for a pv-fed single-phase single-stage grid-connected inverter operating in ccm with only one current sensor,"*Energy Conversion, IEEE Transactions on*, vol. 24, no. 1, pp. 256 –263, march 2009.

[3.10] B. Sahan, A. Vergara, N. Henze, A. Engler, and P. Zacharias, "A single-stage pv module integrated converter based on a low-power current-source inverter," *Industrial Electronics, IEEE Transactions on*, vol. 55, no. 7, pp. 2602 –2609, july 2008.

[3.11] W. Xiao, N. Ozog, and W. Dunford, "Topology study of photovoltaic interface for maximum power point tracking," *Industrial Electronics, IEEE Transactions on*, vol. 54, no. 3, pp. 1696 –1704, june 2007.

[3.12] F. Filho, Y. Cao, and L. Tolbert, "11-level cascaded h-bridge grid-tied inverter interface with solar panels," in *Applied Power Electronics Conference and Exposition (APEC), 2010 Twenty-Fifth Annual IEEE*, feb 2010, pp. 968 –972.

[3.13] S. Kouro, B. Wu, A. Moya, E. Villanueva, P. Correa, and J. Rodriguez, "Control of a cascaded h-bridge multilevel converter for grid connection of photovoltaic systems," in *Industrial Electronics, 2009. IECON '09. 35th Annual Conference of IEEE*, nov 2009, pp. 3976 –3982.

[3.14] E. Ozdemir, S. Ozdemir, and L. Tolbert, "Fundamental-frequency-modulated six-level diode-clamped multilevel inverter for three-phase stand-alone photovoltaic system," *Industrial Electronics, IEEE Transactions on*, vol. 56, no. 11, pp. 4407 –4415, nov 2009.

[3.15] M. Mousa, M. Ahmed, and M. Orabi, "New converter circuitry for pv applications using multilevel converters," in *Telecommunications Energy Conference, 2009. INTELEC 2009. 31st International*, oct 2009, pp. 1 –6.

[3.16] P. Krein and Kim, "Pv converter module configurations for mppt operation," *PECI*, 2010.

[3.17] M. Seeman, V. Ng, H.-P. Le, M. John, E. Alon, and S. Sanders, "A comparative analysis of switched-capacitor and inductor-based dc-dc conversion technologies," in *Control and Modeling for Power Electronics (COMPEL), 2010 IEEE 12th Workshop on*, june 2010, pp. 1 –7.

[3.18] E. Roman, R. Alonso, P. Ibanez, S. Elorduizapatarietxe, and D. Goitia, "Intelligent pv module for grid-connected pv systems," *Industrial Electronics, IEEE Transactions on*, vol. 53, no. 4, pp. 1066 –1073, june 2006.

[3.19] G. Walker and J. Pierce, "Photovoltaic dc-dc module integrated converter for novel cascaded and bypass grid connection topologies 8212; design and optimisation," in *Power Electronics Specialists Conference, 2006. PESC '06. 37th IEEE*, june 2006, pp. 1 – 7.

[3.20] W.-Y. Choi, S.-M. Kim, S.-J. Park, K.-H. Kim, and Y.-C. Lim, "High step-up dc-dc converter with high efficiency for photovoltaic module integrated converter systems," in *Telecommunications Energy Conference, 2009. INTELEC 2009. 31st International*, oct 2009, pp. 1 –4.

[3.21] B. Yuan, X. Yang and D. Li, "Analysis and design of a high efficiency current fed multi-resonant converter for high step-up power conversion in renewable energy harvesting," in *Power Electronics for Distributed Generation Systems (PEDG), 2010 2nd IEEE International Symposium on*, june 2010, pp. 138 –143.

[3.22] J. Enslin, M. Wolf, D. Snyman, and W. Swiegers, "Integrated photovoltaic maximum power point tracking converter," *Industrial Electronics, IEEE Transactions on*, vol. 44, no. 6, pp. 769 –773, Dec. 1997.

[3.23] J.-M. Kwon, B.-H. Kwon, and K.-H. Nam, "Three-phase photovoltaic system with three-level boosting mppt control," *Power Electronics, IEEE Transactions on*, vol. 23, no. 5, pp. 2319 –2327, sept 2008.

[3.24] D. Hohm and M. Ropp, "Comparative study of maximum power point tracking algorithms using an experimental, programmable, maximum power point tracking test bed," in *Photovoltaic Specialists Conference, 2000. Conference Record of the Twenty-Eighth IEEE*, Jan. 2000, pp. 1699 –1702.

[3.25] Y. Bo, Y. Xu, and L. Donghao, "Application of power compensating concept for high efficiency maximum power point tracking in grid-connected photovoltaic system," in *Power Electronics Conference (IPEC), 2010 International*, june 2010, pp. 938 –941.

[3.26] C. Sullivan and M. Powers, "A high-efficiency maximum power point tracker for photovoltaic arrays in a solar-powered race vehicle," in *Power Electronics Specialists Conference, 1993. PESC '93 Record., 24th Annual IEEE*, Jun. 1993, pp. 574 –580.

[3.27] J. Lopez-Seguel, S. Seleme, P. Donoso-Garcia, L. Morais, P. Cortizo, and M. Mendes, "Comparison of mppt approaches in autonomous photovoltaic energy supply system using dsp," in *Industrial Technology (ICIT), 2010 IEEE International Conference on*, march 2010, pp. 1149 –1154.

[3.28] M. E. Corp., "Mitsubishi electric photovoltaic module pv-mf170eb4 170wp," Datasheet, June 2006.

[3.29] J. Martynaitis, "Discussion of "theoretical and experimental analyses of photovoltaic systems with voltage and current-based maximum power point tracking"," *Energy Conversion, IEEE Transactions on*, vol. 19, no. 3, p. 652, sept. 2004.

[3.30] H. Matsuo and F. Kurokawa, "New solar cell power supply system using a boost type bidirectinal dc-dc converter," *Industrial Electronics, IEEE Transactions on*, vol. IE-31, no. 1, pp. 51 –55, feb. 1984.

[3.31] T. Noguchi, S. Togashi, and R. Nakamoto, "Short-current pulse based adaptive maximum-power-point tracking for photovoltaic power generation system," in *Industrial Electronics, 2000. ISIE 2000. Proceedings of the 2000 IEEE International Symposium on*, vol. 1, jan 2000, pp. 157 –162 vol.1.

[3.32] C. Yu-yun and M. Yong-kui, "Constant current-based maximum-power-point tracking for photovoltaic power systems," in *Control and Decision Conference, 2009. CCDC '09. Chinese*, june 2009, pp. 3422 –3425.

[3.33] S. Yuvarajan and J. Shoeb, "A fast and accurate maximum power point tracker for pv systems," in *Applied Power Electronics Conference and Exposition, 2008. APEC 2008. Twenty-Third Annual IEEE*, feb. 2008, pp. 167 –172.

[3.34] M. Seeman and S. Sanders, "Analysis and optimization of switched-capacitor dc x2013;dc converters," *Power Electronics, IEEE Transactions on*, vol. 23, no. 2, pp. 841 –851, march 2008.

[3.35] I. Rectifier, "Irl3714z hexfet power mosfet," Datasheet, 2004.

[3.36] R. Ram, "Power electronics," ARPA-E Pre Summit Seminar, March 2010.

[3.37] P. Krein and T. Esram, "Admittance control for anti-islanding protection in modular grid-connected inverters," in *Control and Modeling for Power Electronics (COMPEL), 2010 IEEE 12th Workshop on*, june 2010, pp. 1 –5.

[3.38] I. Rectifier, "An-978 hv floating mos-gate driver ics," Application Note.

[3.39] M. S. Inc., "Switchmode power rectifiers mbr20100c," Datasheet, 1996.

[3.40] J. Kassakian, M. Schlecht, and G. Verghese, *Principles of Power Electronics*. Adison-Wesley Publishing Co., 1992

[3.41] Krein, P.T.; Balog, R.S.; , "Cost-Effective Hundred-Year Life for Single-Phase Inverters and Rectifiers in Solar and LED Lighting Applications Based on Minimum Capacitance Requirements and a Ripple Power Port," *Applied Power Electronics Conference and Exposition, 2009. APEC 2009. Twenty-Fourth Annual IEEE* , vol., no., pp.620-625, 15-19 Feb. 2009

[3.42] Kyritsis, A.C.; Papanikolaou, N.P.; Tatakis, E.C.; , "Enhanced Current Pulsation Smoothing Parallel Active Filter for single stage grid-connected AC-PV modules," *Power Electronics and Motion Control Conference, 2008. EPE-PEMC 2008. 13th* , vol., no., pp.1287-1292, 1-3 Sept. 2008

[3.43] Shimizu, T.; Jin, Y.; Kimura, G.; , "DC ripple current reduction on a single-phase PWM voltage-source rectifier," *Industry Applications, IEEE Transactions on* , vol.36, no.5, pp.1419-1429, Sep/Oct 2000

[3.44] Pierquet, B.J.; Perreault, D.J.; , "A single-phase photovoltaic inverter topology with a series-connected power buffer," *Energy Conversion Congress and Exposition (ECCE), 2010 IEEE* , vol., no., pp.2811-2818, 12-16 Sept. 2010.

[3.45] Bush, C.R.; Wang, B.; , "A single-phase current source solar inverter with reduced-size DC link," *Energy Conversion Congress and Exposition, 2009. ECCE 2009. IEEE* , vol., no., pp.54-59, 20-24 Sept. 2009

[3.46] Chang, A.H.; Cooley, J.J.; Leeb, S.B.; , "A systems approach to photovoltaic energy extraction," *Applied Power Electronics Conference and Exposition (APEC), 2012 Twenty-Seventh Annual IEEE* , vol., no., pp.59-70, 5-9 Feb. 2012

[3.47] Minjie Chen; Afridi, K.K.; Perreault, D.J.; , "Stacked switched capacitor energy buffer architecture," *Applied Power Electronics Conference and Exposition (APEC), 2012 Twenty-Seventh Annual IEEE* , vol., no., pp.1404-1413, 5-9 Feb. 2012.

[3.48] Linear Technology, "LT1249 – Power Factor Controller," Datasheet

Chapter 4

Maximum Power Point Tracking of PV Arrays in Kuwait

4.1 Introduction

One of the available technologies to generate electricity from renewable resources is to use solar cells to convert the energy delivered by the solar irradiance into electricity. Currently, PV energy generation has a great commercial and academic interest. Recent studies indicate that in the medium to longer term PV generation may become technically and commercially worldwide feasible to be implemented for electricity generation. The main purpose of this report is to study the performance of PV arrays under varying weather conditions in Kuwait. For this study a data base of hourly solar radiation and temperature are collected for a period of six years.

The grid connected PV system converts sunlight directly into ac electricity to supply local loads and inject the excess energy to the public grid. The main purpose of the system is to reduce the electrical energy imported from the electric network. Fig. 4.1 shows the block diagram of the basic components for a grid-connection of PV system. The dc output of the PV array is converted into ac and injected into the grid through an interfacing inverter. The controller of this system implements all the main regulation and protection functions such as:- Maximum Power Point Tracking (MPPT), protection relay and detection of islanding operation.
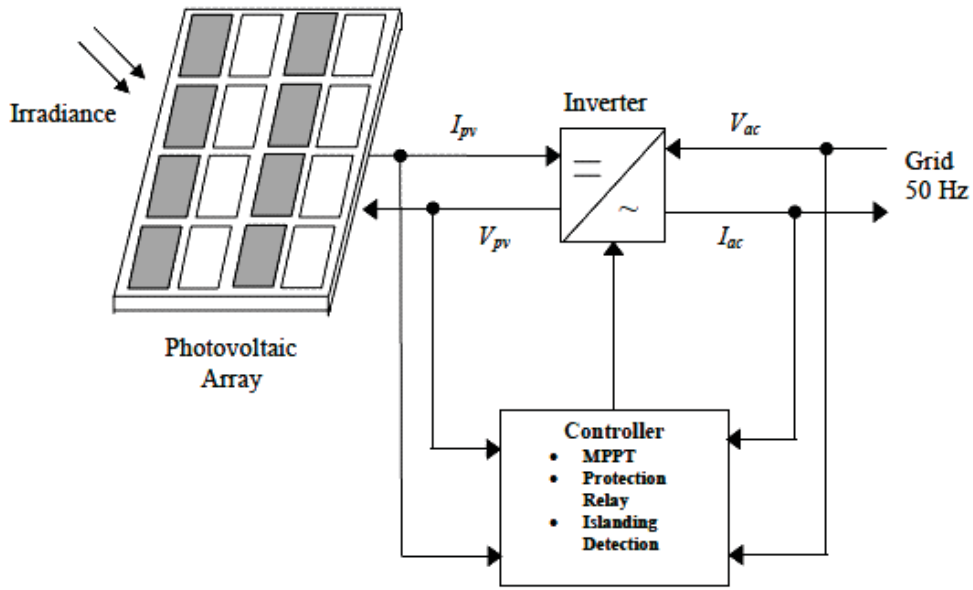
Fig. 4.1 Basic components of grid connected PV array

4.2 Maximum Power Point

Under constant irradiance and cell temperature, the operating point of a PV array is determined by the intersection of the I_{pv}-V_{pv} characteristic and the load line as shown in Fig. 4.2. The load characteristic is defined by a straight line with a gradient given by I_{Load}/V_{Load}. The system operating point moves along the I_{pv}-V_{pv} characteristic curve of the PV panel from B to A as the load resistance increase from zero to infinity. Position C is the maximum power operating point. If the load resistance is too high, the operating points would be in the CA regions. If the load resistance is too low, the operating points would be in the CB regions. Therefore, the maximum power point can be obtained by matching the load resistance to the PV array characteristics.
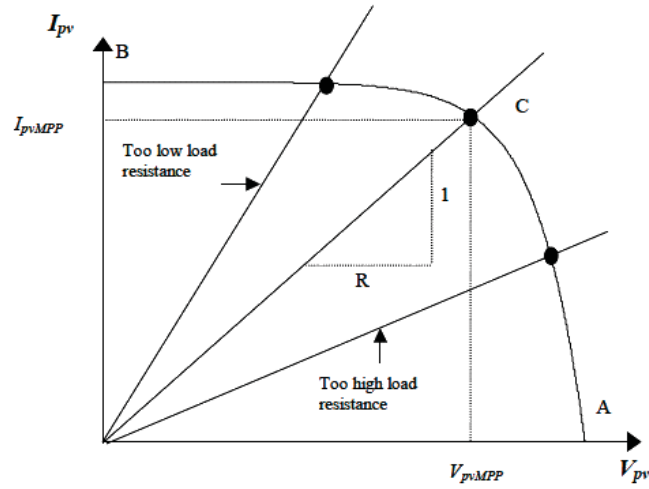
Fig. 4.2 PV characteristic curve and load line

4.3 Effect of Irradiance and Cell Temperature

The effect of irradiance and cell temperature on I_{pv}-V_{pv} characteristic curve is shown in Figs. 4.3 and 4.4, respectively. Fig. 4.3 indicates that the maximum power output is directly proportional to the irradiance. On the other side, Fig. 4.4 shows that the maximum output power from the array decreases as the temperature increases.

As illustrated, the I_{pv}-V_{pv} characteristic of a PV cell varies with the irradiance and operating temperature of the cell. The temperature of the panel, or more precisely the diode junction temperature, also affects the voltage-current curve of the panel. This effect can be taken into a consideration by using temperature coefficients. The typical values of the coefficient for silicon and germanium diodes are:

$$\frac{dV}{dT} = -2.3 ..... -2.1 mV \ /^{\circ}C \tag{1.1}$$

It should be noted that these coefficients are negative. This means the higher the temperature, the lower the open-circuit voltage. The voltage-dependency can be considered linear. Thereby, the voltage vs. temperature variation could be represented as
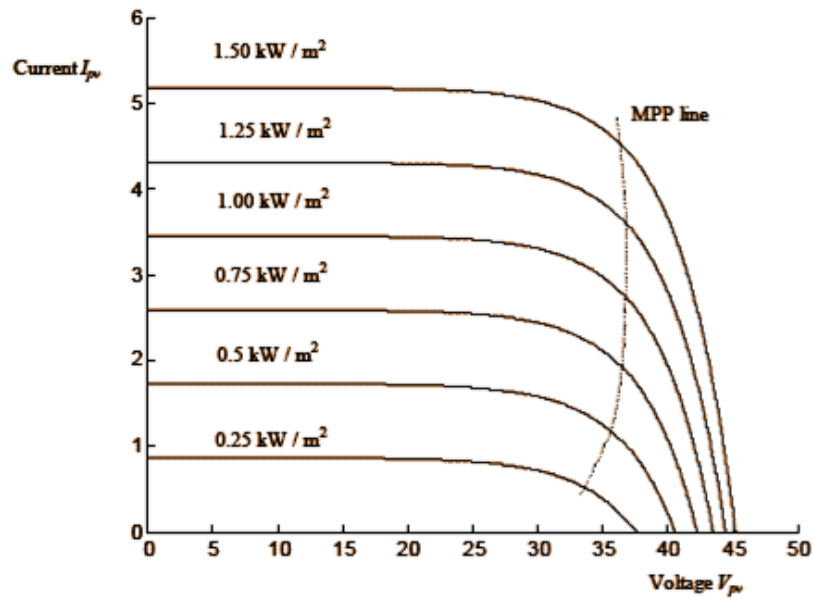
151

Fig. 4.3 Effect of irradiance on the maximum power at constant cell temperature
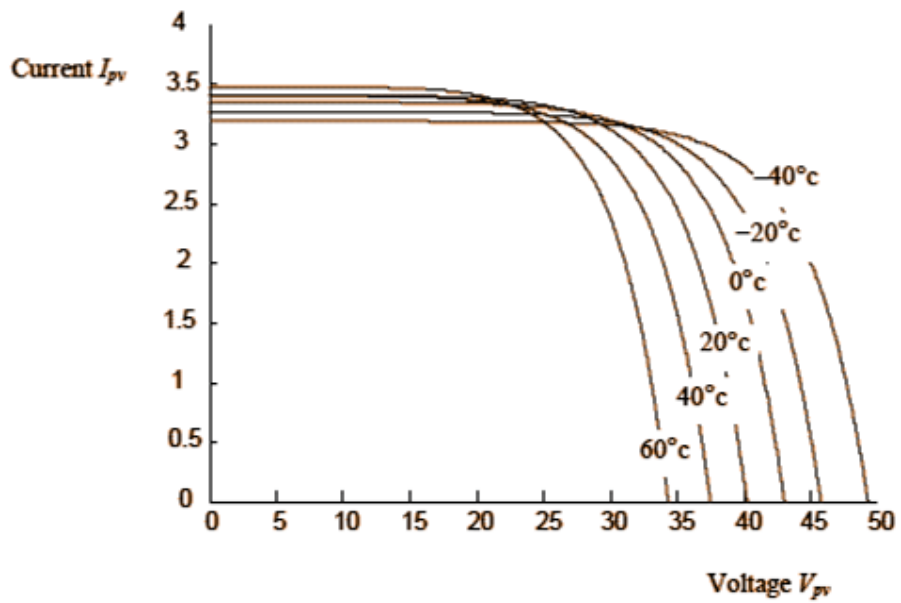

Fig. 4.4 Effect of temperature on the cell characteristic at constant irradiance

percentage coefficients. Hence, these coefficients provide the percentage voltage variations with the temperature changes. These coefficients stay the same regardless of the amount of panels connected in series. The voltage as a function of temperature can thus be found according to:

$$V(T) = V_o[1 + (T - T_o)K_V]$$ (1.2)

where

$$K_V = \frac{dV}{dT} \times 100\%$$ (1.3)

The value K_V can be found on most PV-panel data-sheets [4.1, 4.2].

A previous study was carried by T. Nordmann and L. Clavadetscher to define the effect of solar radiation on the panel temperature in different kinds of installations [4.1, 4.3]. According to this study, the temperature of the panel may rise between 20°C and 55°C above ambient per kW/m^2 of insolation. This means that the panel temperature will be between 45 °C and 80 °C on a 25 °C day at 1000 W/m^2 solar irradiation.

As a result, the environmental factors clearly have a large effect on solar panel behavior. This is why panel specifications are given in standardized conditions. Two sets of environmental parameters have been standardized in IEC 60904-3. Standard test conditions (STC) are defined so that panel temperature is 25 °C, insolation is 1000 W/m^2, and ambient temperature is not defined. Normal operating conditions (NOC) are defined so that ambient temperature is 20 °C, wind speed is 1m/s, and insolation is 800 W/m2 [4.3, 4.4].

The power produced by the panel is calculated as the product of voltage and current. That means this power changes as a function of voltage and hence a clear maximum value can be produced at certain output voltage. This maximum is defined as the MPP of the panel. The voltage and current of the panel at this point are usually given in the

153

data-sheets of solar panels. This point, however, does not stay constant. This is attributed to the fact that the voltage and current change as a function of both insolation and temperature. As described above, insolation mostly affects current and temperature mostly affects voltage.

Since the MPP does not remain constant in the changing operating conditions of a solar panel. Therefore, the power converter used to extract power from the PV-module should have some means of control to track the required MPP. This control is referred to as maximum power point tracking (MPPT). A directly connected fixed load resistance cannot extract maximum power from the PV system under varying radiation and temperature conditions. To get maximum power output at all time, the PV array should track the varying MPP. Therefore, a controller capable of tracking the maximum power point must be implemented to regulate the interfaced converter.

There are a number of Maximum Power Point Tracking (MPPT) techniques. All of these methods require dedicated algorithm to specify the location of the operating point with respect to the maximum power point. In some cases, these algorithms can deliver sub-optimum power output depending on the step size of updating panel voltage. A good MPPT technique should accurately track the maximum power to reduce the cost/kWh generated by the panel.

4.4 Power Conditioning Devices

The tracking of maximum power can be achieved by introducing a DC/DC converter to adjust the panel voltage properly. The control section consists of two control loops: one for the input and the other for the output. The PV generator voltage is regulated at the required level by suitable adjustment of the DC/DC converter. In one of studied

algorithm the voltage level can be kept constant (CV algorithm) or can track the actual MPP by an appropriate searching techniques (MPPT) [4.5].

The practical way to connect PV-array to the AC-grid is to connect some panels in series and use a DC-boost converter to boost the voltage for the inverter as shown in Fig. 4.5. By this way the boost converter ensures that the panel system is at its MPP and that the inverter is fed with the appropriate voltage level of the grid. Still, enough panels should be connected in series to improve the efficiency of the boost conversion as high as possible [4.8].

This dual device configuration has some advantages over single stage inverter. Mainly, a high enough DC-voltage can be produced for the inverter to function at the MPP of the installation with high efficiency and good power quality. This can be done without exceeding the voltage limits at the terminals of the panel installation in case of single stage inverter [4.8-4.10].
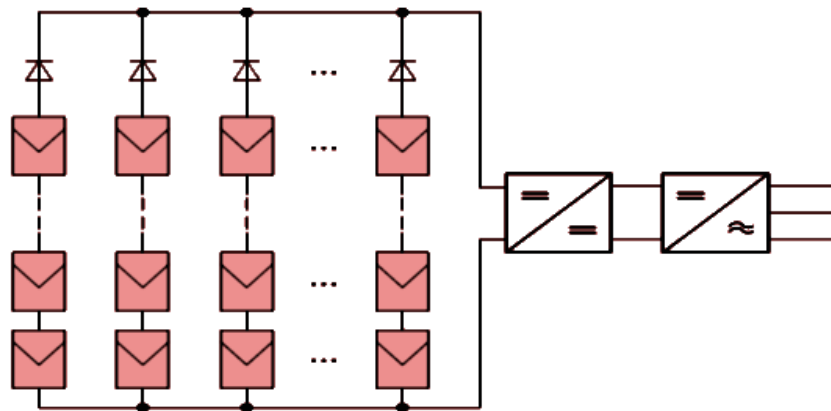
Fig. 4.5 A PV-array with central boost converter and inverter

4.5 Power Electronics Devices for PV arrays

From the discussion in the previous subsection, it can be observed that the most important power electronics device for the PV application is the DC-DC converter and the DC-AC inverter as shown in Fig. 4.6. In general, the MPPT and voltage boost are done by the DC-DC converter controller. The power flow control to the utility and the sinusoidal unity power factor current-injection is achieved by the DC-AC inverter controller [4.11-4.13].

The use of boost converters also allows for greater modularity: several boost converters can be used to feed one inverter. If MPP-tracking is implemented in the boost converters rather than the inverter, fewer panels will be tracked by each converter leading to more precise tracking. A diagram of an installation with string boost converters is presented in Fig. 4.6.

Partial shading or dirt problems can have a significant effect on energy harvesting in large installations. If the boost converters are positioned close to the panels, transmission lines can also be made with high voltages, which reduce losses from cable
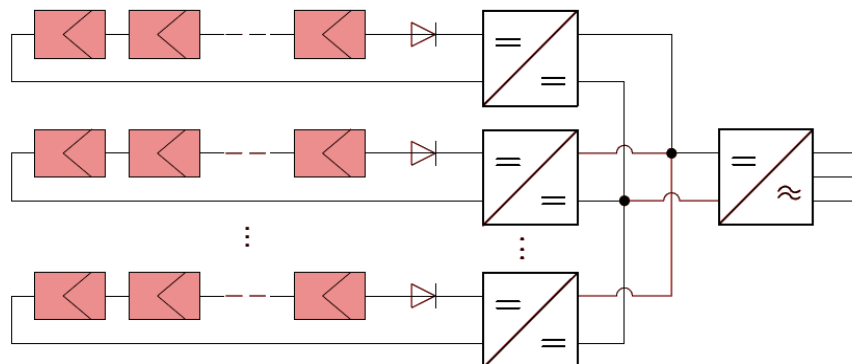

Fig. 4.6 PV-array with string boost converters

resistance. On the other side, the DC-boost converters will introduce additional losses by an added converter stage. Previous measurements [4.9] showed that the efficiencies of the converter reached a value of 97% for a 100kW boost converter.

However, market leaders in solar inverter technology are claiming 98% efficiencies for whole inverter systems [4.10].

4.6 Boost Converter

As previously stated, the maximum power point tracking is basically a load matching problem. In order to change the input resistance of the panel to match the load resistance (by varying the duty cycle), a DC to DC converter is required. The efficiency of the DC to DC converter is maximum for a buck converter, then for a buck-boost converter and minimum for a boost converter. However, the grid connected PV array and pumping system require higher voltage that produced by the array. Therefore, the boost converter is used to obtain the suitable voltage level as shown in Fig. 4.7.
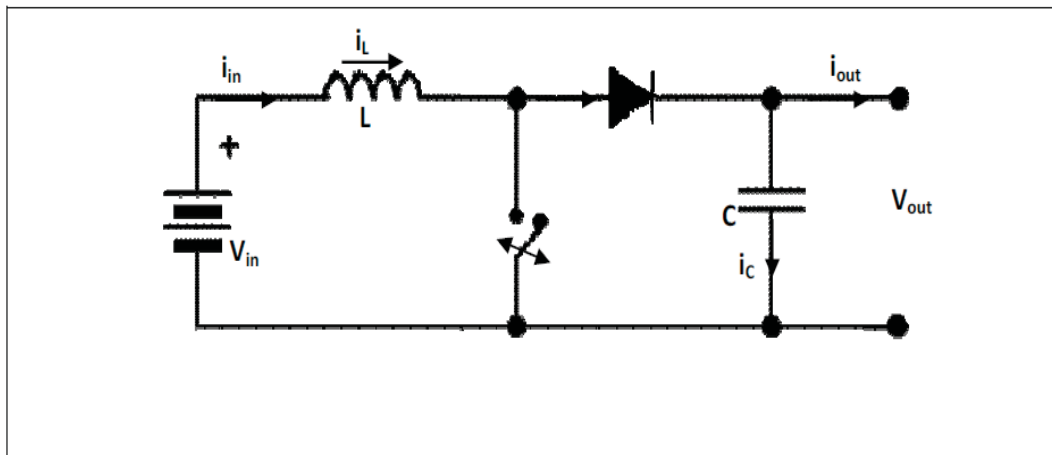
Fig. 4.7 Circuit diagram of a Boost Converter

4.6.1 Mode 1 of the Boost Converter Operation

When the switch is closed the inductor gets charged through the input DC voltage and stores the energy. In this mode inductor current rises (exponentially) but for simplicity we assume that the charging and the discharging of the inductor are linear. The diode blocks the current flowing and so the load current remains constant which is being supplied due to the discharging of the capacitor.
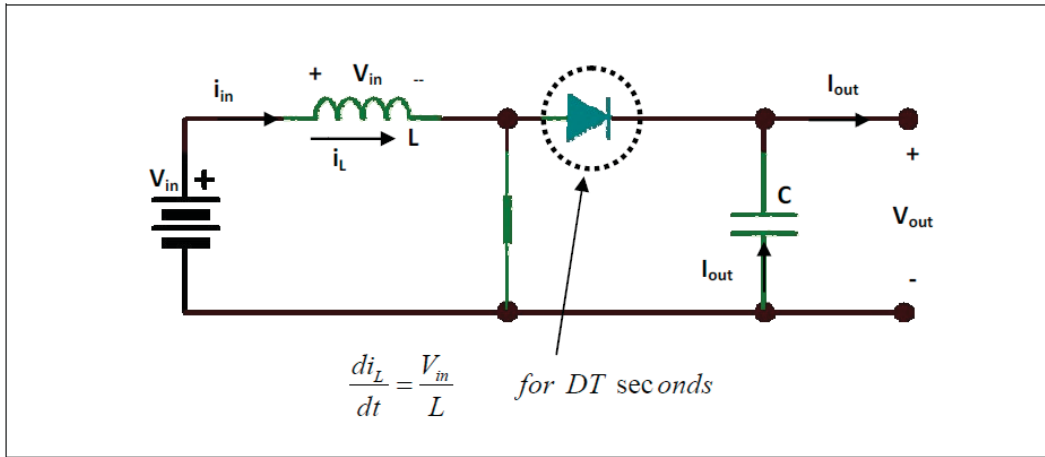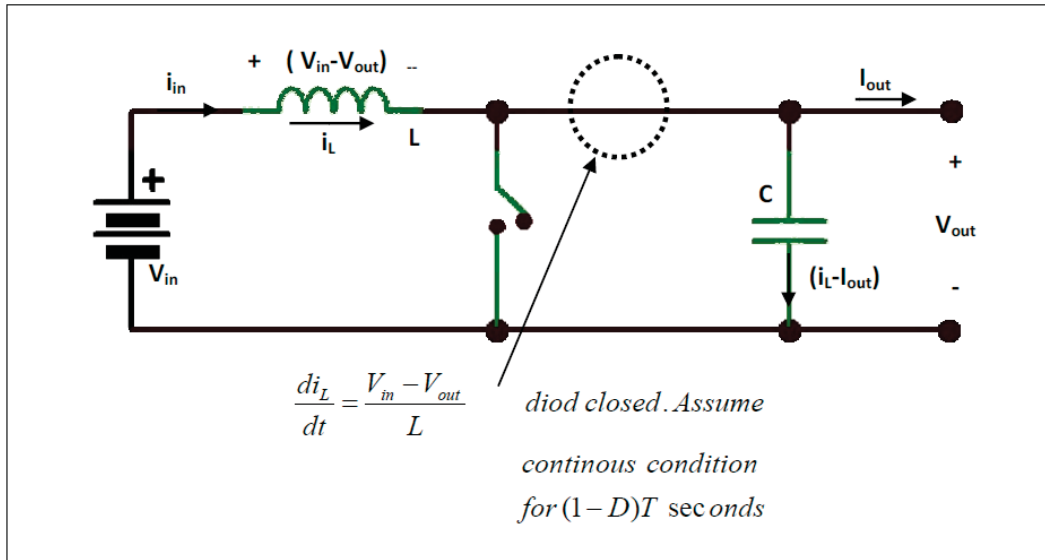

Fig. 4.8 Mode 1 operation of Boost Converter

4.6.2 Mode 2 of the Boost Converter Operation

In mode 2 the switch is open and so the diode becomes short circuited as shown in Fig. 4.9. The energy stored in the inductor gets discharged through opposite polarities which charge the capacitor. The load current remains constant throughout the operation. The equivalent load resistance seen by the PV-panel is illustrated in Fig. 4.10.

$$V_{Lavg} = D \times V_{in} + (1-D) \times (V_{in} - V_{out}) = 0 \tag{1.4}$$

$$V_{out} = \frac{V_{in}}{1-D} \tag{1.5}$$

$$\frac{di_L}{dt} = \frac{V_{in} - V_{out}}{L}$$

diod closed. Assume

continous condition

for $(1-D)T$ *sec onds*

Fig. 4.9 Mode 2 operation of Boost Converter

$$R_{equiv} = \frac{V_{in}}{I_{in}} = \frac{(1-D)V_{out}}{\dfrac{I_{out}}{1-D}} = (1-D)^2 \frac{V_{out}}{I_{out}} = (1-D)^2 R_{load}$$
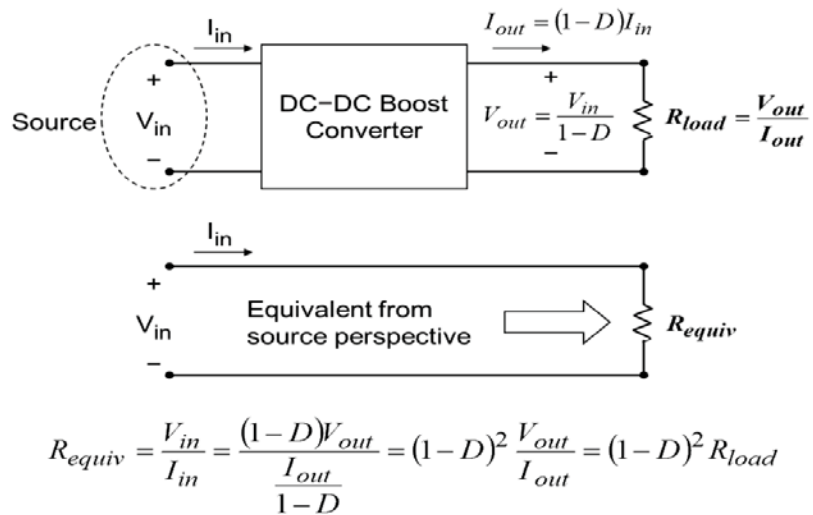
Fig. 4.10 The relation between the equivalent load resistance and the duty cycle

To extract maximum power (130W), connect a boost converter between the panel and the load resistor. By using D the equivalent load resistance is modified so that its seen value from the panel corresponds to the maximum power.

$$R_{equiv} = (1-D)^2 R_{load}, D = 1 - \sqrt{\frac{R_{equiv}}{R_{load}}} = 1 - \sqrt{\frac{6.44}{100}} = 0.75$$
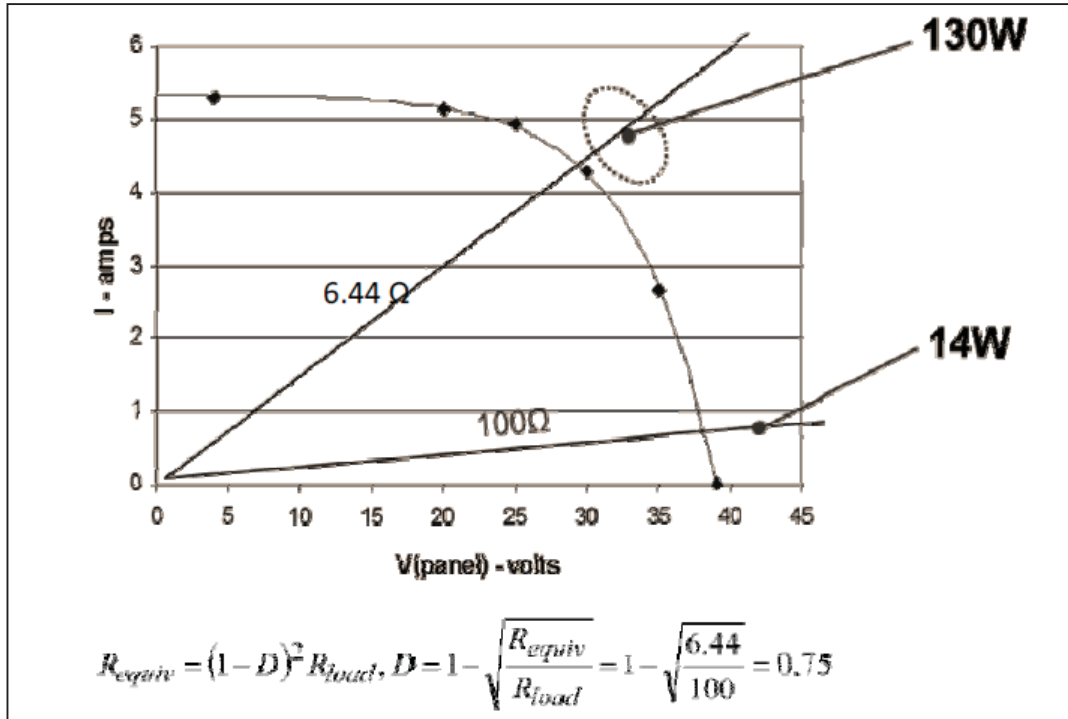
Fig. 4.11 Tracking the maximum power by changing the duty cycle

The selection of the switching devices depends mainly on the operating voltage and current of the semiconductors to be used in the power converter, as shown in Fig. 4.12. For low power and low voltage applications, MOSFET represents the most appropriate switching devices. The MOSFET has very low conducting losses which results in high switching efficiency. Additionally, it has a parasitic anti-parallel diode that can be used as a freewheel-diode. With higher voltage and current rating MOSFET would be replaced by IGBT and then GTO-SCR [4.11, 4.12].
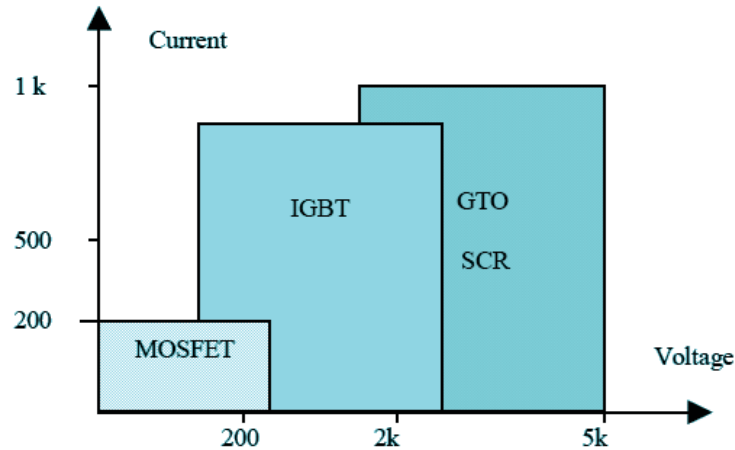
Fig. 4.12 Voltage and current rating of switching devices

Other important design parameters are inductance and capacitance. The main purpose of the capacitance in the DC-link is to keep the input voltage to the inverter at constant value. Its size is determined so that the voltage ripples are restricted within the pre-specified limits. The capacitor must also be able to carry a fairly high current, roughly 1.5-2 times the mean DC current [4.13, 4.14].

The selection of the series inductance depends mainly on the required power quality and efficiency. The magnetic material together and the value of the flux density determine the iron losses. If the switching frequency is increased, the ripple losses will normally decrease. On the other side the switching losses in the transistors will increase. In fact a high inductance will reduce the ripple current and, consequently decrease the ripple losses but will, on the other hand, increase copper losses and, consequently, increase the weight and cost of the inductance.

Electrolytic capacitors will be avoided in this project due to their relatively low lifetime especially at high temperature operation. The integrated converters must, ideally, operate for the same lifetime as the PV modules. Therefore, ceramic components will be

used. Capacitors were chosen based on the required capacitance value, voltage and RMS current ratings, and temperature derating of the dielectric [4.13, 4.14]

4.7 DC-DC Converter Models

The DC-DC converter model mainly attempts to correlate the input and output loads. The output load defines the downstream loading seen by the converter. On the other hand, the input load represents the upstream loading that the converter places on the PV arrays. The output voltage is kept constant as possible. Other dominant variables include output current and voltage range.

For larger grid connected PV-arrays with a capacity over 10kW, three-phase inverters are required. All the configurations described for single-phase utility connection can be used for the three phase. Again, the isolation from the grid can be done either by using a line-frequency or a high-frequency transformer. In such case, an additional converter is required for converting the produced DC voltage from PV array into the AC frequency of the grid.

The DC output of the array is connected across a DC-Link capacitor to a voltage-source three-phase inverter. The output of each phase of the converters is connected to an inductor and capacitor to limit the high-frequency harmonics injected into the grid. A synthesized AC output voltage is produced by appropriately controlling the inverter switches. A three-phase transformer is then used to connect the power to the utility.

4.8 Maximum Power Point Tracking Algorithms

The general block diagram of Maximum power Point Tracking algorithms for the PV array is given in Fig. 4.13. The basic concept of MPPT depends mainly on the applied control technique to move the operating point toward the maximum power [4.15-4.19].
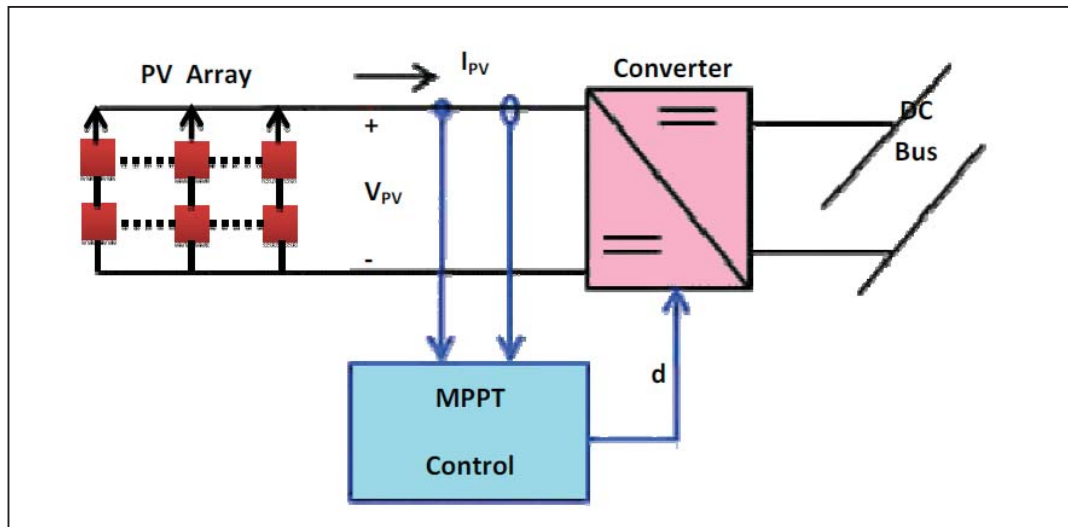

Fig. 4.13 Concept of maximum power point tracking

The MPPT concepts can be classified into two groups as follows:

Indirect MPP trackers:

This type of MPP tracker estimates the MPP voltage by means of simple measurements.

1. The operating voltage of the solar generator can be adjusted seasonally. Higher MPP voltages can be expected in winter because of lower cell temperatures.

2. The operating voltage can be adjusted according to the module temperature.

3. The operating voltage can be derived from the instantaneous open-circuit voltage by multiplication with a constant factor, for example, 0.8 for crystalline silicon solar cells.

These indirect MPP trackers results in an approximate but in many cases acceptable optimum operation point and defined as Constant Voltage algorithms.

Direct MPP trackers

In these trackers, the optimum operating voltage is determined from measured currents, voltages or the actual power produced by the PV array. Therefore, they are able to respond to quick environmental changes. These algorithms are defined as Incremental Conductance trackers. In other direct trackers, the operating voltage is periodically changed in small steps until the maximum power is approached. The increment can either be constant or can be updated when searching the optimal operating point. If the module's power increases from one step to the next, the search direction is retained: otherwise it is reversed. In this way, the MPP is found and the operating point oscillates around the actual MPP. These trackers are defined as Perturb and Observe algorithms [4.17-4.20]

Table 4.1 summarized the above mentioned MPP tracking algorithms studied in this report according to the local environmental conditions in Kuwait.

Table 4.1 Maximum power point tracking algorithms

Indirect	Direct
Constant Voltage	Incremental Conductance
	Perturb and Observe

4.8.1 Constant Voltage Algorithm

This simple and robust method depends mainly on the Open Circuit Voltage of the relay as dominant parameter for tracking the maximum power point. The ratio V_{mpp}/V_{oc} is usually kept constant by using this algorithm [4.21]. This method was proposed because the maximum power point Voltage does not change so much with radiation variations. The operating point of the PV array is kept near the MPP by regulating the array voltage and matching it to a fixed reference voltage $V_{ref.}$ The V_{ref} value is set equal to the V_{MPP} of the PV module. This method assumes that individual insulation and temperature variations on the array are insignificant, and that the constant reference voltage is an adequate approximation of the true MPP. This means that CV algorithm is based on approximately constant ratio between V_{MPP} and V_{oc} as given in (4.6):

$$V_{MPP} \cong kV_{oc} \tag{1.6}$$

By the adjusting of array voltage to this calculated value, the operation at MPP is achieved. In literature, K value ranges between 73% and 80% [4.22-4.25]. The measurement of the voltage V_{PV} is necessary in order to set up the duty-cycle of the DC/DC converter. After determining the value for V_{MPP}, the DC/DC boost converter is switched to quickly force the array terminal voltage to its MPP value. The difference between MPP fraction voltage and the array output represents the error of the PID controller in Fig. 4.14. This PID controller regulates the PV array voltage by continuously switching on and off of the IGBTs at high frequency according to the varying duty cycle. The fast switching action of the boost converter decouples the dynamics of the PV array due its changes in voltage or current from that of the DC link capacitor, which offers good performance under changing weather conditions. The other
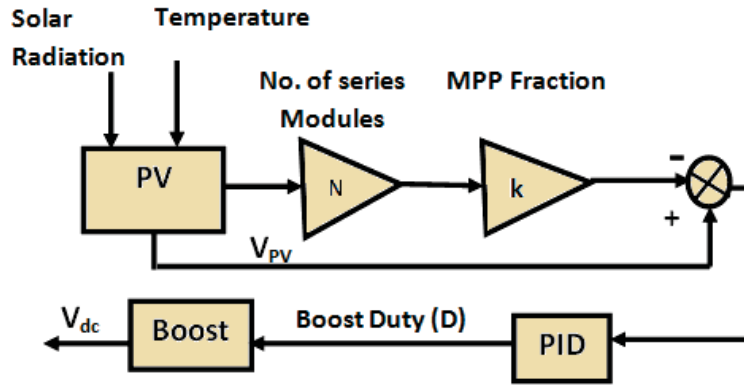
Fig. 4.14 Boost with MPP block diagrams

advantage of using the boost converter is to increase the array voltage to higher levels suitable for grid interconnection.

4.8.2 Perturbation and Observation (P&O) Method

The P&O method has been widely used for MPPT because it is straight forward. This approach requires only measurements of *Vpv* and *Ipv*, and it can track the MPPT accurately under varying irradiance and temperature. According to its name, the P&O algorithm perturbs *Vpv* and observes the impact of this change on the output power of the PV array [4.22, 4.26]. Fig. 4.15 shows the flow chart of the P&O algorithm. At each time interval *(k)*, the power of the array *Ppv(k)* as a function of *Vpv* and *Ipv* is calculated. The calculated value of *Ppv(k)* is compared to the value *Ppv(k-1)* determined at the previous interval. If the output power has found to be increased, *Vpv* is adjusted further in the same direction as in the previous interval. Otherwise if the output power has decreased, then *Vpv* should be perturbed in the opposite direction of the previous interval. According to this procedure the MPP is thus perturbed at cycle. The flow chart of algorithm has 4 cases as shown in Fig. 4.15 and can be detailed as following

- When $\Delta P < 0$ & $V(j) > V(j-1)$, this yields to $Vref = V(j+1) = V(j) - \Delta V$

- When $\Delta P < 0$ & $V(j) < V(j-1)$, this yields to $Vref = V(j+1) = V(j) + \Delta V$

- When $\Delta P > 0$ & $V(j) < V(j-1)$, this yields to $Vref = V(j+1) = V(j) - \Delta V$

- When $\Delta P > 0$ & $V(j) < V(j-1)$, this yields to $Vref = V(j+1) = V(j) + \Delta V$

When the MPP is approached, *Vpv* may oscillate around the optimal value *Vpv,mpp* depending on the magnitude of the step size. These oscillations lead to a reduction in the produced power of the relay with increasing the step size of the perturbation.

In this respect it should be noted, if this step size is large, the MPPT algorithm responds quickly to sudden changes in environmental conditions. On the other side, if the step size is small the algorithm becomes relatively slow and not be able to respond quickly to rapid changes in temperature or irradiance.

Fig. 4.16 shows the block diagram of the automatic converter control to reach the MPP. This control includes a PI controller. The error signal driving the PI controller is equal to the differences between the adjusted reference terminal voltage, *Vref* and the array voltage *Vpv*. The output of the controller is fed to PWM to generate the firing signals of the DC/DC converter.

4.8.3 Incremental Conductance Method

The Incremental Conductance method has been proposed to avoid the drawbacks of the P&O MPPT method. It is based on the fact that the derivative of the output power *Ppv* with respect to the panel voltage *Vpv* is equal to zero at the maximum power point [4.26-4.28]. The PV panel *Ppv-Vpv* characteristic in Fig. 2.2 shows further that this
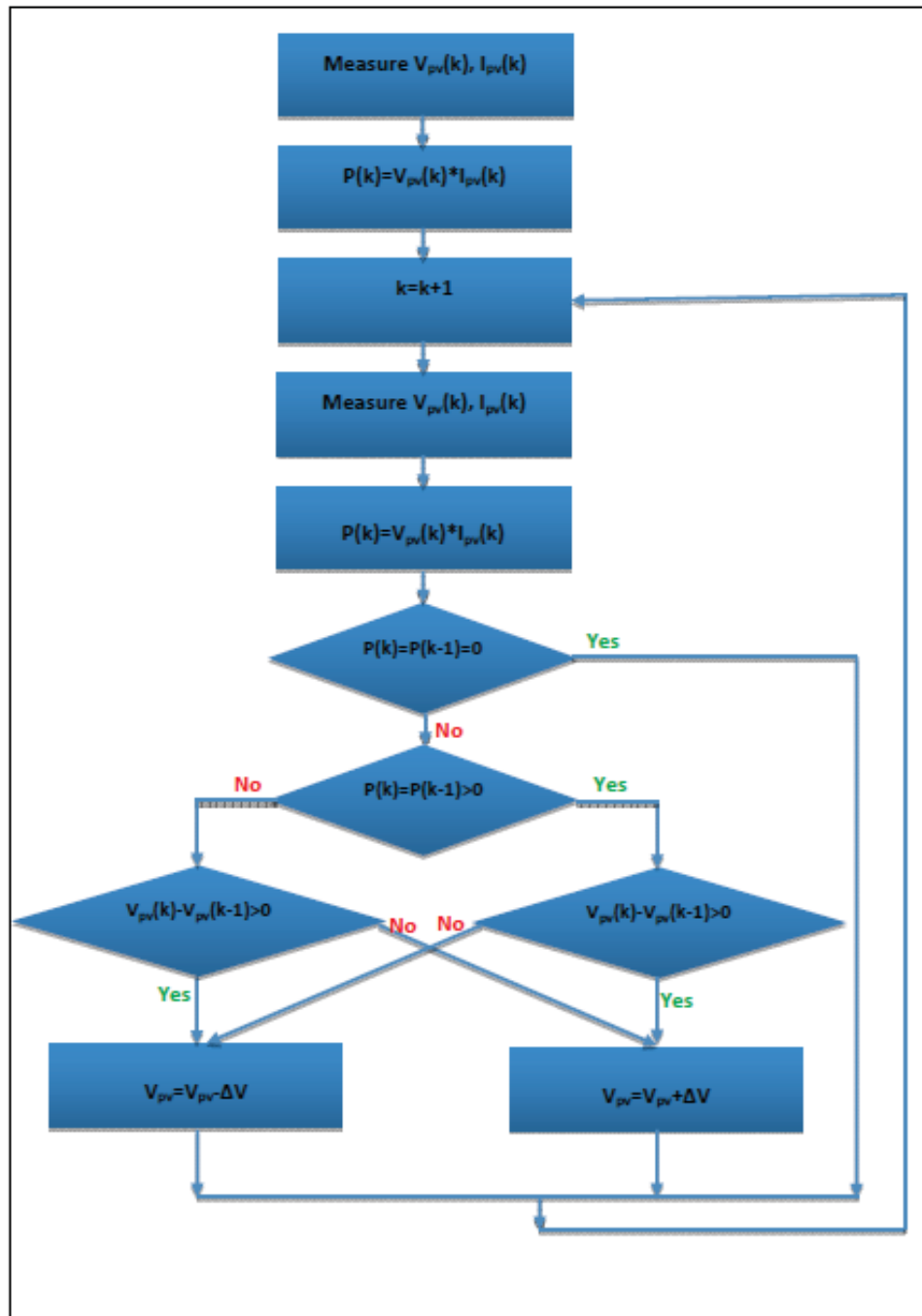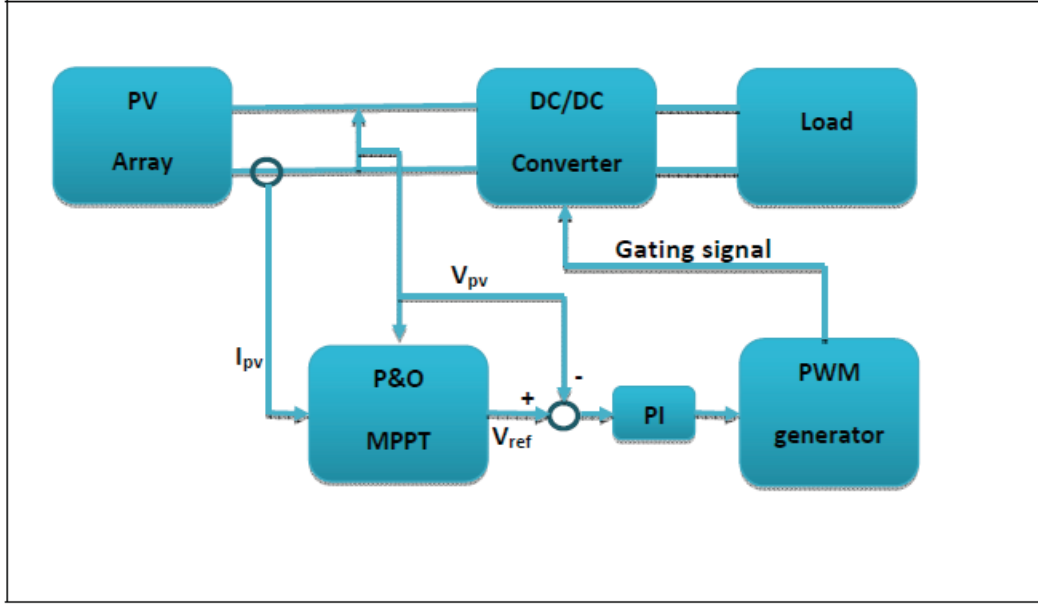
Fig. 4.15 Block diagram of P&O methods

168

Fig. 4.16 Schematic diagram of Converter control for MPPT

derivative is positive to the left of the maximum power point and negative to the right of maximum power point. This leads to the following set of equations:

$$\frac{dP_{pv}}{dV_{pv}} = \frac{d(I_{pv}V_{pv})}{dV_{pv}} = I_{pv} + V_{pv}\frac{dI_{pv}}{dV_{pv}} = 0 \qquad \text{at MPP} \tag{1.7}$$

$$\frac{dP_{pv}}{dV_{pv}} = \frac{d(I_{pv}V_{pv})}{dV_{pv}} = I_{pv} + V_{pv}\frac{dI_{pv}}{dV_{pv}} > 0 \qquad \text{to the left of MPP} \tag{1.8}$$

$$\frac{dP_{pv}}{dV_{pv}} = \frac{d(I_{pv}V_{pv})}{dV_{pv}} = I_{pv} + V_{pv}\frac{dI_{pv}}{dV_{pv}} < 0 \qquad \text{to the right of MPP} \tag{1.9}$$

These equations can be written as:

$$\frac{dI_{pv}}{dV_{pv}} = -\frac{I_{pv}}{V_{pv}} \qquad \text{at MPP} \tag{1.10}$$

$$\frac{dI_{pv}}{dV_{pv}} > -\frac{I_{pv}}{V_{pv}} \qquad \text{to the left of MPP} \tag{1.11}$$

$$\frac{dI_{pv}}{dV_{pv}} < -\frac{I_{pv}}{V_{pv}} \qquad \text{to the right of MPP} \tag{1.12}$$

169

The equation above can be used as a control algorithm to control the inverter operating point by measuring the incremental and instantaneous inverter conductance ($dI_{PV}\big/dV_{PV}$ and $I_{PV}\big/V_{PV}$, respectively). The schematic diagram of the control algorithm is shown in Fig. 4.17. The method may be more difficult to implement than the previous methods because it involves cases in which the denominators may be equal to zero.
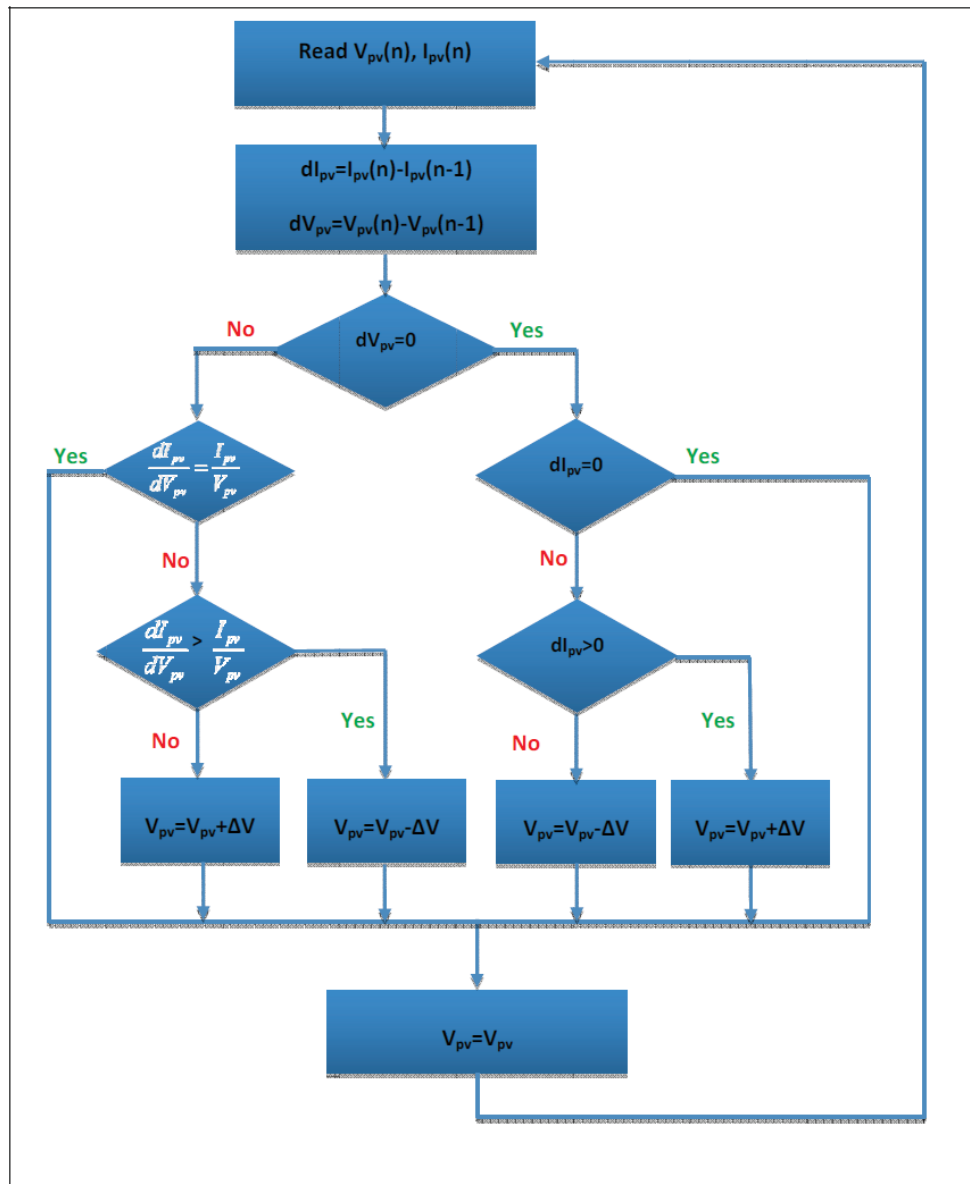
Fig. 4.17 Schematic diagram of incremental conductance MPPT algorithm

Vref is the reference voltage at which the PV array is forced to operate. For MPP, the error signal (e) determined in Fig. 4.18 is fed to PI controller to regulate the array terminal voltage to the MPP value by switching the IGBT devices according to the duty cycle of the converter. Once the MPP is reached, the operation of the PV array is maintained at this point unless a change in d*I* is noted, indicating a change in atmospheric conditions and the MPP. The algorithm decrements or increments *Vref* to track the new MPP.

By proper control of the power converter, the initial operating point is set to match a load resistance proportional to the ratio of the open-circuit voltage (V_{OC}) to the short-circuit current (I_{SC}) of the PV array. A less obvious, but effective way of performing the IC technique is to use the instantaneous conductance and the incremental conductance to generate an error signal (e) as shown in Fig. 4.18.

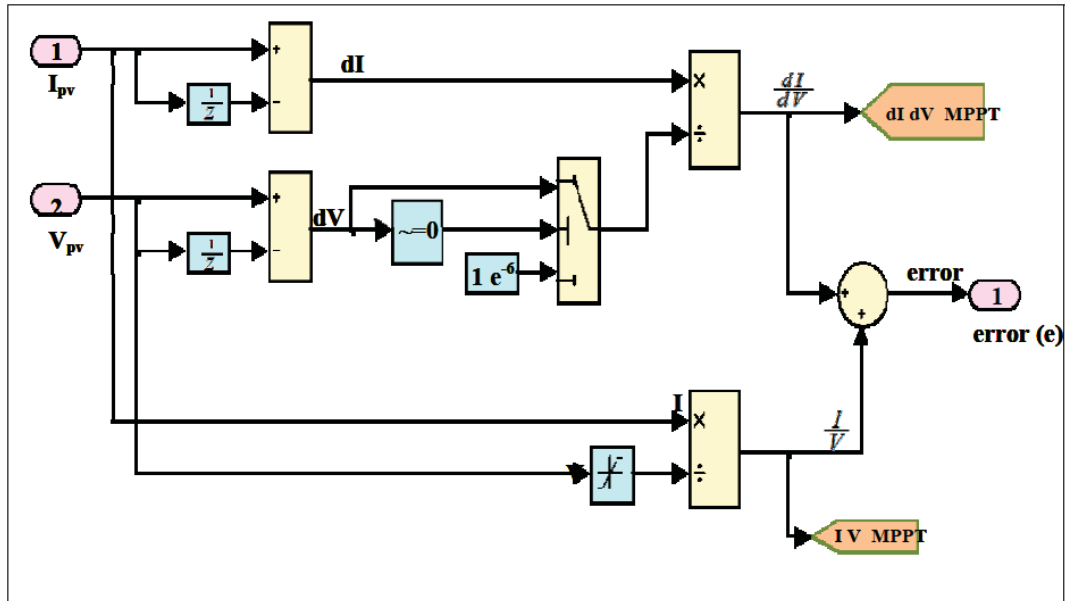$$e = \frac{I}{V} + \frac{dI}{dV} \qquad (1.13)$$

Fig. 4.18 Simulink model to determine the error signal in IC algorithm

4.8.4 Comparison of MPPT Algorithms

Simulink software is used to model the studied grid-connected PV array with a MPPT boost converter tracker as shown in Fig. 4.19. The solar array block simulates the nonlinear *V–I* characteristics of the panel at different solar radiations and temperatures. The specifications of studied solar panel are given in Table 4.2. As depicted in Fig. 4.19 the boost converter is connected from the output of the solar array to the DC/AC inverter. The produced electric power is controlled by varying the on/off duty cycle of the converter.
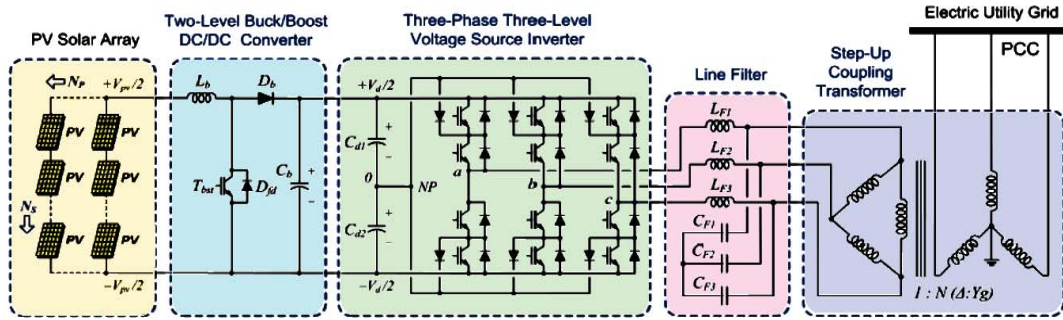

Fig. 4.19 Simulated Grid Connected Solar Array

Table 4.2 PV Panel Specifications

Description	Symbol	Value	Unit
Open Circuit Voltage	V_{OC}	20.8	V
Short Circuit Current	I_{SC}	3.6	A
O.C. Voltage/Temp. Coff.	K_V	-75×10^{-3}	V/°C
No. of Series cell/module	N_S	36	
No. of series connected module	N_{SS}	33	
No. parallel module	N_P	60	
Array power rating at NOTC	P_A	100	kW

In order to verify the MPP tracker for the photovoltaic simulation system, the described MPPT techniques are compared at different ambient conditions in Kuwait to show how they can effectively and accurately tracks the maximum power of the array. The simulation is carried using MATLAB/SIMULINK. The output of the MPPT control block is the gating signal which is used to drive the IGBT switching devices.

The boost converter is designed according to the maximal power of the array. Table 4.3 shows the parameters of the DC-DC boost converter. The test data consist of hourly radiation and temperature for time horizon of 6 years in Kuwait as described in the previous report. This data are applied to check the effectiveness of the described MPPT techniques in producing the maximum annual energy of the photovoltaic systems.

Table 4.3 Buck-Boost Converter Parameters

Parameter	Value
Inductance L	5 mH
Capacitance C_1	100 µF
Capacitance C_2	6000 µF
Frequency	5 KHz

4.9 Simulation and Numerical Results

For each MPPT technique and for hourly input data, the energy supplied by the PV system was calculated for each month averaged over the studied period of 6 years. The implemented controller for the three studied MPP algorithms is PI type with K_p=2 and K_i=0.05. The same Boost converter with its maximum MPP controller is used for comparison. The results are summarized in Table 4.4. The simulation results indicated

that the generated energy from the tracking algorithm using P&O MPPT is maximum

with annual energy of 166233.548 kWh. From the result in Table 4.4, It can be noted

that the P&O and IC algorithms over the year are superior to the CV algorithm. The

produced energy using CV technique is the lowest of the three studied MPPT methods

with annual value of 165012.804. This is attributed to the fact, that CV technique does

not follow the MPP, but instead fixes the reference voltage to the optimal voltage under

STC or to another best fixed voltage, holding it constant under any operating condition.

However, in December and January the generated energy using the CV technique is

slightly greater than both IC and P&O techniques. On the other hand, IC has slightly

smaller energy production compared to P&O techniques in February, March, April,

May August, September, October and November. On the other hand, the generated

energy in June and July using IC MPP technique is maximum compared to that of CV

and P&O techniques.

**Table 4.4 Energy Generated Using MPP Techniques in kWh**

Month	CV	P&O	IC
Jan	6402.368	6397.408	6395.114
Feb	7492.296	7521.864	7440.720
Mar	13050.194	13031.284	13019.318
Apr	14500.200	14522.400	14477.880
May	19403.458	19533.100	19489.328
Jun	20588.460	20765.760	20779.740
Jul	21131.274	21385.784	21399.920
Aug	19901.690	20234.444	20183.914
Sep	16430.160	16626.240	16577.160
Oct	12045.360	12153.302	12120.256
Nov	7418.340	7432.860	7430.340
Dec	6649.004	6629.102	6618.562
Total	**165012.804**	**166233.548**	**165932.252**

Moreover, for these techniques the choice of sampling period is very critical; if the period is too short, energy production will be very low because of the increased number of electronic switching. If the period is too long, on the other hand, the MPP cannot be closely followed when rapid irradiance variation occurs.

The purposes of the next tests are to investigate the dynamic characteristics of a PV system and to calculate the amount of power, voltage and current using the described MPPT controller. It should be noted that the generated power of has the same shape as the solar insulation input, the only difference is a small transient from the rapid insulation variation by using P&O and IC techniques. Comparing the output array voltage, it can be observed that the CV method is more stable with solar insulation variation.

In particular due to lack of space, Figs. (4.20-4.22) show the selected responses of the PV array using the IC, P&O and CV algorithms. In the first test, the MPPT controller is tested under a sunny day, and then cloudy and partially cloudy days to calculate the amount of the oscillation in PV operating points. The dynamic response of the PV array indicated that the CV technique delivers the more stable voltage, current and power waveforms with negligible oscillation amplitudes. Table 4.5 summarizes the oscillations in voltage, current and power using IC and P&O techniques. This is attributed to the IGBTs switching effect to change the array voltage to satisfy the MPP conditions of IC and P&O techniques
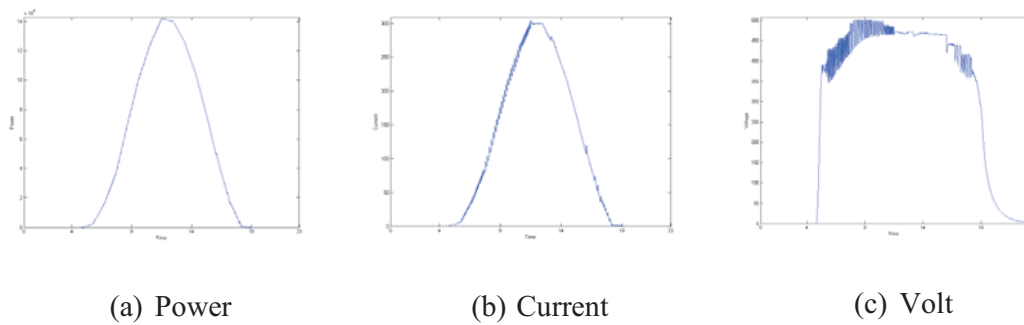
4.9.1 Dynamic response of the PV array for clear day 28th June

(a) Radiation
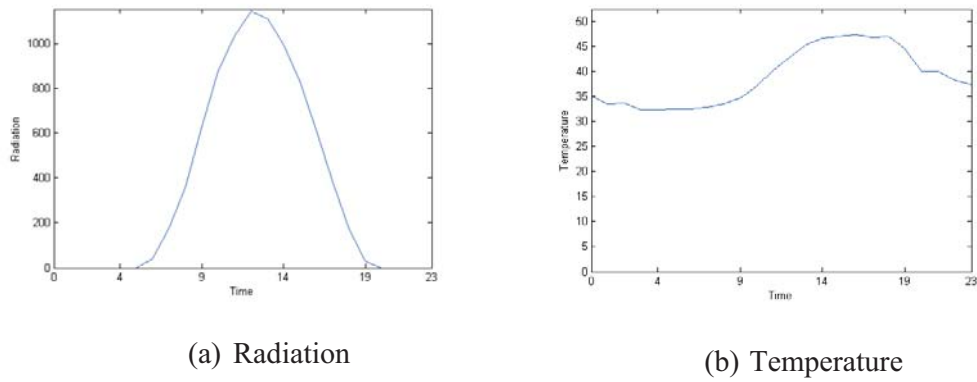
(b) Temperature

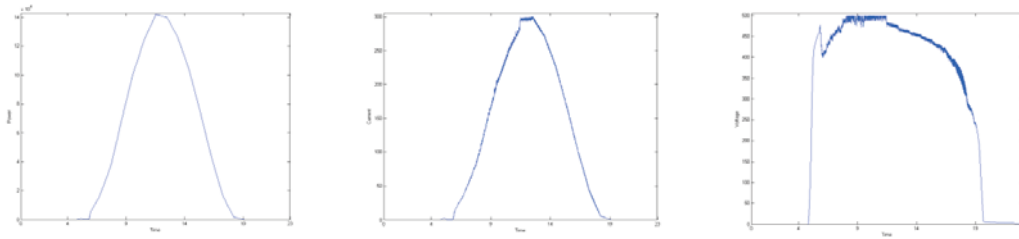**Fig. 4.20 Radiation & Tempreture (26th June)**

(a) Power
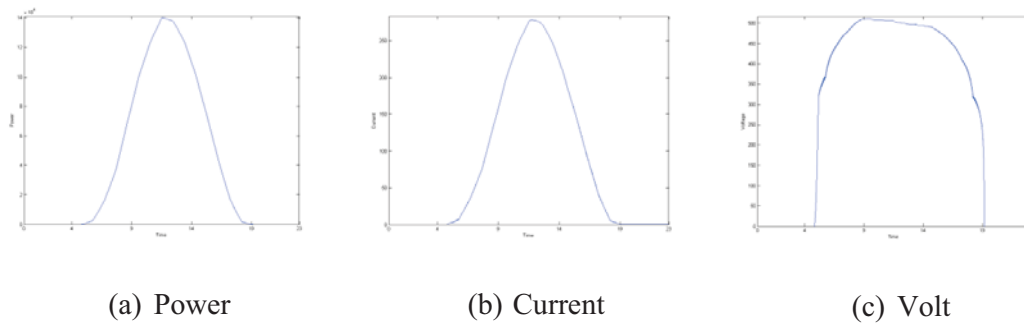
(b) Current

(c) Volt

Fig. 4.21 Dynamic Response of PV Array using CV algorithm

(a) Power

(b) Current

(c) Volt

Fig. 4.22 Dynamic Response of PV Array using IC algorithm

176

(a) Power   (b) Current   (c) Voltage

Fig. 4.23 Dynamic Response of PV Array using P&O algorithm

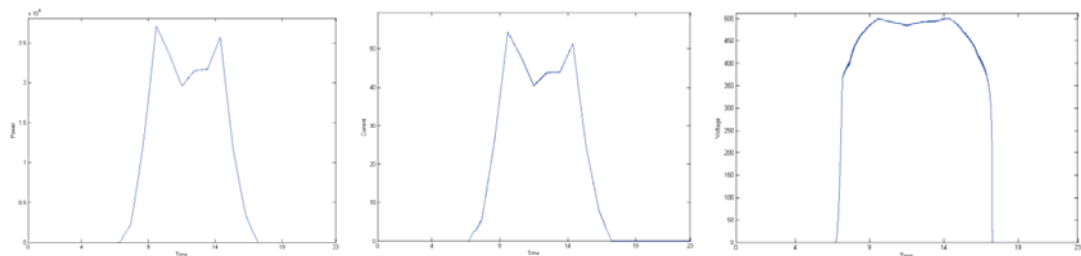## 4.9.2 Dynamic response of the PV array for partially clouded day 19th Jan
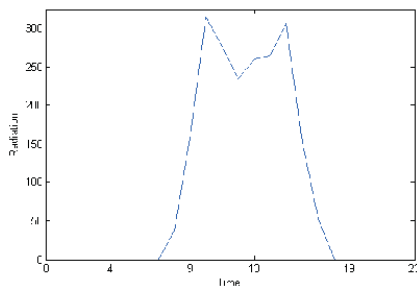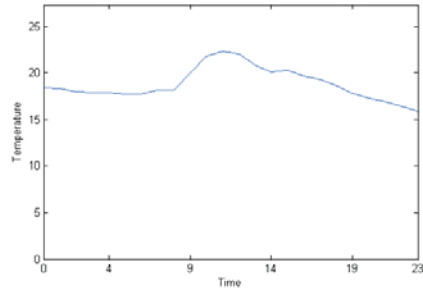
(a) Radiation   (b) Temperature

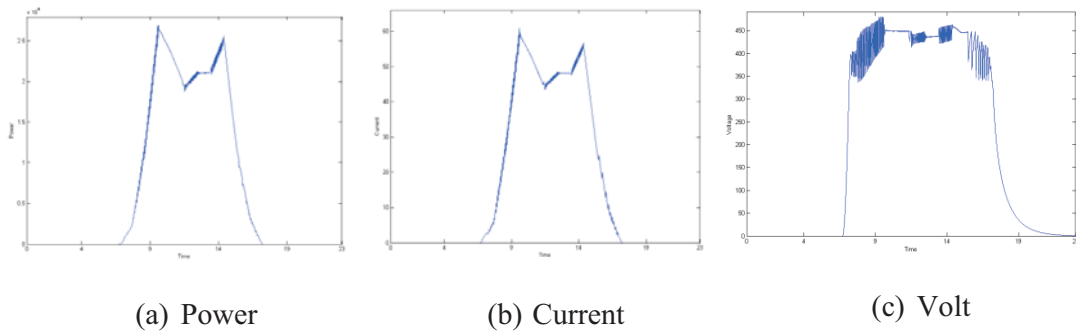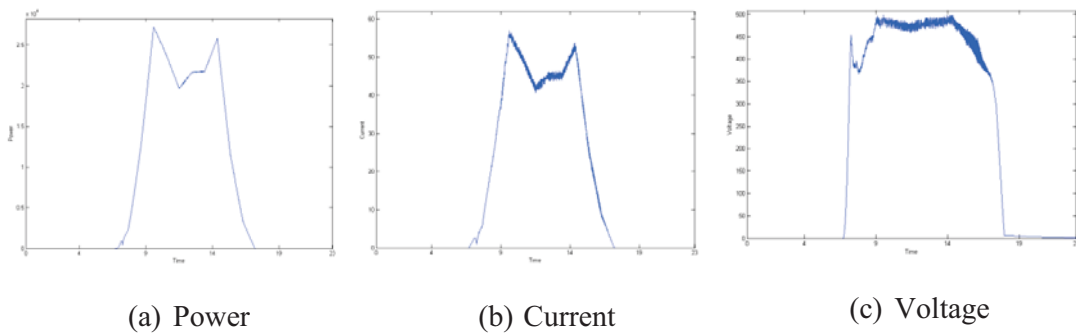**Fig. 4.24 Radiation & Tempreture (19th January)**

(a) Power   (b) Current   (c) Volt

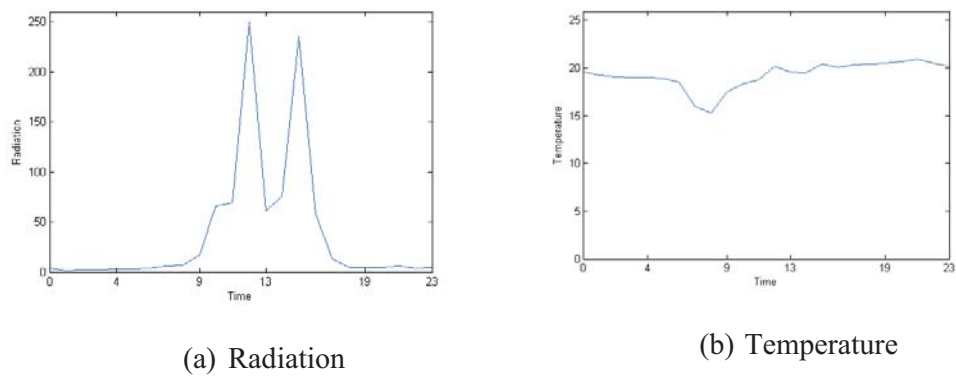**Fig. 4.25 Dynamic Response of PV Array using CV algorithm**

177

(a) Power   (b) Current   (c) Volt

Fig. 4.26 Dynamic Response of PV Array using IC algorithm
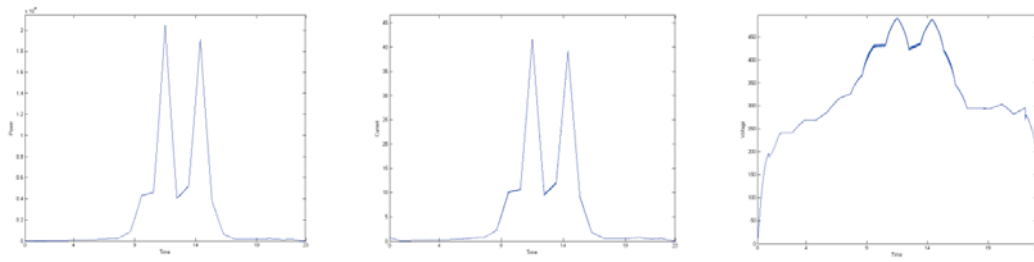

(a) Power   (b) Current   (c) Voltage

Fig. 4.27 Dynamic Response of PV Array using P&O algorithm

4.9.3 Dynamic response of PV array for clouded day 16th Nov

(a) Radiation   (b) Temperature

Fig. 4.28 Radiation & Tempreture (16th Novemper)
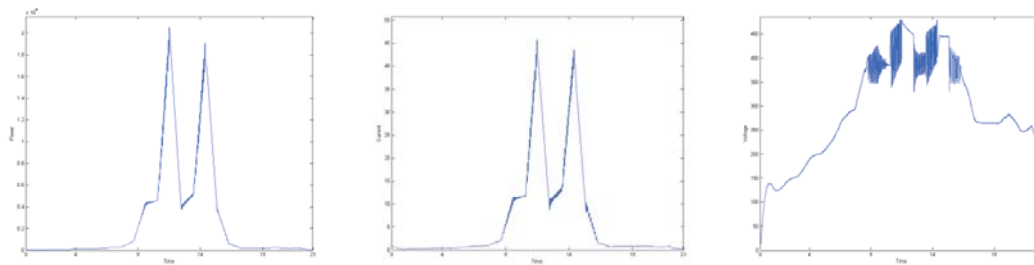
(a) Power   (b) Current   (c) Volt

Fig. 4.29 Dynamic Response of PV Array using CV algorithm
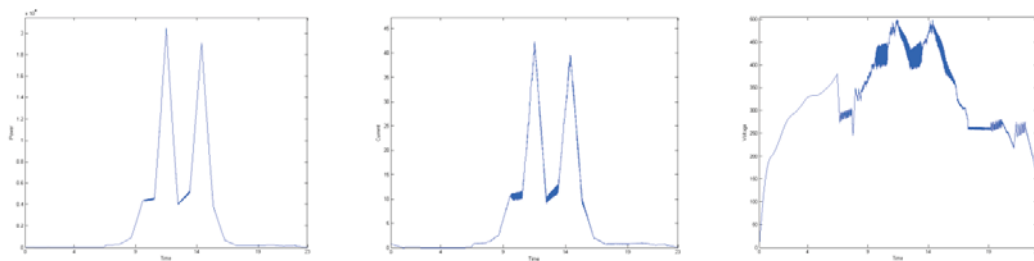

(a) Power   (b) Current   (c) Volt

Fig. 4.30 Dynamic Response of PV Array using IC algorithm

(a) Power   (b) Current   (c) Voltage

Fig. 4.31 Dynamic Response of PV Array using P&O algorithm

Table 4.5 PV Performance under different sky conditions

Sky Condition	Unit	P&O		IC	
		P-P Oscillation	Max Value	P-P Oscillation	Max Value
28th June Clear	Voltage (V)	26	510	59	510
	Current (A)	13	272	15	273
	Power (Kw)	0.04	140	0.03	141
19th Jan Partially Clouded	Voltage (V)	31	481	79	480
	Current (A)	2	59	1.5	58.5
	Power (Kw)	0.05	28.5	0.08	28
16th Nov Clouded	Voltage (V)	36	479	53	477
	Current (A)	1.7	42.4	2.5	42
	Power (Kw)	0.07	22.3	0.1	22.2

4.10 Conclusion

This chapter presents in details a comparative study between constant voltage technique and the two most popular algorithms which are Perturb & Observe algorithm and Incremental Conductance algorithm. To carry out this study the hourly solar radiation, and temperature were collected for a period of 6 years in Kuwait. The Boost converter with the associated PI controller is used for this comparison. Matlab/ simulink have been used for modeling and simulation of the PV array. The capacity of the simulated PV array is 100 kW under 1000W/m^2 and 25^{0}C conditions. A ranking was proposed of the different MPPT techniques based on the sum of the energy generated under different

weather conditions. Due to lack of space the average generated energy each month was displayed and compared.

The results indicated that the P&O and IC algorithms are in general more efficient than CV MPPT technique. In fact, the CV technique did not completely follow the MPP, but instead fixed the reference voltage to the optimal voltage under STC values, holding it constant under any operating condition. The P&O technique provides the greatest annual energy supply for the studied period of 6 years. This is confirmed by their widespread use in commercial implementations. The IC method provided only slightly less annual energy than the P&O. The generated power output of the three methods has the same shape as the solar insulation. The only difference was a small transient from the rapid insulation variation.

In addition, the dynamic response comparison of voltage, current and power output has been traced under different condition of available radiation and temperature. The MPPT controller was tested under a sunny day, and then cloudy and partially cloudy days to calculate the amount of the oscillation in PV operating points. The simulation results indicated that the CV techniques delivered more stable voltage and current signal of the PV array compared to IC and P&O techniques. Underway the fuzzy logic controller will be implemented to enhance the performance of the most suitable P&O algorithm.

References

[4.1] T. Nordmann and L. Clavadetscher, "Understanding tempreture effect on pv system performance", Proceedings of 3rd World Conference on Photovoltaic Energy Conversions, vol. 3, May 2003, pp. 2243-2246.

[4.2] Photovoltaic devices – part 3: Measurement principles for terrestrial Photovoltaic (PV) solar devices with reference spectral irradiance data, IEC 60904-3-ED. 2.0, 2008.

[4.3] BP, 230W Photovoltaic module BP 3230T. [Online]. Available: http://www.bp.com/liveassets/bp_internet/solar/bs_solar___usa/STAGING/local_assets/downloads_pdfs/pq/BP3230T_1-10.pdf

[4.4] T. Markvart (edit.), Solar Electricity (Energy Engineering Learning Package). Chichester, England: John Wiley & Sons, 1994.

[4.5] F. A. Farret and M. G. Simoes, Integration of Alternative Sources of Energy. Hoboken, NJ: Wiley-IEEE press, 2006.

[4.6] T. Esram and P. Chapman, "Comparison of Photovoltaic array maximum power point tracking techniques," IEEE Transactions on Energy Conversion, Vol. 22, no. 2, Jun. 2007, pp. 439-449.

[4.7] T. L. Nguyen and K.-S. Low, "A global maximum power point tracking scheme employing direct search algorithm for Photovoltaic systems," IEEE transactions on Industrial Electronics, vol. 57, no. 10, Oct. 2010, pp. 3456-3467.

[4.8] Y. Huang, F. Peng, J. Wang, and D. Yoo, "Survey of the power conditioning system for PV power generation," in Power Electronics Specialists Conference, 2006. PESC'06. 37th IEEE. IEEE, 2006, pp.1-6.

[4.9] M. Liukkonen, A. Hentunen, and J. Suomela, \Analysis of the ultracapacitor module in power buffering," in Proceedings of 4th European Symposium on Super Capacitors & Applications, Bordeaux, France, Oct. 2010.

[4.10] SMA, Sunny Mimi Central Installation guide. [Online]. Available:

http://download.sma.de/smaprosa/dateien/5710/SMC9-11TLRP-IEN100640.pdf

[4.11] Texas Instruments. Understanding Boost Power Stage in Switchmode Power Supplies. Texas Instruments, Mar. 1999. PDF

[4.12] Van Duijsen P.J., Bauer P., Lascu D., "Selection of Semiconductor Models in Power Electronics Simulation", Proceedings of the PCIM 2003

[4.13] R. W. Erickson and D. Maksimovic. Fundamentals of Power Electronics. Kluwer Academic Publishers, 2nd edition, 2001.

[4.14] "Boost Switching Converter Design Equations." Electronics, PCB Design and PCB Layout. Day counter, Inc, 2004. Web. 25 Feb. 2011. <http://www.daycounter.com/LabBook/BoostConverter/Boost-Converter-Equations.phtml>.

[4.15] C.Hua, C.Shen, " Comparative study of peak power tracking techniques for solar storage system" Applied Power Electronics Conference and Exposition, APEC 98. Conference Proceedings 1998,. Volume 2, pp 679-685, 15-19 Feb. 1998.

[4.16] Trishan Esram , Pa trick L. Chapman, "Comparison of photovoltaic array maximum power point tr acking techniques", IEEE Transactions on energy conversion, Vol. 22, No. 2, June 2007.

[4.17] N. Femia, G. Petrone, G. Spagnuolo, and M. Vitelli, "Optimization of perturb and observe maximum power point trackingmethod," IEEE Trans. Power Electron., vol. 20, no. 4, pp. 963–973, Jul. 2005.

[4.18] Weidong Xiao, William G. Dunford, Patrick R. Palmer, Antoine Capel, "Regulation of photovoltaic voltage", IEEE Transactions on Industrial Electronics, Vol. 54, No.3, June 2007

[4.19] Trishan Esram , Pa trick L. Chapman, "Comparison of photovoltaic array maximum power point tr acking techniques", IEEE Transactions on energy conversion, Vol. 22, No. 2, June 2007

[4.20] Calavia, M., Perié, J.M., Sanz, J.F. and Sallán, J., 2010. Comparison of MPPT strategies for solar modules. International Conference on Renewable Energies and Power Quality, Granada, Spain, March 23-25, 2010.

[4.21] Y. M. Tung, A. P. Hu, N. K. Nair, "Evaluation of Micro Controller Based Maximum Power Point Tracking Methods Using dSPACE Platform," Australian University, Power Engineering Conference 2006.

[4.22] F. Liu, Y. Kang, Y.Zhang and S. Duan, "Comparison of P&O and Hill Climbing MPPT Methods for Grid-Connected PV Converter," Industrial Electronics and Applications, 2008. ICIEA 2008. 3rd IEEE Conference, pp. 804 - 807.

[4.23] S. Jain, and V. Agarwal, "Comparison of the performance of maximum power point tracking schemes applied to single-stage grid-connected photovoltaic systems," IET Electr. Power Appl., 2007, pp. 753 - 762.

[4.24] C. Jaen, C. Moyano, X. Santacruz, J. Pou, and A. Arias, "Overview of maximum power point tracking control techniques used in photovoltaic systems," Electronics, Circuits and Systems, 2008. ICECS 2008. 15th IEEE International Conference, pp. 1099 - 1102.

[4.25] D. P. Hohmand , M. E. Ropp, "Comparative Study of Maximum Power Point Tracking Algorithms," Progress in Photovoltaic Research and Applications, vol. 11, no. 1, pp. 47–62, 2003

[4.26] Y.-C. Kuo, T.-J. Liang, and J.-F. Chen, "Novel maximum-power-point tracking controller or photovoltaic energy conversion system," *IEEE Trans. Ind. Electron.*, vol. 48, pp. 594-601, June 2001.

[4.27] G. J. Yu, Y. S. Jung, J. Y. Choi, I. Choy, J. H. Song, and G. S. Kim, "A novel two-mode MPPT control algorithm based on comparative study of existing algorithms," in *Conf. Record of the Twenty-Ninth IEEE Photovoltaic Specialists Conf.*, 2002, pp. 1531-1534.

[4.28] Hairul Nissah Zainudin, Saad Mekhilef, Comparison Study of Maximum Power Point Tracker Techniques for PV Systems, Proceedings of the 14th International Middle East Power Systems Conference (MEPCON'10), Cairo University, Egypt, December 19-21, 2010, Paper ID 278..